EUROPEAN ORGANIZATION FOR NUCLEAR RESEARCH

CERN-EP/87-60
23 March 1987

TODAY AND TOMORROW FOR SCINTILLATING FIBRE (SCIFI) DETECTORS

Jasper Kirkby

CERN, Geneva, Switzerland

ABSTRACT

We review the current status of SCIFI detectors in experimental particle physics and their prospects in tomorrow's supercollider detectors. Our main focus concerns tracking devices although we also discuss the important aspects of SCIFI calorimetry. We could say, in summary, that SCIFI detectors will have a bright future.

Invited talk at the
INFN Eloisation Project - Workshop on Vertex Detectors:
State of the Art and Perspectives,
Erice, Sicily, 21-26 September 1986

0181N/JK/sm

CONTENTS

./.

CONTENTS (cont.)

TODAY AND TOMORROW FOR SCINTILLATING FIBRE (SCIFI) DETECTORS

Jasper Kirkby

CERN
Geneva, Switzerland

ABSTRACT

We review the current status of SCIFI detectors in experimental particle physics and their prospects in tomorrow's supercollider detectors. Our main focus concerns tracking devices although we also discuss the important aspects of SCIFI calorimetry. We could say, in summary, that SCIFI detectors will have a bright future.

SECTION I: TODAY

1. PRINCIPLE OF OPERATION

In the late 1950's an intensive effort was devoted to the observation of the tracks of charged particles in, initially, solid scintillators such as NaI (Tl) and then in targets made from coherent (parallel) bundles of plastic or glass scintillating fibres[1]. The fibre approach results in an excellent effective depth-of-field since a certain fraction of the scintillation light is 'trapped' inside the fibres by total internal reflection and consequently the optical image is preserved by the coherent geometry and transported to an output face (Fig. 1). The early work achieved considerable success but came to a halt in the early 1960's when bubble and spark chambers emerged as the clear leaders for particle tracking.

However, since that time there have been considerable advances in the technologies associated with SCIFI detectors, namely scintillators, fibre optics, image intensifiers, multi-anode phototubes, CCD cameras and data acquisition systems. As a result, and in view of their attractive properties, a renewed development of SCIFI detectors is taking place.

The modern wave of SCIFI development started with the work on plastic fibres by Borenstein et al.[2] and then by Saclay[3]. The contemporary work on glass SCIFI was initiated by Potter[4] and Ruchti et al.[5]. Additional groups are now involved in the development of tracking detectors based on scintillating fibres of plastic[6-8], glass[9,10] and liquid in glass capillaries[11] and in the

development of calorimeters based on plastic scintillating fibres[12-14], plastic wave-shifting fibres[15,16] and liquid scintillator in teflon tubes[17].

The operation of an individual scintillating fibre is illustrated by the example shown in Fig. 2. All types of scintillating optical fibre possess a scintillating core material surrounded by a non-scintillating optical cladding of a lower refractive index (producing a 'step index' fibre). The cladding provides a highly efficient reflective surface for transporting along the fibre the light which is contained inside a narrow cone of half angle, $90°-\Phi_{critical}$ (see Fig.2). In order to perform efficiently, the interface between the core and cladding must be optically smooth and, since the electromagnetic wave extends (with an exponentially-decreasing amplitude) into the cladding, the cladding material must be transparent and of depth several wavelengths ($\gtrsim 5$ in these applications). The cladding serves, in addition, to isolate the reflective surface from mechanical or chemical damage; fibres can, in principle, be more easily handled than sheets of scintillator where the reflective surface is exposed.

The fraction of the total scintillation light which is trapped in each direction is approximately 0.5 [1-n(cladding)/n (core)], where n is the refractive index. (This expression is approximate because it does not account for non-meridianal rays; the effect is to underestimate the trapping fraction by a factor of 15-30%, depending on fibre geometry.) The trapping efficiencies of glass, plastic and liquid SCIFI are seen (Table 1) to be small, between 2.5-4% in each direction. This can be compared with 10-15% for the optical collection efficiency of typical sheets of plastic scintillator. In order to absorb the large (92-95%) fraction of untrapped scintillation light, each fibre may include an optional outer layer of a thin opaque material (extra mural absorber, EMA) as indicated in Fig. 2.

Table 1

Approximate SCIFI optical trapping efficiencies

Scintillator medium	Core material	n (core)	Cladding material	n (clad.)	Trapping efficiency ε (%) *)
Glass	GS1	1.59	N51A	1.51	2.5
Plastic	Polystyrene +PBD+POPOP	1.59	Polyvinyl acetate	1.46	4.1
Liquid	Methyl-naphthalene +bis-MSB	1.62	N51A	1.51	3.4

*) The trapping efficiency for scintillation light, in each direction, $\varepsilon \sim 0.5$ [1-n(cladding)/n(core)].

2. OVERVIEW

2.1 SCIFI Characteristics

The key merits of SCIFI detectors are as follows:

1. Compactness/high density of hits per unit path length, e.g. minimum ionizing particles generate 5 photoelectrons (or equivalently 'hits') per mm in plastic SCIFI at a length of 1 m.

2. Fine spatial resolution, e.g. $\sigma \sim 20$ μm for glass SCIFI.

3. Fine two-track resolution, e.g. 50 μm for glass SCIFI, and absence of signal saturation up to extremely high particle densities.

4. Very high granularity, up to 10^5 cells cm^{-2}.

5. Radiation hardness. Both glass and plastic SCIFI can withstand $\lesssim 10^6$ rads with tolerable losses in light output.

6. Flexible/can follow curved surfaces.

7. Intrinsically fast response of the detector itself, e.g. in the case of plastic SCIFI, the pulse time can be determined to less than 1 ns and the pulse integration time is $\lesssim 20$ ns.

8. Insensitivity to magnetic fields.

9. In addition, for calorimeters:

   a) High density, e.g. with a packing fraction of 50%, a Pb/SCIFI calorimeter has a radiation length of 1.1 cm.

   b) Good hermeticity and uniformity of response with respect to transverse longitudinal and angular impact position. 'Cracks' due to wav ars or mechanical boundaries are essentially absent.

   c) Good energy resolution for electromagnetic showers, due to the fine sampling. The measured values are $\sigma_E/E \lesssim 10\%/\sqrt{E(GeV)}$, extending down to very low energies (~ 20 MeV) in the case of phototube readout.

   d) An imaging capability which can provide, for example, a precise location of the conversion point or shower core.

   e) The capability to construct a 'compensating' hadron calorimeter (relative electron/hadron response = 1) from non-exotic absorber materials such as Pb.

2.2 Applications

These characteristics point to the following applications of SCIFI detectors:

1. Live targets either for detecting short-lived heavy-flavoured particles[18] or for rare decay experiments involving stopped particles[19].

2. Tracking in the environment of very high multiplicity and particle density such as high-energy ^{16}O interactions[20].

3. Precise, compact tracking in collider detectors[21].

4. Charge-flow tracking, i.e. the measurement of charged particle densities in jets, rather than to measurement of individual particles.

5. z-vertex measurement in supercollider detectors.

6. Electromagnetic calorimetry[22] with an imaging capability.

7. Hadron calorimetry which is hermetic and compensated.

In the remainder of Section I we first examine the choice of scintillators and their performance in fibres. We will point out the limitations of present scintillating fibres and indicate possible solutions. This is followed by a description of the readout techniques and a review of the experimental status of SCIFI tracking detectors. In Section II we consider the influence of SCIFI on the design and performance of tomorrow's supercollider detector. This section also discusses the readout of SCIFI detectors at ultra-high rates.

3. CHOICE OF SCINTILLATOR

3.1 Overview

We compare in Table 2 the main characteristics of glass and plastic SCIFI. Plastic scintillators are seen to be generally well-suited to SCIFI applications: good light yield, long attenuation length, fast, low mass, reasonably radiation-hard and relatively easy (i.e. low temperature) fibre production. The major limitation concerns the lack of efficient narrow-diameter fibres; present scintillator/waveshifter combinations are unsuitable below fibre diameters of ~ 500 μm. Glass scintillators, however, do not suffer from this problem and can be drawn into extremely fine fibres without loss of efficiency. With the exception of this property and also of radiation hardness, glass SCIFI is generally inferior in comparison with plastic SCIFI. The most serious limitation is the very short attenuation length.

In view of these characteristics the development of glass SCIFI has centred on precise small-volume active targets whereas plastic SCIFI has largely been used in compact tracking ofmoderate resolution or in calorimetry. We will now discuss the characteristics of these scintillators in more detail.

Table 2

Comparison of the key properties of glass and plastic SCIFI

Property	Glass ($GS1\text{-}Ce^{3+}$)	Plastic (Polystyrene +PBD+POPOP)	
1. Photon yield of bulk material [NaI(Tℓ) = 40]	1.5 ± 0.5	8-10	photons keV^{-1}
2. Detected photoelectron yield of fibres (@ specified fibre length)	2(@ 1 cm)	5(@ 100 cm)	pe mm^{-1}
3. Attenuation length, λ	2-20	80-200	cm
4. Scintillation decay time constant, τ	55	3	ns
5. Radiation length, X_o	9.8	41.3	cm
6. Radiation hardness*	10^6	$\leq 10^6$	rads
7. Minimum diameter of efficient fibres	~ 10	~ 500	μm
8. Fibre manufacture	Difficult	Easy	

* We define radiation hardness as the exposure which causes an induced attenuation of ~ 8.7 dB m^{-1} (equivalent to λ = 50 cm) in the region of the scintillation spectrum.

3.2 Plastic scintillator

3.2.1 Scintillation mechanism

In order to understand the performance of plastic SCIFI we must first consider the mechanism of light production by organic scintillators and wave-shifters.

Light emission in organic materials[23] is an inherent molecular property, occurring not only in the crystalline state but also in vapour and dilute solution in a liquid or plastic medium. Organic phosphors are primarily pure or substituted aromatic hydrocarbons since the benzene ring constitutes a stable system with a variety of (π electron) vibrational levels. This structure is readily excited into a high vibrational state by photons or ionizing particles and then promptly (few ns) de-excites with the emission of radiation. Before radiative decay there is a rapid (10^{-12} s) vibrational relaxation in which excess energy is lost in collisions with neighbouring molecules. This causes a (Stokes) shift of the bands of fluorescent light to somewhat longer wavelengths than those corresponding to the original transition from the ground state vibrational levels. However, in most scintillators there is a significant overlap of these two spectra -- the absorption (or excitation) and emission spectra -- which results in a ('self') absorption length of the primary fluorescent light of only a few mm. Therefore, in order to allow light to be transmitted through appreciable thicknesses of the material, a further fluorescent component is added which preferentially absorbs the scintillation light and re-emits at longer wavelengths. The second component (the 'waveshifter') is typically present in small concentrations (0.01-1% by weight) since it has a large absorption cross-section. Further waveshifters may be added until the final light has a sufficiently long wavelength for good transmission (λ = 1-2 m) through the bulk material. The properties[24] of some scintillator and waveshifter materials in common use are summarized in Table 3.

3.2.2 Overview of properties

We compare the three common classes of plastic scintillators in Table 4. They are characterized by their polymer base material as follows:

1. PVT (polyvinyl toluene or polymethyl styrene). This is the material typically used by industrial manufacturers such as Nuclear Enterprises[25] (NE designation) or Bicron[26] (BC designation).

2. PMMA (polymethyl methacrylate or acrylic). This requires a scintillating material, such as naphthalene, to be added to the non-scintillating polymer base. It was developed[27-28] as an inexpensive and mechanically robust alternative to the PVT scintillators, albeit with somewhat reduced light output. This category is found to be the most susceptible to radiation damage.

3. Polystyrene. This was developed[28-29] as an inexpensive scintillator which could be simply fabricated in large quantities by extrusion, thus avoiding the normal process of molding between two plates of glass.

3.2.3 Light yield and attenuation length

Experimentally we observe, in NE102A (PVT scintillator), 60 photoelectrons (pe) mm^{-1} for minimum ionizing particles, with an

optical path length of 5 mm NE102A, using a RCA 8850 quantacon phototube (bialkali photocathode). The calculated light collection efficiency is 21%. In a typical large counter the observed yield reduces to 10–15 pe mm^{-1}.

Table 3

Organic scintillators and wavelength shifters

Material	Emission λ_{max} (nm)	Decay time, τ (ns)	Quantum efficiency	Photon yield (γ keV^{-1})
1. Scintillators				
Naphthalene	322	96	0.23	4.8
Anthracene	400	4.9	0.36	17
p-Terphenyl	340	0.95	0.93	10
Polyvinyl toluene	312	14	0.07	
Polystyrene	332	23	0.03	
2. Waveshifters				
PBD [1.]	360	1.1	0.92	
POPOP [2.]	410	1.4	0.93	
bis-MSB [3.]	420	1.3	0.94	
BBQ [4.]	480	18	-	
K27 [5.]	500	< 5	0.86	
3HF [6.]	510	< 1	0.36	

1. PBD: 2-phenyl-5(4-biphenylyl)-1,3,4-oxadiazole.
2. POPOP: p-bis [2-(5-phenyloxazolyl)]benzene.
3. bis-MSB: p-bis (o-methylstyryl)benzene.
4. BBQ: benzimidazo-benzisochinolin-7-on.
5. K27: xanthene acid derivative (supplied by Hoechst AG, Frankfurt, FRG).
6. 3HF: 3-hydroxyflavone.

Table 4

Properties of plastic scintillators

	PVT	Acrylic	Polystyrene
Commercial names	NE - BC -	PLEXIPOP ALTUSTIPE	KSTI
Typical composition (by weight):			
Polymer base	Polyvinyl toluene	Polymethyl methacrylate (PMMA)	Polystyrene
Additional scintillator	-	10-15% naphthalene	-
Scintillator/waveshifter 1.	2% p-terphenyl (NE102A)	1% butyl PBD	1% butyl PBD
Waveshifter 2.	0.1% POPOP (NE102A)	0.01% POPOP	0.01% POPOP
Density	1.03	1.18	1.06 g cm^{-3}
Mean refractive index, n (emission spectrum)	1.60	1.49	1.59
Softening point	75	180	98°C
Radiation length, X_o	42.4	34.4	41.3 cm
Hadronic interaction length, λ	79.5	70.8	77.4 cm
dE/dx (minimum ionizing particles)	2.0	2.3	2.0 MeV cm^{-1}
Photon yield (minimum ionizing particles)	10	3-9	8-10 photons keV^{-1}
Decay time constant, τ	3	3-7	3 ns
Wavelength of peak emission, λ_{max}	430	430	430 nm
Typical attenuation length, λ_{atten}	2	1-1.5	1-2 m
Radiation hardness (see Section 3.2.4)	$\lesssim 10^6$	$\lesssim 10^5$	$\lesssim 10^6$ rads
Mechanical handling properties	Poor	Good	Fair

Plastic SCIFI, such as produced by Saclay[3], involves a polystyrene - PBD (1%) -- POPOP (0.01%) core of diameter 0.5-1.5 mm surrounded by a polyvinyl acetate cladding of thickness 7-22 μm. This results in a trapping efficiency in each direction of approximately 4% of the scintillation light (Table 1), as compared with ~ 10% in standard (slab) scintillation counters. The observed light yield in plastic SCIFI is therefore expected to be ~ 40% of the yield of a standard counter of equal thickness. This is confirmed, as indicated in Fig. 3, where a yield of 5 pe mm^{-1} is measured[3] at 1 m distance.

Figure 3 also indicates (1-2 m) attenuation lengths for plastic SCIFI which are typical of the bulk material. This confirms the absence of substantial reflective losses at the core-cladding interface. This observation is reinforced by a measurement[3] of the attenuation in a clear (undoped) polystyrene fibre, shown in Fig. 4. Here we see excellent attenuation lengths, $\lambda > 20$ m, in the green-red spectral region. [Reference 15 found $\lambda = 11$ m for a polystyrene fibre (diameter 1.5 mm and length > 4 m) doped with the waveshifter K27 ($\lambda_{max} \sim 500$ nm).]

3.2.4 Radiation hardness

The radiation hardness of detectors was barely relevant to experimental particle physics a few years ago but, starting with the ISR and then the pp colliders, it has now become a crucial issue. Furthermore, as we shall discuss in Section II, it will become increasingly important at the supercolliders.

The experimental data[27-34] are incomplete and in some cases contradictory. This is probably due to the fact that there are many parameters which influence the amount of radiation damage, amongst which are:

1. Total dose.

2. Dose rate.

3. Type of radiation: photons, electrons, hadrons, neutrons or heavily ionizing particles.

4. Surrounding chemical environment, especially the presence of oxygen.

5. Composition of the material, in particular the presence or not of a UV-generating component. In the case of fibres, the composition of both the core and the cladding is relevant.

6. Presence in the material of small concentrations of impurities.

7. Time between irradiation and measurement (recovery), and the surrounding chemical environment during this interval.

8. Heat cycling (annealing).

We can find the following qualitative consensus among the experimental measurements:

1. All data agree that acrylic scintillators are more readily damaged by radiation than polystyrene or PVT scintillators. Equivalent damage (in the region of the scintillation spectra) occurs in the latter scintillators at about an order-of-magnitude higher doses. This is seen (Fig. 5) in transmission measurements[30] made on undoped acrylic and polystyrene fibres. The vertical axis is expressed as the attenuation,

$$A(dB\ m^{-1}) = -10\ \log_{10}\ (I_{out}/I_{in})/L\ ,$$

where I_{in} and I_{out} are the input and output light intensities (at a certain wavelength) and L(m) is the fibre length. This quantity is related to the more familiar attenuation length λ (m) by the expression λ (m) = 4.343/A (dB m^{-1}). Figure 5 demonstrates the preferential deterioration in transmission at shorter wavelengths ('yellowing' of the material). Furthermore, polystyrene exhibits a threshold in $\log_{10}$ (radiation dose) below which the induced attenuation is tolerable. This threshold, which is seen in other measurements[35], occurs between 10^5 to 10^6 rads.

2. The amount of damage does not seem to depend on the type of ionizing particle which deposits a given total energy.

3. After periods of a few days in air following exposure, substantial recoveries in transmission are observed.

The data are in less clear agreement over the following issues:

1. The influence of an oxygen atmosphere. Reference 32 finds a strong deterioration of acrylic scintillators after only 10^4 rads, providing the dose rates are small (10 rads hr^{-1}) and air is present. The damage is reduced by a factor of 10 in a N_2 atmosphere. This leads to the explanation that UV light, produced by the butyl PBD, creates free oxygen radicals from the atmospheric O_2 molecules which slowly diffuse into the plastic. Oxygen radicals are highly reactive and result in chemical damage to the material. Reference 34 similarly finds a large oxygen effect in clear (undoped) acrylic fibres, but of opposite sign. This reference also finds that the presence of oxygen leads to an accelerated (~ 4 days) and almost complete recovery of damaged acrylic fibres. A further experiment[30], involving undoped fibres of both acrylic and polystyrene, finds no effect due to dose rate in an air environment (and therefore, equivalently, no effect due to oxygen). These discrepancies may be related to the presence or otherwise of scintillators and waveshifters in the material under test.

2. The relative contribution to the observed loss of light from a deterioration of the scintillation efficiency and from a decrease in the attenuation length.

In summary, it seems that polystyrene scintillators and their fibres will operate with tolerable losses up to several 10^5 rads, and perhaps up to 10^6 rads. This is just at the level where they become viable for supercollider detectors. What is now clearly needed is a new, comprehensive and systematic study to be made of radiation damage to plastic scintillators and plastic scintillating fibres.

3.2.5 Limitations and cures

The main limitation of current plastic SCIFI is the absence of efficient narrow-diameter fibres. This is illustrated in Fig. 6 where we see (Fig. 6a) the primary scintillation light propagating a short distance before absorption and re-emission by the waveshifter. The attenuation of the primary scintillation light is given by the expression,

$$I = I_o\ 10^{-d\varepsilon c} = I_o\ e^{-d\varepsilon c(\ell n\ 10)}\ ,$$

where I is the light intensity, d(cm) is the distance of light propagation, $\varepsilon(M^{-1}\ cm^{-1})$ is the molar absorptivity (or molar extinction coefficient) and c (M) is the concentration of the waveshifter in moles $litre^{-1}$ (M). Typical values (for POPOP) are $\varepsilon = 4 \times 10^4\ M^{-1}\ cm^{-1}$ and c = 0.1 (g $litre^{-1}$)/364 (molecular weight) = $2.7\ 10^{-4}$ M. This indicates an attenuation by a factor 1/e in a distance $d = [4 \times 10^4 \times 2.7 \times 10^{-4} \times 2.3]^{-1}$ cm, i.e. 400 μm. Therefore, providing the fibre diameter is more than ~ 500 μm most of the primary scintillation light will be shifted before reaching the core-cladding interface. This shifted light will then be collected with the nominal efficiency ε (~ 4%).

As the diameter of the fibres is reduced, we see (Fig. 6b) that cross-talk will occur, i.e. light is trapped in fibres which are not intercepted by the particle. Furthermore, if one tries to correct this with EMA (Fig. 6c) the efficiency (light output) of the fibres reduces to an unacceptably low value ε^2 (~ 0.16%), since both the primary and the shifted light must be trapped.

A simple solution to this problem would be to increase the waveshifter concentrations. The drawback is this leads to a decreased bulk attenuation length, since most waveshifters in common use suffer some self absorption. It is likely, however, that some optimization can be done of the concentrations of the components in present plastic scintillators to suit specific experiments and fibre lengths.

An alternative solution is to provide each fibre with an external aluminized coating (Fig. 7). This serves to contain the primary scintillation light with a few reflections, before the waveshifting takes place. The waveshifted light is then transported in the standard fashion by reflections at the core-cladding interface. The obvious drawback here is that single fibres as opposed to multifibres (Section 4) must be handled. [Aluminization is in fact utilized for the 1 mm diameter plastic SCIFI of the UA2 track detector (Section 6.1), to provide an EMA.]

The most attractive solution is to find alternative waveshifters with better absorption and transmission properties. The waveshifter POPOP is seen (Fig. 8) to have a small Stokes shift and a region of overlap between the absorption and emission spectra. It is this overlap which leads to self absorption of the emission spectrum, especially at the shorter wavelengths. A promising new candidate to replace POPOP is 3HF[36] (3-hydroxyflavone) which displays (Fig. 9) a strikingly clean Stokes shift and a strong molar absorptivity. Furthermore it is found[37] to have an acceptable quantum efficiency (0.36, compared with 0.93 for POPOP) and a very fast decay time (< 1 ns). Of particular note is the green emission spectrumwhich should result in substantial improvements in both the attenuation length (λ ~ 20 m from Fig. 4) and, more importantly, in the radiation hardness (see Fig. 5). Studies[37,38] are presently underway to investigate plastic scintillators containing 3HF waveshifter.

Finally we mention that a suitable plastic EMA is not yet available for plastic SCIFI. As we shall see, EMA is essential in tracking devices. This situation reflects the relatively recent development of plastic SCIFI rather than any fundamental obstacle.

3.3 Glass scintillator

3.3.1 Scintillation mechanism

The luminescence of inorganic phosphors differs fundamentally from that of organic phosphors. Here the process is a lattice effect, intimately connected with the crystalline nature of the host material. An inorganic scintillator involves a crystalline or near-crystalline host insulator which is doped with a small concentration of impurity atoms, known as 'activators'. Examples are NaI activated with Tℓ or a glass matrix activated with Ce^{3+} ions. (In certain cases activator centres may also be caused simply by lattice imperfections in a pure crystalline material.) Ionizing radiation causes electrons in the host matrix to be transferred from the valence band to the conduction band. The resulting electron-hole pair (known as an 'exciton') then rapidly moves through the lattice under the influence of the electromagnetic field between the excited ion and a neighbour in the ground state. This mobility results from the crystalline nature of the host. In a pure crystal the lifetime of the exciton, which terminates when the electron and hole recombine, is estimated to be ~ 10 ns, during which time it has travelled a mean square displacement of ~ 1 μm from its origin. However, well before this time it may encounter an activator centre, which is chosen to have energy levels inside the forbidden gap of the crystalline host. This effectively locks the exciton on the activator centre, which can then decay in its characteristic time with the emission of a photon.

There are two other ways in which the activator centre may be excited. One is simply direct absorption of energy from the ionizing particle or direct absorption of photons of the appropriate frequency (for which the host may be transparent if the photons are not energetic enough to cause transitions from the valence to conduction bands). The other can involve the motion of free electrons and holes, evidently in association with conductivity.

After excitation of the activator centre the neighbouring lattice undergoes a rapid relaxation. This occurs in a time of the order of 10^{-13}-10^{-12} s, characteristic of lattice vibrations and the emission of phonons. The result is a Stokes shift of the emitted light to longer wavelengths than those of the excitation bands and, as with organic scintillators, the phosphor becomes largely transparent to its own scintillation light.

In addition to activator centres there may be (both deliberate and accidental) dopants which compete for excitons and which have non-radiative decays. These are known as 'quenchers' or 'killers' and influence both the amount and time constant of the emitted light. This quenching can also be caused by mutual interactions between activator centres when the latter are present in high concentrations. As an example we find quenching effects start to appear in GS1 glass when the Ce_2O_3 fraction by weight exceeds 2%.

A further impurity or lattice defect may give rise to metastable levels in the forbidden gaps. These centres, known as electron 'traps' or 'colour centres', have the property of holding an exciton essentially indefinitely. They may be caused by an inpurity in the crystal or by the transformation or dislocation of atoms from the lattice due to the effects of ionizing radiation, in particular from highly-ionizing particles. They adversely affect the performance of the scintillator by reducing the energy transfer efficiency to the activator centres, by absorbing scintillation photons and thereby reducing the transparency of

the material, and by generating phosphorescent (long-time constant) light. Electrons trapped in these centres can be liberated by appropriate UV irradiation or heating (annealing) but, depending on the nature of the trapping centre, this may only offer a temporary cure. Annealing at a sufficiently high temperature can provide enough thermal energy for interstitial atoms to migrate through the crystal and recombine in vacant sites, thus returning the crystal to its undamaged state.

In summary we see that inorganic scintillators have the ability to transfer the ionization energy efficiently through the lattice to an activator centre where light emission takes place. In fact inorganic scintillators have the highest conversion efficiency of ionization energy into light, e.g. NaI (Tℓ) produces 40 γ keV^{-1}, or an efficiency of 12%, as compared with 3% for good plastic scintillators. Finally, the light is emitted $\leq$ 1 μm from the particle trajectory, i.e. it is local, in contrast with the situation for plastic scintillator/waveshifters.

3.3.2 Overview of properties

The first challenge facing inorganic SCIFI was to find materials which could be drawn into clad optical fibres. The work has focussed on scintillating glasses, originally[5] containing Tb^{3+} but now on glasses based on the Ce^{3+} activator (Refs. 5,9,10,39) since it has the shortest known decay time constant ($\tau \simeq 55$ ns). Table 5 presents a summary[10] of the properties of the cerium glass GS1, manufactured by Levy Hill Laboratories[40]. We mention that this and similar highly-crystalline glasses are difficult to manufacture and difficult to reprocess into fibres since the glass devitrifies readily, i.e. transforms to an opaque white crystalline ceramic.

3.3.3 Light yield and attenuation length

We observe, in GS1, 40 pe mm^{-1} for minimum ionizing particles, with an optical path length of 5 mm GS1, using a RCA 8850 quantacon phototube (bialkali photocathode). The calculated geometrical light collection efficiency is 28%.

We have also compared the responses of GS1 and a PVT plastic scintillator, NE102A, to highly ionizing particles. Using an ^{241}Am source (5.5 MeV α) we find, for GS1, a light yield of 40% relative to the yield of a minimum ionizing particle which deposits 5.5 MeV. Plastic scintillators show a far more serious saturation; our equivalent measurement with NE102A is 7%. This difference in response dramatically demonstrates the different scintillation mechanisms: the glass matrix efficiently conducts excitons away from the highly ionized region whereas the organic scintillator cannot and saturation occurs. This saturation is formalized by Birks law[23] which expresses the fluorescent light output per path length dx in a scintillator,

$$dI/dx = S\,(dE/dx)/[1+kB(dE/dx)] \ ,$$

where S is the scintillation efficiency, dE/dx is the specific energy loss and kB is the (Birks) constant, characteristic of the material, which represents the probability of quenching (by molecular interaction) relative to photon emission. Typical values for organic scintillators are kB = 0.01-0.015 gm cm^{-2} MeV^{-1}. For fast electrons one ion pair is produced every ~ 200 nm, i.e. ~ 200 molecular distances apart, and so quenching is negligible and dI/dx = S dE/dx. However, for 5.5 MeV α particles one ion pair is produced every ~ 1 nm, i.e.

Table 5

Properties of GS1 scintillating glass

Composition, by weight[1]:	SiO_2	55%
	MgO	24%
	Al_2O_3	11%
	Li_2O	6%
	Ce_2O_3	4%
Density, ρ	2.64 ± 0.1	g cm^{-2}
Mean refractive index (GS1 spectrum), n	1.586 ± 0.005	
Transition temperature	620	°C
Linear thermal expansion coefficient, α	75×10^{-7}	$°C^{-1}$
Radiation length, X_o	9.77	cm
Hadronic interaction length, λ	37.4	cm
dE/dx (minimum ionizing particles)	4.6	MeV cm^{-1}
Photon yield (minimum ionizing particles)	1.5 ± 0.5	photons keV^{-1}
Decay time constant, τ	55	ns
Wavelength of peak emission, λ_{max}	395	nm
Attenuation length	2-20	cm
Radiation hardness (see Section 3.3.4)	10^6	rads
Approximate cost	8	\$ US cm^{-3}

1. Levy Hill Laboratories, Ref. 39.

about 1 per molecule, resulting in strong quenching of the photon emission. Not only does GS1 have a good light yield for highly ionizing particles but it also has a high cross-section for slow neutron detection (via ^{7}Li capture). This and similar glasses are therefore used extensively in neutron experimentation[39].

The observed light yield vs. length in bulk GS1 is shown in Fig. 10. We see a sharp attenuation ($\lambda \sim 2.5$ cm) in the first 2 cm followed by a flattening to $\lambda \sim 20$ cm at the furthest distances. This behaviour is easily understood from the observed overlap of the excitation (absorption) and emission spectra (Fig. 11). We discuss in Section 6.4 the light yield and attenuation length of fibres of this glass.

In order to understand the cause of the poor attenuation, several samples of GS1 were prepared with different fractions of Ce^{3+}. The results of transmission measurements for these samples (Fig. 12) show the absorption is not due to an impurity in the host glass but is due to the Ce itself. However the poor quantitative agreement between Ce^{3+} concentration and transmission has led to the hypothesis that the Ce^{3+} may be partially oxidizing to Ce^{4+}, which is known to have a very strong optical absorption in this region. Quantitatively the poor transmission of GS1 would result if only 2% of the original Ce^{3+} was oxidized to Ce^{4+}. These considerations give hope that GS1 or an equivalent glass can soon be produced with a good attenuation length.

3.3.4 Radiation hardness

The transmission of GS1 after exposure to secondary radiation from external targets at CERN is shown in Fig. 13. Up to levels of $\sim 10^{6}$ rads we see relatively mild deterioration in transmission. At higher levels the glass becomes increasingly opaque to its scintillation light, although it remains fairly clear to visible light even at the highest exposure of 10^{8} rads. The good resistance of GS1 to radiation is due to the strong electron affinity of cerium, which inhibits the formation of colour centres by ionizing radiation. In fact cerium glasses are widely used in high radiation environments such as reactors. In the case of SCIFI detectors, it is necessary for both the core and cladding glasses to be resistant to radiation. We therefore anticipate that radiation-resistant SCIFI detectors will require a low refractive index cladding glass containing a small cerium admixture.

The temperature annealing of GS1 has also been investigated. The results (Fig. 14) show a mild recovery at 200°C and a substantial improvement at 400°C. This indicates there are prospects for recovering radiation-damaged SCIFI detectors providing they are constructed in such a way to allow disassembly and baking at high temperature.

3.3.5 Limitations and cures

The primary limitation of the Ce scintillating glasses is the very short attenuation length, as described above. It is now necessary to demonstrate that pure Ce^{3+} glass can be prepared in a suitably reducing environment and to measure the improvement in the attenuation length.

There are two other potential drawbacks with glass SCIFI. The first is the slow scintillation time constant of 55 ns. In the case of readout using image intensifiers and phosphors this actually presents no limitation since the fastest phosphors (which also, in fact, contain Ce)

have a similar time response. The second is the short radiation length of 9.8 cm, which may lead to an unacceptable amount of material in certain applications.

3.4 Liquid scintillator

There are two separate developments involving fibres filled with liquid scintillator:

1. Glass capillaries. Small (6 x 6 x 12 mm^3) active targets have been made from fine glass capillaries fused into a coherent bundle[11]. The fibres have 60 μm pores and provide an open volume of 50% which may then be filled with liquid scintillator (see Table 1) by capillary action. A yield of 4 hits (pe) mm^{-1} for minimum ionizing particles is observed using an image intensifier. The attenuation length is very short (~ 2.5 cm).

2. Teflon tubes. Extruded teflon FEP tubes, of outer diameter 5 mm and wall thickness 0.4 mm, have been used to read out electromagnetic calorimeters[17]. They were filled with NE235 scintillator[25] of refractive index 1.47. In association with teflon (n = 1.38) this gives an approximate trapping efficiency in each direction of 3.1%. The light yield after a path length of 2 m was found to be (20 ± 4) γ per MeV deposited in the scintillator (equivalent to 1 pe mm^{-1}), with a good attenuation length λ = 140 cm. The light yield showed no significant deterioration after irradiation up to 10^5 rads (a drop of 20% in the attenuation length was observed at 10^5 rads) but at the highest doses (4 x 10^6 rads) the teflon had become brittle and the transmission was very poor. Further development of this technique is taking place[37] using alternative materials in place of teflon.

4. SCIFI MANUFACTURE

The production of SCIFI from bulk plastic or glass scintillator is illustrated in Fig. 15. (The dimensions shown on this figure refer to the glass SCIFI targets discussed in Section 6.4.). The whole process must take place under clean conditions since dust particles render fibres useless.

The first step (Fig. 15a) is to prepare a preform comprising of a polished scintillator core around which is placed a cladding. The cladding can either be an extruded material, with inner dimensions closely matched to the core, or, in the case of the Saclay plastic fibres, a coating of polyvinyl acetate which is applied directly to the polished surface of the core scintillator. The ratio of the physical dimensions of the core and cladding are preserved throughout the drawing processes and must be properly chosen at the outset. The preform may be completed by a thin EMA coating which, for glass SCIFI, is an opaque black glass. All preform materials must have proper matching of physical properties such as softening points, expansion coefficients, etc. The final preform weighs from 0.1 kg up to several kg, depending on the material and capacity of the pulling station.

The preform is slowly inserted through the top of an oven (Fig. 16) where it is heated to the appropriate softening temperature. The lower tip of the preform is then caught and pulled downwards to form fibres. These fibres may be cut into lengths of several metres or, in the case of plastic SCIFI, stored on a drum. (Saclay stores on each drum a single 1 mm diameter fibre of length 0.6 km from each preform weighing ~ 0.5 kg.)

An automatic measurement of the fibre diameter provides feedback control of the pulling speed and oven temperature. Good pulling stations produce fibres with diameter variations of ~ 1%, whereas the best stations can achieve ~ 0.1%.

The first draw (Fig. 15b) produces single fibres of diameter ~ 1 mm which can be used directly for calorimetry or moderate-resolution tracking. In order to make finer fibres a second draw (Fig. 15c) is necessary. This involves the manual assembly of a set of single fibres (typically 100-200) into a mechanical fixture which holds them in a precise array. After the second draw a multifibre bundle is obtained, with individual fibres of the required small diameter (~ 25 μm) which are fused together by their cladding/EMA. The last process (Fig. 15d) is to assemble the multifibre bundles into a device of the required dimensions and to bond them with epoxy or by fusion (heat). The final preparation involves optical polishing of the output faces.

Microphotographs of glass SCIFI targets manufactured[41] by this process are shown in Figs. 17 and 18. (These targets are used by Ref. 10 as described in Section 6.4.) The later targets (Figs. 17b and c) are seen to have reasonably good coherency (parallelism to < 1 fibre diameter over the length of the fibres). However we can see by comparing Fig. 18 with Fig. 19, which shows the near-perfect regularity of a fibre-optic plate used in image intensifiers, that there is room for further improvement.

5. READOUT

5.1 Overview

In order to be sensitive to the single-photon signal levels which are characteristic of SCIFI, the readout system must have a photon gain of ~ 10^5 in addition to an imaging capability. This is achieved by image intensifiers of typically three stages where at least one involves a micro-channel plate (MCP) to provide both high gain and a fast gating capability. After intensification the image is generally stored on a charge-coupled device (CCD) from where it may be either read out in ~ 10 ms or fast-cleared in ~ 1 μs. Fibre-optic coupling is used between all the optical stages to ensure the highest efficiency and simplicity of assembly.

This approach has certain advantages, such as:

1. High degree of multiplexing. One image intensifier/CCD channel handles up to 10^5 fibres.

2. Good physical match between narrow diameter (25 μm) SCIFI, image intensifier resolution (50 μm spot diameter) and typical CCD pixel size (20 × 20 μm^2). (SCIFI of larger diameter may be read out with a demagnifying image intensifier.)

3. Low geometrical distortions.

However, there are also some drawbacks associated with image intensifiers, such as:

a) Rate limitation. The fastest phosphor (P47, Ref. 42) has a time constant τ = 35 ns. In a three-stage tube this implies a minimum integration time of 100-150 ns.

b) Finite lifetime. Both the MCP and the photocathode deteriorate with time, due to ion bombardment. The gain lifetime (1/e) is typically limited to a charge of $\lesssim$ 0.05 Coulomb cm^{-2} on the phosphor. (An ion barrier film over the MCP input face can increase this value by an order of magnitude.) These charge limitations can readily be exceeded over the duration of an experiment unless careful attention is paid to gating and minimization of system gain.

c) Cost. The minimum cost of a single image intensifier system suitable for single photon detection is ~ 30 KSF.

d) A certain 'touchiness' in operation. This is a subjective but nevertheless valid comment. It is not unrelated to item c).

In addition to the standard image intensifier/CCD readout chain there are a great variety of electronic imaging systems which could be adapted to SCIFI readout. The most useful is probably the SIT (silicon-intensifier target) tube preceded by suitable image intensification, known as the ISIT. The SIT tube accelerates electrons from a photocathode to about 10 keV before they strike a silicon wafer target. In this way the tube has a charge gain of ~ 1000. The silicon target is a diode array of 14 x 14 μm^2 pixels which can be read out in a few msec by means of an electron beam scanning the back face.

A recent development of multi-anode phototubes by Hamamatsu[43] (R2594-95 and R2486-89) and by Philips[44] (XP4702) provides a potentially attractive future alternative to the readout of moderate diameter ($\geq$ 1 mm) SCIFI. As an example, the Philips tube has an array of 64 (8 x 8) anode pads of spacing 2.54 mm. The dynode structure is formed by a set of thin parallel electrodes spaced by 0.2 mm and containing aligned holes of 300 μm diameter with a centre-to-centre spacing of 770 μm. The device is very compact: 35 mm deep x 50 mm diameter. Initial measurements[45] show a gain of 10^7 and low (< 5%) cross-talk with the nearest neighbour. After further development this class of device, with suitable VLSI electronics, offers the future possibility of a robust, high-speed readout system for SCIFI imaging calorimetry or moderate resolution SCIFI tracking. Finally, for readout of coarse SCIFI calorimetry, the traditional phototubes or Si diodes can be used.

We will return to the readout devices in Section 10 where we look at their operation in a supercollider detector. However we will now describe two present readout systems which have been used to obtain some of the experimental SCIFI results of the following section.

5.2 Examples of SCIFI readout systems

The UA2 SCIFI detector[6] readout is shown in Fig. 20. It involves a three-stage image intensifier[46] as follows:

1. II1: electrostatic focus, 80 mm input diameter, 18 mm output diameter, S20 photocathode, P47 phosphor.

2. II2: gated proximity focus MCP, 18 mm diameter, S20 photocathode, P47 phosphor.

3. II3: electrostatic focus, 18 mm input diameter, 7 mm output diameter, S20 photocathode, P46 phosphor.

The overall linear demagnification is 0.08 and the operational photon gain is 0.4 10^5. The gain lifetime of tube II2 was measured to be an integrated charge of 5.5 x 10^{-2} Coulombs cm^{-2} at the phosphor. The decrease in gain was found to be caused by equal losses in the photocathode quantum efficiency and in the gain of the MCP. The CCD is a Thomson TH 7852 [47] (active area 4.3 x 5.8 mm^2 and pixel size 30 x 19 μm^2). This project has included the important development[48] of the fast clear (1 μs) of the CCD using the antiblooming diodes adjacent to each pixel.

The CERN-MPI-RAL[10] SCIFI readout is shown in Fig. 21. This involves a four-stage (for film recording) or three-stage (CCD recording) image intensifier as follows:

1. Stages 1-2-(3): proximity focussed diodes[49], 25 mm diameter, bialkali or S20 photocathodes, P20 or P11 phosphors.

2. Final stage: gated proximity focus MCP, 18 mm diameter, S20 photocathode, P20 phosphor.

The system has unit magnification and an overall photon gain of ~ 10^5 (three stage). The CCD is a Thomson TH7861 (active area 6.6 x 8.8 mm^2 and pixel size 23 x 23 μm^2).

The CCD data acquisition system is shown schematically in Fig. 22. A local preamplifier and control unit clocks analogue data out of each pixel sequentially. This data is fed to a 'frame grabber' or 'frame storer' which digitizes the data in a FADC, suppresses low channels and stores the pulse heights and addresses of the remaining channels into RAM. Typically a clock frequency of 10 MHz is used and the readout of a single frame takes ~ 10 ms.

6. EXPERIMENTAL STATUS OF SCIFI TRACKING DETECTORS

6.1 Plastic SCIFI: Cambridge-CERN-Orsay-Saclay-UA2

A large SCIFI detector (the 'SFD')[6] is under construction as part of the UA2 upgrade programme for the SPS Collider with ACOL. A SCIFI detector was chosen since it provides compact tracking and pre-shower information while allowing sufficient room for a transition radiation detector in the restricted space of the UA2 inner detector. The device involves plastic fibres[3] of diameter 1 mm and length ~ 235 cm arranged into a cylindrical detector of length 210 cm and mean radius 41 cm. The EMA for each fibre is provided by a sputtered aluminium layer of thickness 100 nm. The fibres are oriented into stereo triplets (with angles 0, ±α relative to the beam axis); 6 triplets (with α = 275 mr) precede a 1.5 X_0 Pb converter sheet and 2 triplets (with α = 367 mr) follow, to provide a total of 24 layers of fibres. The operational mean detection efficiency per single fibre layer is 91% for minimum ionizing particles which cross at 90°. This corresponds to 3.8 pe mm^{-1} at the photocathode of the first image intensifier stage. The SFD involves in total 60 K fibres (140 km) which are read out with 32 image intensifier/CCD units. At the (80 mm diameter) entrance face of the image intensifier chain (Section 5.2) each fibre is inserted into a drilled plate with holes of 1 mm diameter spaced by 1.3 mm between centres. The system will be triggered at 2.6 x 10^5 Hz and can be read out at up to 200 Hz.

The SFD prototype is producing some very nice results as we shall now see. Some typical (40 GeV) electron events are shown in Fig. 23.

These events clearly demonstrate the suitability of SCIFI to imaging calorimetry. The sensitivity can be easily understood. A high energy electron radiates $1 - e^{-1.5} = 78\%$ of its initial energy in crossing a 1.5 X_0 converter. This appears in a characteristic soft (1/E) spectrum of photons which, in turn, generate electrons by Compton scattering, pair production, etc. A SCIFI array has an excellent sensitivity to this soft cascade since the energy threshold is very low (1 pe per ~ 35 keV deposited energy).

The clear separation between π and e responses in the preconverter fibres is shown in Fig. 24. After correcting for beam contamination, the πe rejection at 40 GeV is measured to be 7.3×10^{-2} at an electron detection efficiency of 98%. The performance is essentially unchanged at 10 GeV (Fig. 25): a πe rejection of 7.3×10^{-2} at an electron detection efficiency of 96%.

The measurement precision of the SFD is illustrated in Fig. 26a. The track residuals in the first 18 layers have σ = 0.35 mm. The fitted curve also includes two satellite Gaussians (σ = 0.58 mm) which reflect a 2 x 3% probability of cross-talk to a neighbour in the readout system. In order to obtain these results the positive (pincushion) distortions in the electrostatically-focussed image intensifier system had first to be corrected. The maximum magnitude of the distortion is 13%: 1 mm in space (i.e. 1 fibre diameter) is equivalent to 70 μm at the centre of the CCD and to 80 μm at the edge of the CCD. The distortions are effectively corrected using a magnification proportional to a polynomial in radius (R mm) at the input to the image intensifier of the form: $r = 0.070\ R\ (1 + 2.0 \times 10^{-6}\ R^3)$, where r (mm) is the radius measured at the output by the CCD. This function is determined by means of a matrix of illuminated fiducial fibres.

Finally the shower location precision is indicated in Fig. 26b. This shows a transverse matching precision σ = 0.76 mm between a candidate electron and a shower. This precision is necessary to reject false electron signals due to the overlap of a π and γ.

6.2 Plastic SCIFI: Washington University, St. Louis

A SCIFI range detector[7] for heavy nuclei has been developed jointly by Washington University and Fibre Optic Development Systems, Inc.[50]. The detector is made from 100 x 100 μm^2 square fibres of polystyrene scintillator (KST1-415), with an acrylic cladding of thickness 7 μm and no EMA. These fibres are arranged into coherent bundles of cross-section 2.7 x 2.7 cm^2 and length 30 cm. The readout chain is as follows: fibre optic reducer (40 mm to 18 mm diameter), dual MCP image intensifier (photon gain up to 10^6), fibre optic reducer (18 mm to 11 mm diameter) and finally a CID readout sensor (pixel dimensions 23 x 27 μm^2).

A typical event is shown in Fig. 27. Near to the end of the nuclear range the optical FWHM of the track is approximately 8 fibres, i.e. 800 μm, whereas the physical region of energy deposition is less than 1 fibre width. This is an experimental demonstration of the broadening process shown in Fig. 6b and a measurement of the absorption length of the waveshifter in this plastic scintillator. Although the fibres were found to have an attenuation length of only 11 cm, recent improvements of the procedure and of the scintillator have increased this to 60 cm.

The track residuals of a single ^{56}Fe event are shown in Fig. 28. The small r.m.s. residual error (σ = 35 μm) is a consequence of the large energy deposition. There may be evidence in Fig. 28 for a

further potential improvement if the longitudinal correlations are due to fibre incoherency and not a smoothing due to fibre cross-talk.

6.3 Glass SCIFI: Notre Dame-Fermilab

A SCIFI active target has been developed[5] for Fermilab experiment E687 to observe the photoproduction and decay of heavy-flavoured particles. The target is made[41] from 25 x 25 μm^2 square fibres of GS1 glass[40] with N51A cladding and an EMA. The readout involves a two-stage electrostatic focus image intensifier followed by a gated proximity focussed MCP stage. The overall photon gain is 2 x 10^5. The output is fibre-optically coupled to a Fairchild CCD 3000F CCD camera.

An interaction recorded on photographic film (Fig. 29) shows the potential for the high resolution SCIFI detector to become an 'electronic' bubble chamber. The observed spot frequency for minimum ionizing particles is 4 mm^{-1} in a 1 cm deep target with the opposite face polished and aluminized. The track residuals show a r.m.s. deviation of 28 μm.

6.4 Glass SCIFI: CERN-MPI(Munich)-RAL

This group has been developing[10] the application of glass SCIFI to active targets and compact, precise tracking in collider detectors. The targets[40,41] and readout are already described in Sections 4 and 5.2. The essential features are the fibre size, 25 x 25 μm^2, and length, 25 mm.

Examples of some events recorded with photographic film (Kodak 2475) are shown in Figs. 30 and 31. These photographs dramatically demonstrate the importance of an EMA to absorb the untrapped scintillation light.

Measurements of the spot size using photographic film (Fig. 32) and CCD (Fig. 33) indicate a FWHM of 52 ± 4 μm. The spot size is found to be only weakly dependent on its total brightness (Fig. 34). This behaviour is desirable since it implies that the two track resolution of 52 μm will not be strongly affected by increases in the gain of the readout system.

An example of the track residuals distribution is shown in Fig. 35. The residuals distribution has been investigated at various depths onto the target. The results (Fig. 36) show a constant r.m.s. residual, σ = 22.3 μm. This indicates that the fibres are parallel to better than one fibre diameter over the length of the target, in agreement with optical measurements (Figs. 17 and 18).

The light yield and attenuation length has been measured using the gap length distribution (Fig. 37) familiar in bubble chamber analyses. The results (Fig. 38) show a yield of 2 pe mm^{-1} at zero length and an attenuation length of 29 mm. This initial short attenuation length is confirmed by UV measurements made on long individual multi-fibre bundles (Fig. 39). At longer distances the fibres display an attenuation length of ~ 25 cm. This figure sets a lower limit on the attenuation length caused by scattering losses in the fibres, as opposed to absorption losses.

SECTION II: TOMORROW .....THE SUPERCOLLIDER

7. THE CHALLENGE OF THE SUPERCOLLIDER ENVIRONMENT

The next threshold in our understanding of the laws of nature is widely expected to lie in the energy range below 2 TeV. This requires an e^+e^- machine with $\sqrt{s}$ = 2 TeV or a hadron collider with $\sqrt{s} \geq$ 12 TeV and, for both machines, a luminosity, $L = 10^{33}$ cm^{-2} s^{-1}. Proton-proton colliders apparently can be built to these specifications using present technologies. The question is: Can the experimenter work in such a harsh environment?

The hadron supercollider environment (Table 6) is characterized by:

1) High energy
   - Multi-TeV individual particles.
   - Multi-TeV jets, with a high multiplicity and high density near the jet core (Fig. 40).

2) High luminosity
   - > 10^8 Hz event rate.
   - Multiple interactions per crossing.
   - High particle fluxes (cm^{-2} s^{-1}).
   - High radiation doses to the detector.

Almost all current detectors would suffer serious limitations in this environment. For this reason we must not only extend the performance of existing detectors but also explore alternatives and new technologies in search of a breakthrough. It is the aim of this section to explore the possibilities for SCIFI in tomorrow's supercollider detector.

8. THE SCIFI MICROTRACKER CONCEPT

8.1 Is tracking necessary?

It is worthwhile first to examine the need for tracking in a supercollider detector. It is easy to see that early experiments or those at ultra-high luminosities (10^{34} cm^{-2} s^{-1}) will include 'beam-dump' styles of detectors, which include only calorimetry or a passive absorber followed by a muon spectrometer. It is equally easy to see that, without an inner tracking device, the overall performance of a detector will be substantially reduced, and a great deal of physics will be inaccessible or ambiguous. Tracking (in many cases associated with a magnetic field) provides the following:

1. Electron identification and measurement (charge, p/E match and elimination of backgrounds such as $\pi\gamma$ overlaps or e^+e^- pairs).

2. Improved muon identification and measurement (track vector before the absorber and P_{inner}-P_{outer} match to reject hadron decays and punch-throughs).

3. Measurement of jet charged multiplicity. This is important, for example, in helping to tag the presence of a W [52]. A 1 TeV W still has $\langle n_{ch} \rangle \sim 17$ but a qg di-jet of 1 TeV energy has $\langle n_{ch} \rangle \sim 75$.

4. Tagging of heavy flavour production by the presence of a secondary decay vertex.

Table 6

The supercollider experimental environment

	CLIC	LHC		SSC
Beam particles	e^+e^-	pp		pp
Luminosity	10^{33}	$1.4 \times 10^{33} \rightarrow 10^{34}$		10^{33} cm^{-2} s^{-1}
$2 \times E_{beam}$	2	16	16	40 TeV
Bunch spacing	170 μs	25	5	16 ns
Interaction rate	10^{-3} *	$1.4 \times 10^{8} \rightarrow 10^{9}$		10^{8} Hz
<Interactions> crossing^{-1}	$1.7\ 10^{-7}$ *	3.5	5	1.6
$<n_{ch}>$ event^{-1} (p_T > 0.5 TeV/c)	~ 60	~ 100	~ 100	~ 100
$<n_{ch}>$ cm^{-2} in jet core (r = 10 cm)	-	10	10	10
$<n_{ch}>$ crossing^{-1}	-	~ 200	~ 260	~ 120
$<n_{ch}>$ cm^{-2} s^{-1} (r = 10 cm)	-	$1.4 \times 10^{6} \rightarrow 10^{7}$		10^{6}
Radiation dose yr^{-1} (r = 10 cm)	-	10^{6}	10^{7}	10^{6} rads

* Single photon annihilation.

5. Measurement of z vertex positions and correct association of calorimeter energy with the corresponding signal or background vertex.

6. Independent measurement of jet directions and charged energy (redundancy, calibration and cross-check of calorimeter measurements, especially for rare events where the maximum event information is needed).

8.2 The need for a new approach

Present high-energy collider detectors, such as DELPHI or ALEPH, utilize giant superconducting solenoids of typical dimensions 7 m (length) × 5 m (diameter) and field strengths 1.2-1.5 T. The main factor which leads to these large dimensions is the requirement to measure momenta up to ~ 100 GeV/c. In order to achieve this goal, the central trackers, which comprise drift chambers or TPCs with measurement

precisions of 100-200 μm, must extend over a radial distance of 1-2 m. It is the large size of these inner systems which sets the enormous scale and cost of the overall detector. Future detectors which adopt this approach for the supercollider, where the momenta will be ≲ 1 TeV, will require even larger solenoids.

We argue that the combination of two new technologies can provide a dramatic reduction in the scale of future collider detectors. These technologies are as follows:

1. Precise micro-trackers such as SCIFI or Si micro-strips.

2. Superconducting solenoids with ultra-high (6 T) magnetic fields.

We can estimate the potential reduction in detector size. The momentum accuracy (σ_p/p) above a few GeV/c is proportional to $\sigma_s p/BL^2$, where σ_s is the sagitta measurement error, B is the field strength and L is the tracking lever arm. We will take the following representative values:

1. Today's detector (TPC or DC tracking): $\sigma_s = 100$ μm, $B = 1.5$ T, $L = 100$ cm

2. Tomorrow's detector (SCIFI tracking): $\sigma_s = 5$ μm, $B = 6$ T, $L = L_{new}$

In order to achieve the same performance for σ_p/p, tomorrow's detector needs a tracking lever arm of:

$$L_{new} = 100 \text{ cm } \sqrt{\left[\frac{5 \text{ μm}}{100 \text{ μm}} \times \frac{1.5 \text{ T}}{6 \text{ T}}\right]} = 11 \text{ cm} ,$$

i.e. a reduction by almost one order of magnitude.

A similar calculation can be performed for the low-energy region. Here multiple coulomb scattering (mcs) dominates the momentum precision and σ_p/p (mcs) $\propto \sqrt{X/BL}$, where X is the tracker thickness between the first and last measurement planes, expressed in radiation lengths (r.l.). We will assume for today's detector X = 2.5% r.l. and for tomorrow's detector X = 2.0% r.l. [equivalent to an 8 mm plastic scintillating fibre 'superlayer' or 6 layers of silicon]. This indicates a reduction in size by a factor of 4 is possible at constant σ_p/p (mcs).

We can summarize as follows:

- The combination of a precise SCIFI micro-tracker with an ultra high field superconducting solenoid can lead to a reduction in linear dimension of the central tracker by about one order of magnitude, while maintaining the same momentum measurement precision.

- This will result in a substantial reduction in the cost and size of subsequent detector elements (calorimeter solenoid, muon spectrometer, etc.).

- Furthermore the overall performance of the detector will be significantly improved with respect to:

a) Calorimetry, since a deep uniform calorimeter and expensive materials become economically practical.

b) Electron identification, by the detection of synchrotron photons[51]. The key advantages of a strong B field are that the energy loss to synchrotron photons $\propto B^2LE_e^2$ and the mean photon energy $\propto BE_e^2$, where E_e is the electron energy. This is discussed further in Section 9.5.

8.3 Design criteria

The supercollider environment of high energy and high luminosity places the following requirements on a charged-particle tracking device:

1. Precise measurement accuracy (to measure momenta and secondary decay vertices).

2. Fine two-hit resolution/high granularity (to resolve particles in jets, to handle multiple events and multiple z vertices and to identify e^+e^- pairs).

3. Radial compactness/high density of measurements (hits) per unit path length (to reduce the overall cost and to maximize the performance of subsequent detector components).

4. Radiation hardness (both of the device and the local electronics).

5. Fast response/high rate capability.

6. Good pattern recognition capability (to minimize the computer time for event reconstruction).

SCIFI tracking is potentially capable of meeting all these design criteria, as we discuss below.

8.4 Design and performance

A SCIFI micro-tracker (Fig. 41) is built of three or more concentric cylindrical 'superlayers' constructed from coherent arrays of narrow (25 μm) diameter fibres. The outer radius is only 30-50 cm. Each superlayer consists of 4 layers, each 2 mm thick, made from fibres arranged in the directions z-u-v-z. The u and v fibres form a narrow angle stereo of ±50 mrad with respect to the z fibres, which lie parallel to the beam axis. The perpendicular material in each superlayer is 2% X_0 (plastic) - 8% X_0 (glass). With a yield of 5 hits per mm there are a total of 40 hits per track in each superlayer.

This geometry results in excellent track reconstruction since each superlayer measures local track vectors in space (three-dimensional position and angle) and in momentum (by impact parameter relative to the beam axis). For example, inside a superlayer the azimuthal angle precision, σ_ϕ = 0.6 mr, and the momentum precision, σ_p/p < 1% p. Unambiguous linkage of the track vectors between superlayers can therefore be made. In addition the vector stubs of (uninteresting) low energy tracks can be rejected at an early stage of event reconstruction.

In association with an ultra high field (6 T) solenoid, a compact SCIFI tracking system can achieve remarkable performance (Table 7). With a lever arm of 30 cm and assuming a measurement accuracy per hit σ = 15 μm and a systematic sagitta error of 10 μm, the momentum precision is

$$(\sigma_p/p)^2 = [5 \times 10^{-4}\ p(\text{GeV/c})]^2 + (0.01)^2 \ .$$

This is sufficient for sign measurement at 1 TeV/c.

Table 7

SCIFI micro-tracker performance

Number of hits per track	120
σ_{xy} hit^{-1}	15 μm
Two-hit resolution	50 μm
σ_{xy} (impact parameter at origin)*	< 20 μm
σ_z (vertex) track^{-1}	100 μm
$(\sigma_p/p)^2$	$[5 \times 10^{-4}\ p\ (\text{GeV/c})]^2 + (0.01)^2$

* p > 20 GeV/c

9. ALFIE: THE ALL FIBRE EXPERIMENT

9.1 Overview

SCIFI has important potential applications in a supercollider detector beyond the micro tracking system which we have just described. In order to illustrate these possibilities we have assembled a supercollider detector named ALFIE (All Fibre Experiment), based on the concepts presented in the previous section, which is completely read out with plastic SCIFI. The components of this detector (Figs. 42 and 43) are as follows:

1. A compact central detector, located inside an ultra high field superconducting solenoid of inner radius 60 cm, which comprises of:
   a) Micro-tracker.
   b) Charge-flow detector.
   c) z-vertex detector.
   d) Micro-converter.
2. A Pb/SCIFI electromagnetic and hadronic calorimeter.
3. A muon spectrometer comprising of magnetized iron absorber and large area SCIFI sheets.

We will now discuss each of these components in more detail.

9.2 Micro-tracker

This is constructed from plastic SCIFI in a similar fashion to the micro-tracker described previously. The device has five cylindrical superlayers with the first two comprising only of z fibres and the last three including u and v fibres. The function of the innermost layers is to identify the presence of heavy flavoured quarks or new long-lived particles by means of secondary decay vertices. The innermost fibre layer, which is situated at a radius (r) of 10 cm, receives a radiation dose of 10^6 rads per year and so must be replaced at yearly intervals. The situation quickly improves with increasing radius, e.g. the 3rd layer at r = 20 cm has a lifetime of four years.

9.3 Charge-flow detector

This detector (Fig. 44) measures the 'flow' of charged particles, without any attempt to resolve individual particles, in analogy with the measurements of energy-flow in calorimeters. The plastic SCIFI of diameter 1 mm are arranged parallel to the z axis in a cylindrical shell geometry.

The jets are measured by pulse height analysis of the SCIFI light output. In this way a simple yet relatively high resolution (in comparison with calorimetry) analysis of jet directions, widths and charged multiplicities can be made. The particular merit of this approach is the absence of any saturation of SCIFI response for essentially all jet flux densities, in contrast with the space charge limitations of wire chambers. (We remark here that, in an actual experiment, the charge-flow detector or the micro-tracker would be used, but not both.)

9.4 z-vertex detector

The z measurement of the event vertex will be important since the average beam crossing at a supercollider will contain 3-5 interactions. In these simultaneous interactions the only way to associate calorimeter cells with a common event and to reject background cells is by tracking back to the z vertex. This capability may be of crucial importance in the case of rare events which, for example, could be faked by the chance occurrence of two simultaneous high p_T interactions.

The z-vertex detector (Fig. 45) is constructed in a similar way to the charge-flow device but with the fibres arranged in circles, perpendicular to the beam axis. The readout face, which runs along the length of the chamber, is connected to the optoelectronic readout chain via non-scintillating coherent fibre bundles.

9.5 Micro-converter

A powerful potential application of SCIFI is an imaging pre-converter for photons and electrons (Fig. 46). The 'micro-converter' is made from plastic fibres of diameter 1 mm embedded in a medium of thin high-Z converters, e.g. Pb foils or Woods metal, of a total thickness ~ 3 X_o. The SCIFI/Pb volume ratio is $\geq$ 50% to ensure a very low threshold for photon detection. We can estimate this threshold to be ~ 5 MeV as follows. If we have a SCIFI/Pb volume ratio of 50% then the scintillator samples ~ $(dE/dx)_{SCIFI}/(dE/dx)_{Pb}$ = 1.7/11.7 = 14% of the total dE/dx. Therefore a photon (electron) of 5 MeV will deposit in the scintillator 5 x 0.14 = 0.6 MeV. The yield of plastic SCIFI is 1 pe per 35 keV deposited energy. Therefore a 5 MeV photon (electron) will produce a light pulse of 600/35 = 17 pe. In reality, the micro-converter has a finite granularity of 1 mm and so we must consider

the electron range. For a 2.5 MeV electron the range in Pb is ~ 2 mm so we expect at least one fibre crossing for both the electron and positron, i.e. a yield of 10 pe. At slightly higher incident energies the SCIFI micro-converter will image the photon conversions; the e^+e^- tracks will scatter in the converter and curl in the magnetic field.

The first application illustrated (Fig. 46a) for this device is to identify the presence of a nearby π and γ which could lead to false electron candidates in the relatively coarse-grained cells of the electromagnetic calorimeter. In addition to rejection of this background, the SCIFI micro-converter can make a positive electron identification in two ways (Fig. 46b):

1. Initiation of the electron shower in the thin pre-converter.

2. Identification of hard synchrotron photons radiated in the ultra-high magnetic field.

The characteristics of the synchrotron light radiated by an electron in a 6 T magnetic field over a path length of 30 cm are as follows: number of photons (independent of E_e) = 11, total synchrotron energy E (keV) = 14 E_e^2, critical energy E_c (keV) = 8 E_e^2 and mean photon energy E_γ (keV) = 1.3 E_e^2, where E_e is expressed in GeV. This shows the potential presence of a very powerful technique (in addition to calorimetry) for the identification of high energy electrons, namely the detection of hard (MeV) synchrotron photons which are located in a well-defined position along the tangent to the electron track. For a γ threshold of 5 MeV, we can see (Fig. 47) the threshold for electron identification is 30-40 GeV; lowering of the γ threshold would lead to a corresponding reduction in the electron identification threshold. The SCIFI tracking layers will be essentially transparent to photons of these energies ($\geq$ 5 MeV) and so most will reach the micro-converter. Photons which convert in the tracking layers will of course be detected with good efficiency and will aid the identification of electrons. This technique for electron identification is of particular importance since most of the alternative techniques, such as transition radiation or matching between the calorimetry energy and incident momentum, are of little benefit above ~ 100 GeV. At these energies, wherein lies the key physics, the only positive experimental signatures of an electron are longitudinal shower profile and production of hard synchrotron photons. Finally we comment that the radiation of photons in the material of the SCIFI tracker will increase the apparent synchrotron flux and aid the identification of the electron.

The final application of the SCIFI micro-converter (Fig. 46c) concerns the identification of single high p_T photons. Here the major background is from high energy π^o or η production which leads to two or more nearly-coincident photons. A two-shower resolution of 150 μm will allow π^o identification up to ~ 1 TeV.

9.6 Calorimeter

The calorimeter involves a matrix of parallel, 1 mm diameter plastic SCIFI embedded in Pb or Woods metal[12-14]. The volume ratio Pb/SCIFI is ~ 3/1 depending on the exact composition of the absorber and readout, as discussed below. The entire calorimeter is made from material of the same density. The calorimeter is divided longitudinally by cutting fibre blocks of the appropriate thickness, followed by machining and polishing of the entrance and exit faces. In the electromagnetic section (30 X_o) these blocks may have thicknesses of

5 X_o, 20 X_o and 5 X_o in order to follow the shower profile and to check for (hadron) penetration and the exit. The hadronic section (a total of 12 λ) is also segmented longitudinally.

The fibre directions lie approximately radially in the barrel region and along z in the end cap region. In this geometry the fibres are approximately, but not exactly, pointing to the interaction region and so particles cannot travel the length of a single fibre and avoid the absorber material. The readout is accomplished with small waveshifter plates, each with two photodiodes attached to opposite edge faces (Section 10.2), which are arranged in a mosaic at the outer surface of each layer. With this approach the transverse granularity and cell shapes can be simply chosen or later modified, since the calorimeter medium itself has no fixed internal boundaries.

The advantages of this calorimeter are as follows:

1. High density. For a Pb/SCIFI volume ratio of 3/1 the radiation length X_o = 7.4 mm and the interaction length, λ = 21.3 cm.

2. Fast. The signal integration time is < 20 ns and the individual cell times can be determined to < 1 ns.

3. Hermetic and uniform. Internal dead regions or 'cracks' are absent.

4. Inexpensive materials and relatively simple construction compared with other calorimeters such as liquid argon or TMP.

5. Good electromagnetic and hadronic energy resolution.

6. Readout system which is compact, simple, flexible and stable in operation.

7. 'Compensated', i.e. relative electron/hadron response = 1.

8. Radiation hard to a level sufficient for operation in a supercollider detector.

We will elaborate further on the final three points. Wigmans[53] has recently clarified the mechanisms which influence the responses of calorimeters to electrons and hadrons. The responses depend on several parameters which include not only the absorber material, as was naively previously considered, but also the readout material and the relative amounts of each. The most important conclusion from this work is that compensating calorimeters can be made from absorbers other than uranium, a material which is expensive and difficult to handle. Compensation (e/π = 1) can be achieved by a variety of high Z absorbing materials, which suppress the electron response (by preferential absorption of photons in the Compton and photoelectric region) and boost the π response (by providing a good source of low energy neutrons which can be preferentially detected in the readout material). The situation is shown in Fig. 48. Here we see the general improvement in the e/π ratio towards unity as the Z of the absorber increases. However to be able to achieve e/π = 1 requires a readout material with a high cross-section for thermal neutrons, i.e. to contain free hydrogen atoms. This is the case for liquid TMP, and for plastic scintillator. In these materials, by altering the absorber/readout volume ratio, the neutron/minimum-ionizing particle ratio can be tuned through a wide range and compensation can be achieved. Specifically this will occur in a Pb/SCIFI calorimeter with a volume ratio of 3/1.

In order to have a good energy resolution in the electromagnetic section it is necessary to sample finely; 2 mm Pb will give an electromagnetic energy resolution, $\sigma_E/E = 12\%/\sqrt{E(GeV)}$. In a conventional approach, involving alternate plates of Pb and scintillator, this would require scintillator plates of thickness < 1 mm in order to maintain the required Pb/scintillator volume ratio of 3/1. Such plates are difficult to handle and have a poor transmission which would result in large transverse non-uniformities. (The transmission in very thin scintillator plates could, in principle, be improved by coating with a 'cladding' layer.) SCIFI, however, is well-matched to these simultaneous requirements of fine sampling thickness and uniform response (long attenuation length).

The radiation dose at the entrance to this calorimeter (r = 100 cm) is 10^4 rads year^{-1} (3×10^{11} minimum ionizing particles cm^{-2} year^{-1}). If we assume the mean photon energy is ~ 1 GeV then at shower maximum there will be ~ 10 particles per incident photon and the dose will be ~ 10^5 rads year^{-1}. On this basis we see that plastic SCIFI must perform reliably up to doses of 10^6 rads. This is a reasonable expectation based on present performances and new materials (Section 3.2) and considering the short fibre lengths involved. The radiation dose in the hadron calorimeter will be approximately an order of magnitude less (i.e. < 10^4 rads year^{-1}) because of the larger radial distance and the reduction in mean number of particles at shower maximum.

9.7 Muon spectrometer

The entire ALFIE inner tracking detector, solenoid and (12λ) calorimeter is contained within a radius of 3.6 m. Beyond this is located a muon spectrometer. The dimensions of the muon system are enormous and incompressible since it is necessary to have 4-5 m magnetized Fe to absorb sufficiently the multi-TeV jets and to provide a 15% measurement of the muon momenta. Tracking chambers made of SCIFI sheets are used in the muon spectrometer. The purpose of this exercise is not to argue that the SCIFI is better than conventional large area drift chambers but simply that it may be competitive.

The SCIFI sheets are made from plastic fibres of diameter 1 mm and length 6 m. This will provide a position measurement accuracy σ ~ 300 μm. We assume the bulk cost of a single image intensifier/CCD readout channel to be 25 KSF and (as for UA2) 2000 fibres to be handled by a single channel. These fibres cover an area of $2000 \times 6 \times 10^{-3} = 12$ m^2. So the total cost of a SCIFI muon chamber, including mechanical costs is ~ (25 + 5) KSF/12 ~ 2.5 KSF m^{-2}. This is identical to the typical cost of large area drift chambers. The particular advantages of the SCIFI chambers are speed, compactness and the ability to be wrapped in circles to match optimally the field direction in the forward toroids. The triggering capability of this system will be discussed in the next section.

10. READOUT AT THE SUPERCOLLIDER

10.1 Image intensifier/CCD systems

The high speed operation of an image intensifier/CCD system is paced by the CCD. The maximum rate at which a CCD may be exposed is several $\times 10^5$ Hz. This is set by the fast clear time of 1 μs which would, for example, lead to a 50% dead time at an exposure rate of 10^6 Hz. The readout times are typically 10 ms, reducing to 1 ms for

the highest speed contemporary CCDs. With these slow readout times (which are due to the high degree of multiplexing) it is clear that detailed CCD information cannot participate in the trigger until level 3 ($\lesssim 10^3$ Hz) where the events are analysed in parallel microprocessors. It is possible, however, to obtain fast OR'd SCIFI pulses which can participate in level 2 triggers ($\lesssim 10^5$ Hz). These pulses are generated at the anodes of the final image intensifier stages and correspond to the sums of the total SCIFI pulse height in regions of area ~ 1 cm^2.

The operation of an image intensifier/CCD system at low rates $\lesssim 10^6$ Hz is illustrated in Fig. 49. Here the decision time for a level 1 trigger is less than mean time between events. In these cases the phosphor decay time of the DC first stages can be suitably chosen to store the event at the input of the gated MCP stage while the trigger decision is taking place (Fig. 49b). The gate is opened by a successful level 1 trigger and the CCD is exposed. Data is then read out of the CCD. The readout is aborted and the CCD is fast cleared if the level 2 trigger is satisfied.

At higher rates it is necessary to provide an optical delay line upstream of the gated image intensifier stage (Fig. 50). The first two stages are proximity focussed photodiodes mounted directly at the edge of the SCIFI detector. Since these devices do not have a MCP they have a high quantum efficiency and operate in longitudinal magnetic fields of any strength. The photodiodes serve to amplify the optical signal by a factor of 100 and to shift the light to a longer wavelength for improved optical transmission. The fastest available phosphors are used (P47, τ = 35 ns). The output is connected to a flexible coherent fibre bundle which acts as the optical delay line. The length of this delay line must be sufficient to allow the level one trigger to open the gate of the final stage before the arrival of the optical data, e.g. a level 1 decision time of 350 ns would require a 60 m delay line. This situation is shown in Fig. 51 for a period of 50 ns between crossings, which corresponds to the minimum system integration time. In order to preserve the lifetime of the final stage image intensifier, the device and CCD may be cooled and the gain reduced. (Suitably cooled, CCD's can record and shift signals of < 10 electrons.)

The ability of a SCIFI micro-tracker to handle the high rates of the supercollider (Table 6) is due to its extremely high granularity: the full system comprises ~ 5×10^7 fibres or ~ 10^7 'cells' (defined by the 50 μm image intensifier spot size). During an integration time of 50 ns approximately five events will occur, with a total multiplicity of 100 (high p_T event) + 4×40 (minimum bias events) = 260 charged particles. However, the resulting occupancies are low. For example, in the innermost layer at r = 10 cm there are $2\pi 10/(50 \times 10^{-4}) = 1.3 \times 10^4$ cells, and so the occupancy per trigger is $260/1.3 \times 10^4 = 2.1\%$.

It would clearly be an advantage to build a device which replaced the coherent fibre optic delay line. Figure 52 shows some conceptual schemes which involve a) vacuum and b) gas-filled devices. The vacuum device is basically a proximity focussed image intensifier with a long drift space in a small electric field (10 cm with ΔV_{drift} = 11 V provides a 100 ns delay). A strong longitudinal magnetic field provides focussing. The gas filled device requires a photocathode which is compatible with exposure to gases. A candidate is TMAE, the photosensitive component used in RICH detectors. Here we require photons to be absorbed immediately after traversing the input fibre optic window. This may be achieved by heating or pressurizing the TMAE

or, perhaps preferably, by arranging for a liquid TMAE photocathode at the inner face of the input window. Since TMAE is only sensitive to photons with wavelength $\lambda < 220$ nm, it will be necessary to precede this device with a converter stage involving a suitable (BaF_2?) phosphor and quartz fibre optics. Finally, after drifting the appropriate distance it should be possible to achieve some electronic gain by avalanche multiplication at a suitably-designed phosphor surface.

10.2 Phototubes and Si photodiodes

Single or multi-anode phototubes and Si photodiodes can read out both SCIFI tracking detectors with moderate diameter (~ 1 mm) fibres and SCIFI calorimeters. Phototubes (which have been described in Section 5.1) have the merits of robustness, low noise, high gain and high rate capabilities, but cannot be used in magnetic fields.

Probably the best devices to read out a supercollider SCIFI calorimeter are Si photodiodes. The simplest construction involves 'fluorescent flux concentrators'[54]: small waveshifter plates of dimensions ~ 30 x 30 x 1 mm^3 which have a Si photodiode glued to each of two opposite narrow faces. The dimensions of the plates are chosen according to the desired calorimeter cell size, e.g. here we chose $\Delta\phi \times \Delta\eta \simeq 0.03 \times 0.03$ for the electromagnetic calorimeter. A mosaic of these plates covers the outer surface of each longitudinal section of the calorimeter. This readout is very compact and provides a simple and effective technique for longitudinal readout, with a flexible choice of cell sizes and shapes. Two photodiodes ensure the identification and rejection of spurious pulse height due to tracks which cross a Si wafer.

The light output can be estimated from the present measurements of ~ 10,000 pe GeV^{-1} in a Pb/SCIFI block with a 1/1 volume ratio and bialkali phototube readout. We will assume a Pb/SCIFI ratio of 3/1, a photon collection efficiency in the waveshifter plate of 0.2 and a relative quantum efficiency (Si/phototube) = 2. The expected yield is then 10,000 x 1/3 x 0.2 x 2 = 1300 pe GeV^{-1}, or a noise equivalent per photodiode of ~ 1 GeV. With a little improvement this is probably acceptable for supercollider operation. The advantages of Si photodiode readout are well-known; the absence of drift (no gain), compactness and compatibility with magnetic fields are of particular note. Finally we remark that it should be possible to calibrate each calorimeter cell to < 1% simply from the singles pulse height distribution. Each 3 x 3 cm^2 cell at 1 m radius receives 10^5 Hz charged particles. This constitutes a constant energy source which can be used to inter-calibrate all cells and to monitor drifts with high statistical accuracy. It should be straightforward to follow the slow degradation of light output of a SCIFI calorimeter, which does not have short time scale problems associated with gas and liquid impurities.

11. CONCLUSIONS

SCIFI detectors have advanced rapidly since their recent 'rediscovery' to the stage where they are now being incorporated in a few pioneer experiments. Current work has demonstrated their striking capacity for electronic 'imaging' which leads to a broad variety of unique applications in tracking and calorimetry. With some further development it appears that SCIFI detectors are well-matched to the harsh experimental environment of the supercollider. Moreover, the use of SCIFI in tomorrow's supercollider detectors can simultaneously reduce their size and cost while substantially improving the performance.

Acknowledgements

I would like to thank many colleagues for discussions, in particular, M. Bourdinaud, J.P. Fabre, J.M. Gaillard, C.G.A. Hill, H. Leutz, L. Linssen, S. Majewski, R. Mead, R. Ruchti, H. Schönbacher, J.C. Thévenin and my colleagues in the CERN-MPI(Munich)-RAL Collaboration. I also wish to to thank A. Zichichi and the Directors of this Workshop, G. Charpak and F. Villa, for having organized such an enjoyable and stimulating meeting. Finally, my thanks to S. McCreadie for typing this paper so efficiently.

REFERENCES

1. See, for example, the review by G.T. Reynolds, IRE Trans. Nucl. Sci. NS-7, 115 (1960).
D.A. Hill et al., Proc. 2nd Symp. on Photo-Electronic Devices, London (1961) 475.
H.C. Burrows et al., Nuclear Electronics I, (1962) 153.
D.G. Anderson et al., British Scientific Instrument Research Association (SIRA) AERE/EMB/PR1301 (1961); Proc. 6th Int. Congress on Glass (1962) 429. (The latter work resulted in the development of GS1 scintillating glass.)

2. S.R. Borenstein et al., Proc. 1981 Isabelle Summer Study (1981) 1438; Phys. Scripta 23, 550 (1981); IEEE Trans. Nucl. Sci. NS-29, 402 (1982); IEEE Trans. Nucl. Sci. NS-31, 396 (1984).

3. L.R. Allemand et al., Nucl. Instrum. Methods 225, 522 (1984).
H. Blumenfeld et al., IEEE/NS-33, No. 1, 54 (1986).

4. D.R. Potter, IEEE/NS-29, No. 1 (1982).

5. R. Ruchti et al., IEEE Trans. Nucl. Sci. NS-30, No. 1, 40 (1983); IEEE/NS-31, No. 1, 69 (1984); IEEE/NS-32, No. 1, 590 (1985); IEEE/NS-33, No. 1, 151 (1986).

6. J.M. Gaillard et al. (UA2 Collaboration), Proc. DPF Conf., Eugene, Oregon (1985) 912.

7. W.R. Binns et al., Nucl. Instrum. Methods A251, 402 (1986).

8. A. Konaka et al., Proc. 23rd Int. Conf. on High-Energy Physics, Berkeley (1986).

9. A. Bross, Nucl. Instrum. Methods 247, 319 (1986).

10. M. Atkinson et al., Nucl. Instrum. Methods A254, 500 (1987). The results using CCD readout are presented in a paper which will presently be submitted to Nuclear Instruments and Methods.

11. D.R. Potter, Proc. Workshop on New Solid State Devices for High-Energy Physics, Lawrence Berkeley Laboratory (1985).

12. H. Blumenfeld et al., Nucl. Instrum. Methods 225, 518 (1984); 235, 326 (1985).

13. H. Burmeister et al., Nucl. Instrum. Methods 225, 530 (1984).

14. DELPHI Technical Proposal, CERN/LEPC/83-3, 159 (1983).

15. J. Fent et al., Nucl. Instrum. Methods 211, 315 (1983).
H. Fessler et al., Nucl. Instrum. Methods 228, 303 (1985);
Nucl. Instrum. Methods A240, 284 (1985).

16. M. Albrow et al. (UA1 Collaboration), CERN-EP/86-131 (1986), submitted to Nuclear Instruments and Methods.

17. L. Bachman et al., Nucl. Instrum. Methods 206, 85 (1983).

18. R. Ruchti et al., Proc. 1982 DPF Summer Study on Elementary Particle Physics and Future Facilities, Snowmass, Colorado (1982) 373.
M. Atkinson et al., Nucl. Instrum. Methods 225, 1 (1984).

19. I.M. Chiang et al., AGS Proposal E787 (1986).

20. K. Pretzl, private communication.

21. D. Binnie et al., Proc. 1984 Summer Study on the Design and Utilization of the Superconducting Super Collider, Snowmass, Colorado (1984) 593.
M. Atkinson et al., Nucl. Instrum. Methods 237 (1985) 505.
J. Kirkby, Proc. 5th Topical Workshop on Proton-Antiproton Collider Physics, St. Vincent, Aosta Valley (1985) 672.

22. P. Sonderegger, CERN-EP/86-214 (1986), submitted to Nuclear Instruments and Methods.

23. J.B. Birks, Theory and practice of scintillation counting, Pergamon Press, Oxford (1964).

24. I.B. Berlman, Handbook of fluorescence spectra of aromatic molecules, Academic Press, New York and London (1971).

25. Nuclear Enterprises Ltd., Bath Road, Beenham, Reading, Berkshire, England.

26. Bicron Corporation, 12345 Kinsman Road, Newbury, Ohio 44065, USA.

27. C. Aurouet et al., Nucl. Instrum. Methods 169, 57 (1980).

28. M. Bourdinaud and J.C. Thévenin, Physica Scripta, Vol. 23, 534 (1981).

29. J.C. Thévenin et al., Nucl. Instrum. Methods 169, 53 (1980).

30. P.L. Mattern et al., IEEE Trans. Nucl. Sci. NS-21, 81 (1974);
NS-22, 2468 (1975).

31. H. Schönbacher and W. Witzeling, Nucl. Instrum. and Methods 165, 517 (1979).

32. Y. Sirois and R. Wigmans, Nucl. Instrum. Methods A240, 262 (1985).

33. G. Marini et al., CERN/85-08 (Yellow Report, 1985).

34. J.P. de Brion et al., Saclay preprint DPhPE 86-07 (1986).

35. J.C. Thévenin, private communication.

36. C.L. Renschler and L.A. Harrah, Nucl. Instrum. Methods A235, 41 (1985).

37. S. Majewski, University of Florida, Gainesville, private communication.

38. W.R. Binns and A. Bross, Workshop on New Solid State Devices for High-Energy Physics, Lawrence Berkeley Laboratory (1985).

39. A.R. Spowart, Nucl. Instrum. Methods 135, 441 (1976); 140, 19 (1977); 150, 159 (1978).

40. Levy Hill Laboratories Ltd. (C.G.A. Hill, Director), 5 Sheffield House, Fieldings Road, Cheshunt, Waltham, Hertfordshire EN8 9TJ, England.

41. Collimated Holes Inc. (R.W. Mead, President), 460 Division Street, Campbell, California 95008, USA.

42. Optical characteristics of cathode ray tube screens, Electronic Industries Association, 2001 Eye Street N.W., Washington, DC 2006, USA. TEPAC Publication No. 116 (revision of JEDEC publication No. 16-C) (1980).

43. Hamamatsu Photonics K.K., 1126 Ichino-cho, Hamamatsu City, Japan.

44. Philips International BV, Elcoma Division, PO Box 218, 5600 MD Eindhoven, The Netherlands.

45. R. Meunier, CERN, private communication.

46. Delft Electronische Producten, Postbus 60, 9300 AB Roden, The Netherlands.

47. Thomson-CSF, Division Tubes Electroniques, 38 rue Vauthier, BP 305, 92102 Boulogne-Billancourt Cedex, France.

48. S. Reynaud, CERN/EF/INSTR 86-1 (1986).

49. Proxitronic, Robert Bosch Strasse 34, D-6140 Bensheim, Fed. Rep. Germany.

50. Fibre Optics Development Systems Inc., 427 Olive Street, Santa Barbara, California 93101, USA.

51. Report of the Task Force on Detector R & D for the Superconducting Super Collider, SSC-SR-1021 (1986).

52. A. Seiden, these proceedings.

53. R. Wigmans, CERN/EF/86-18 (1986), submitted to Nuclear Instruments and Methods.

54. E. Lorenz et al., Nucl. Instrum. Methods A249, 235 (1986).

a) SOLID SCINTILLATOR

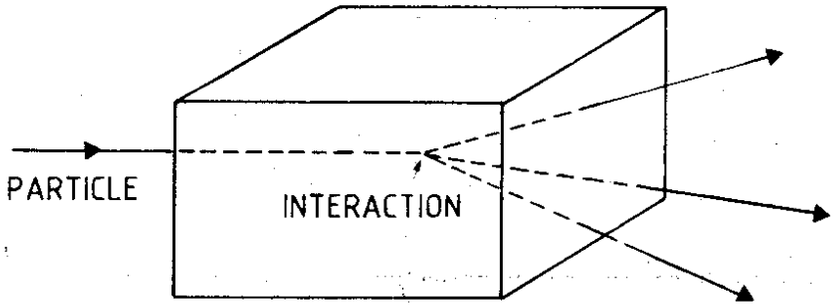

b) SCINTILLATING FIBRE BUNDLE (FIBRES PERPENDICULAR TO TRACK)

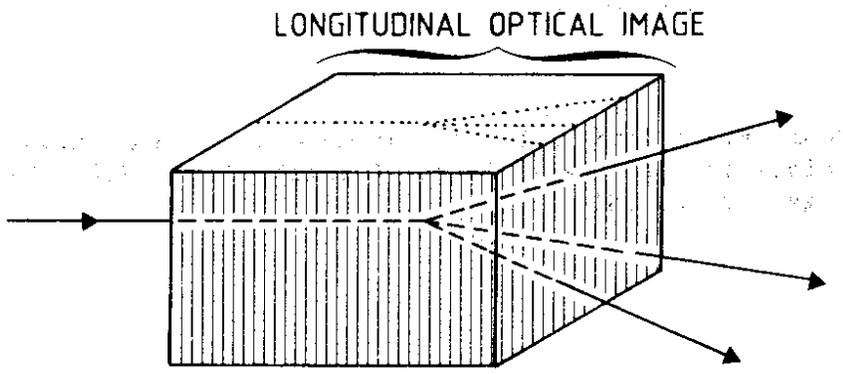

c) SCINTILLATING FIBRE BUNDLE (FIBRES PARALLEL TO TRACK)

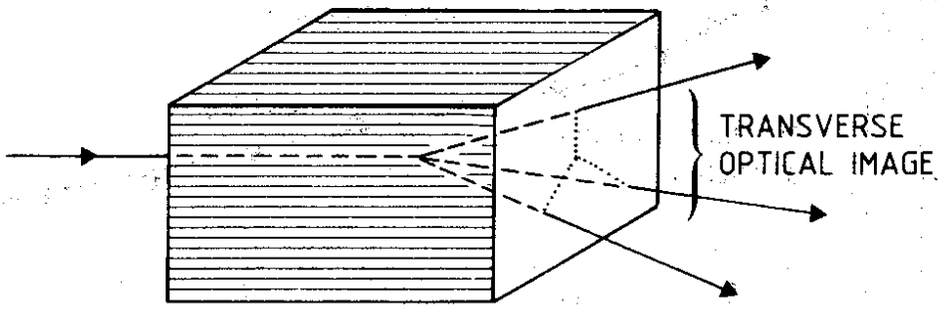

Fig. 1. Principle of the scintillating fibre (SCIFI) target. The solid scintillator a) is replaced by scintillating fibre bundles which transport either a longitudinal b) or transverse c) optical image of the interaction to an output face.

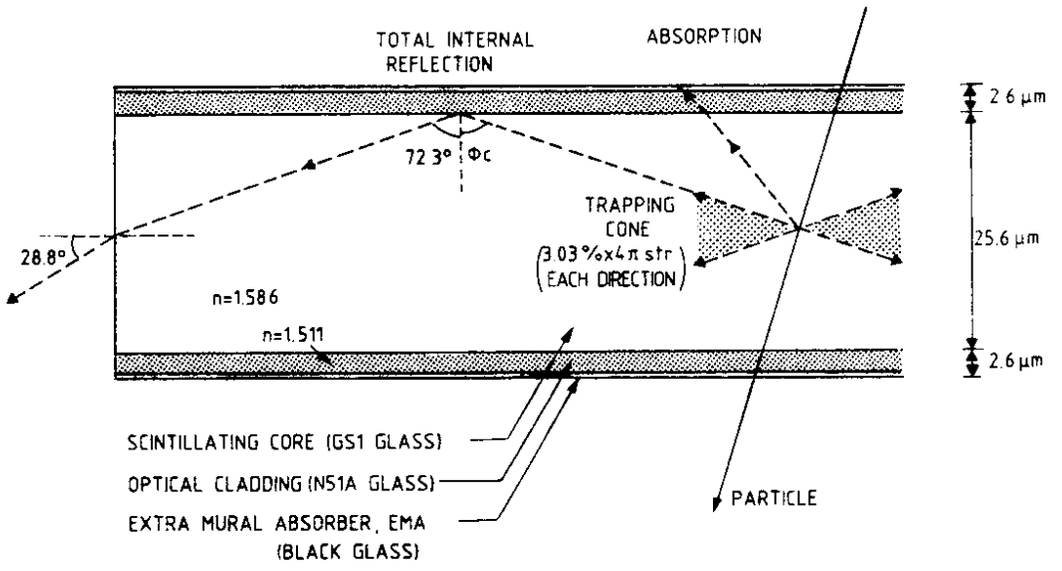

Fig. 2. Geometrical and optical parameters of an individual scintillating glass fibre (target 2 in Ref. 10 and Figs. 17 and 18).

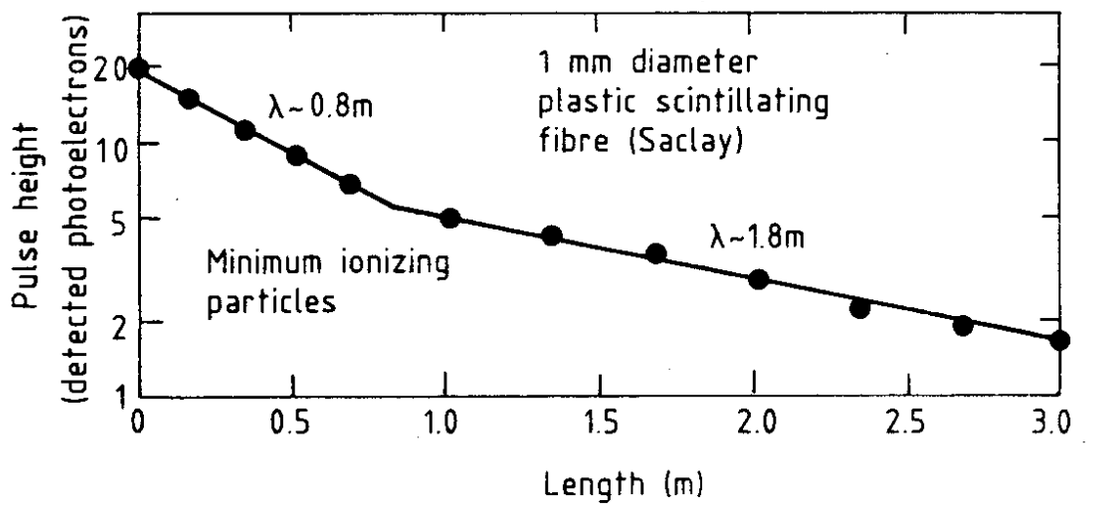

Fig. 3. Pulse height vs. length observed in plastic SCIFI using a bialkali phototube (Ref. 3).

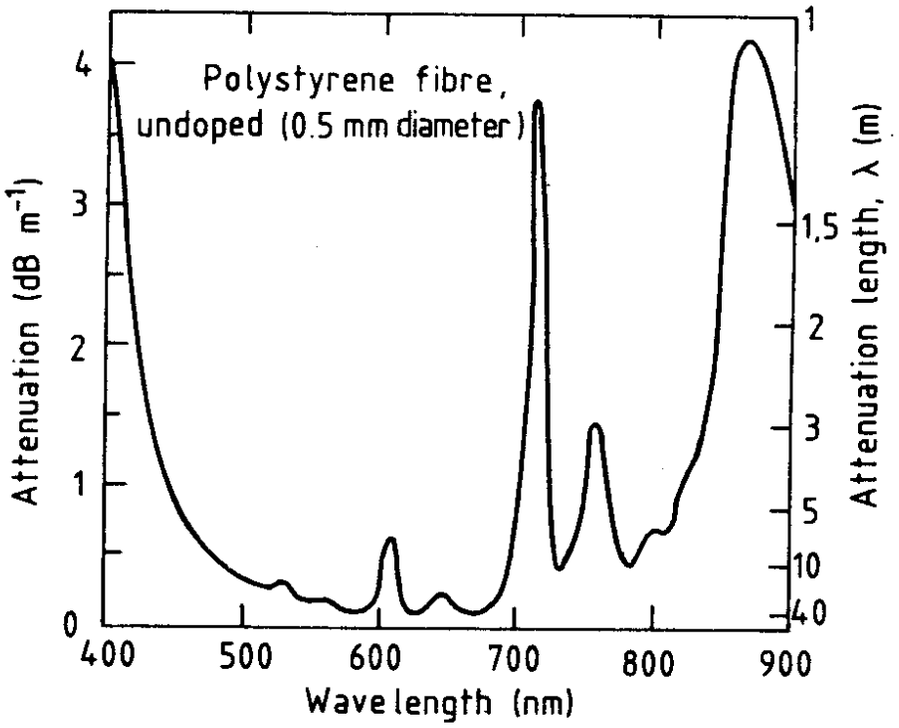

Fig. 4. Attenuation in undoped polystyrene fibres vs. wavelength (Ref. 3).

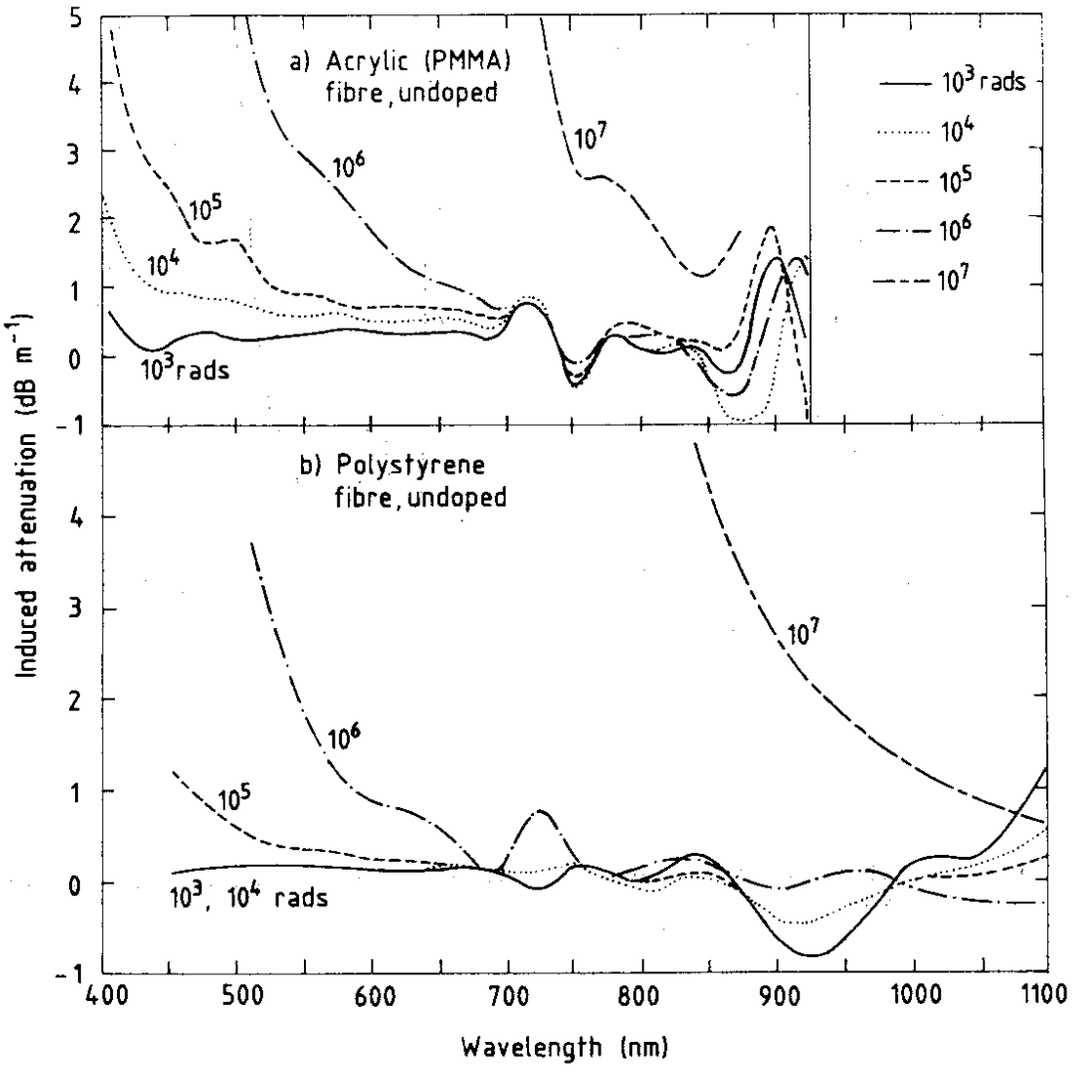

Fig. 5. Radiation-induced attenuation in a) undoped acrylic and b) undoped polystyrene fibres (Ref. 30). The curves show the changes in attenuation relative to the zero radiation values.

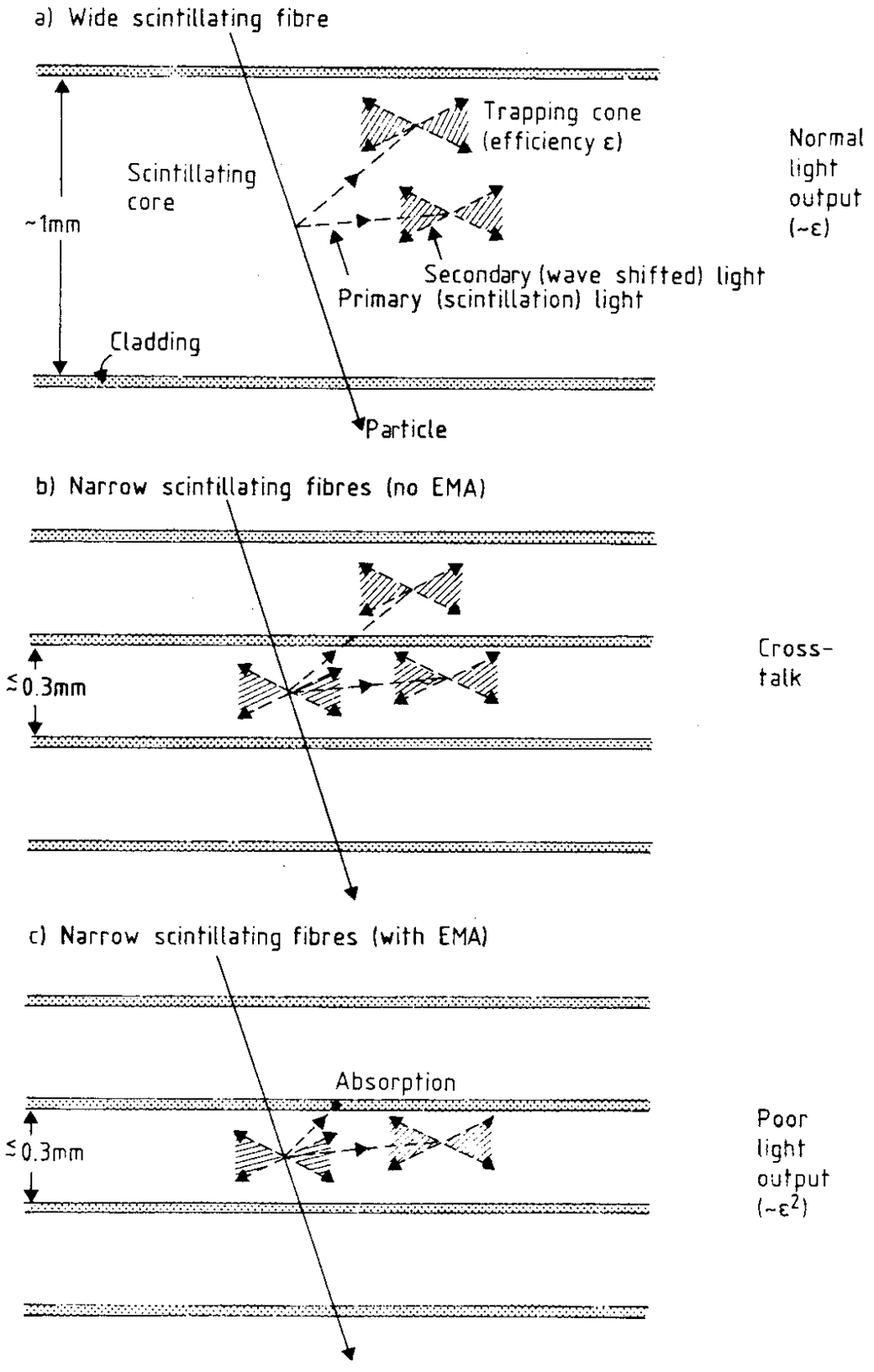

Fig. 6. Schematic representation of the operation of plastic SCIFI with a) wide and b), c) narrow diameters. The narrow diameter fibres function poorly due to either b) cross-talk or c) low efficiency.

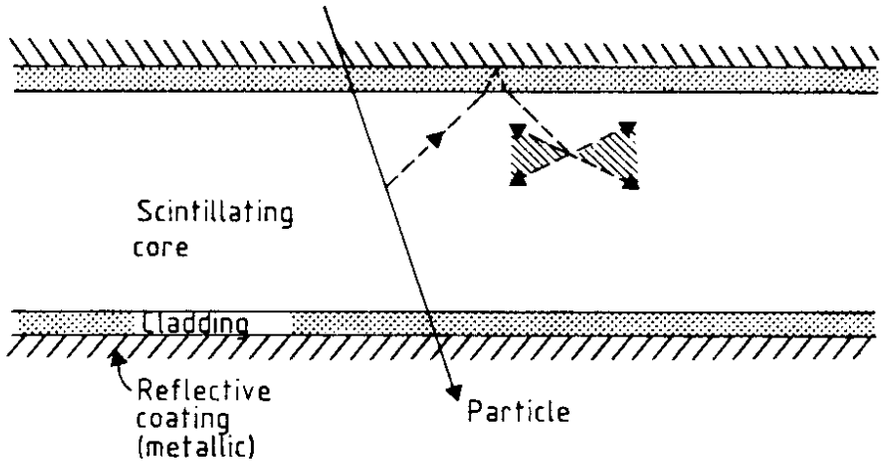

Fig. 7. Operation of narrow-diameter plastic SCIFI with an outer metallic reflective coating.

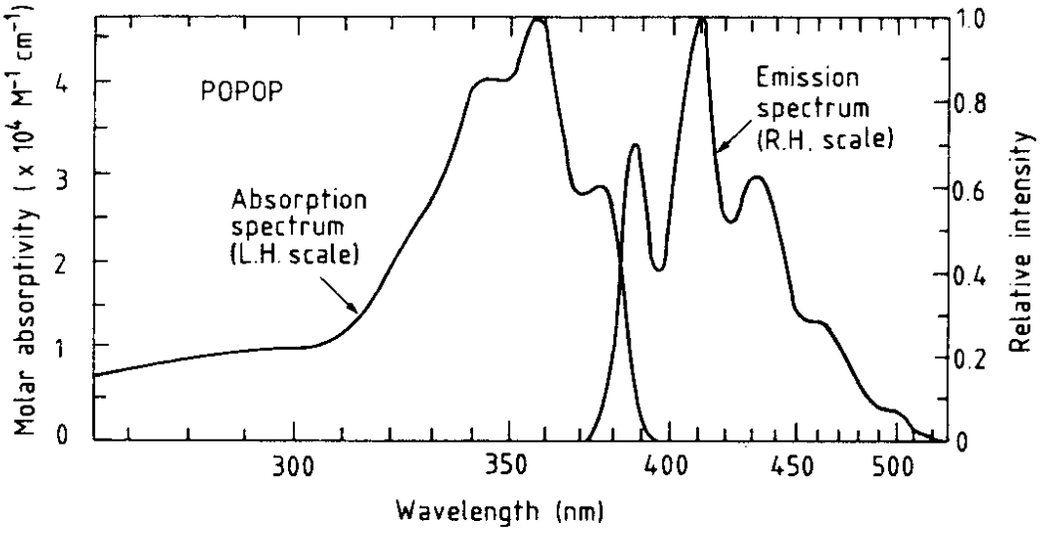

Fig. 8. Absorption and emission spectra of the aromatic waveshifter POPOP (Ref. 24).

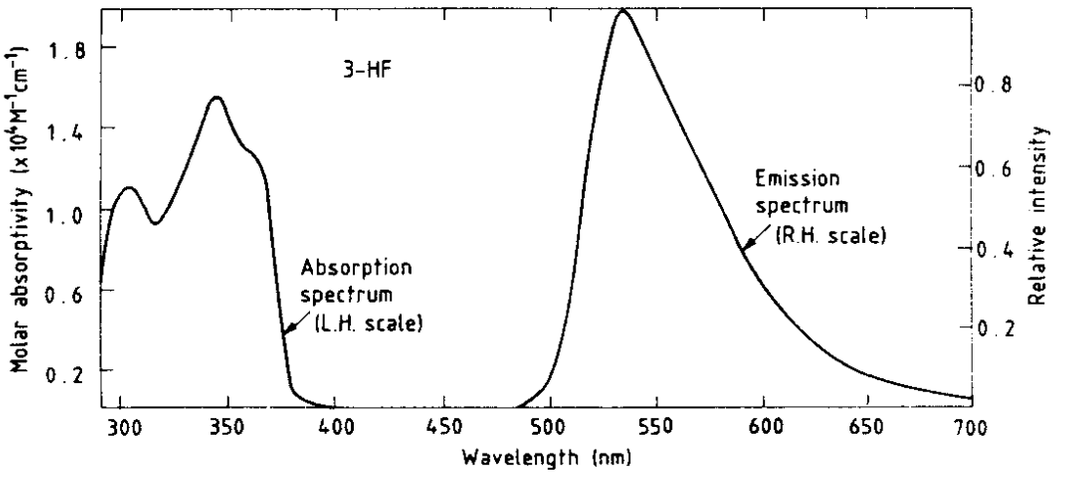

Fig. 9. Absorption and emission spectra of the aromatic waveshifter 3-hydroxyflavone, 3HF (Ref. 36).

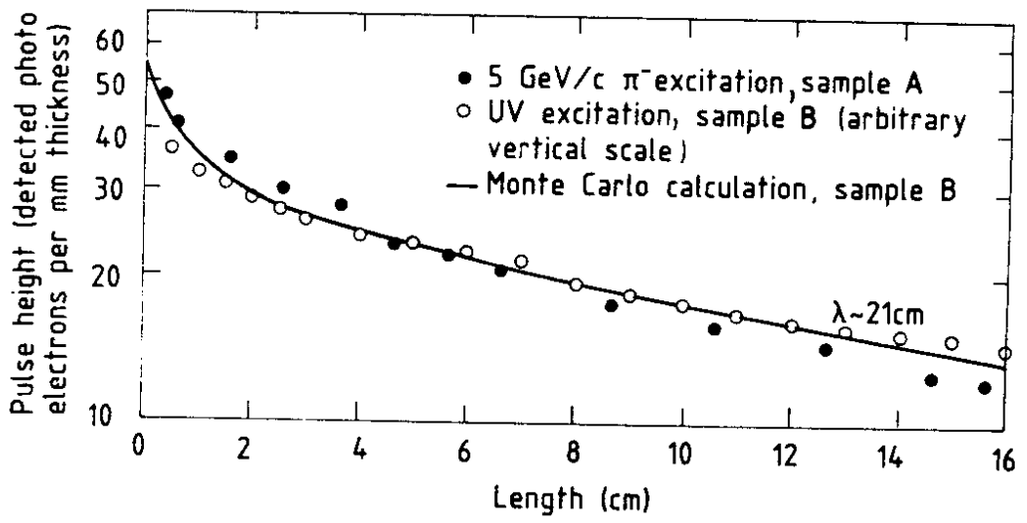

Fig. 10. Light yield, measured with a bialkali phototube, of polished GS1 scintillating glass blocks of length ~ 17 cm (Ref. 10). The curve is a Monte Carlo calculation of sample B based on measurements of the scintillation emission spectrum (Fig. 11) and transmission curve (Fig. 12). The vertical scale shows the observed photoelectron yield for sample A (for which the calculated photon efficiency is 28%).

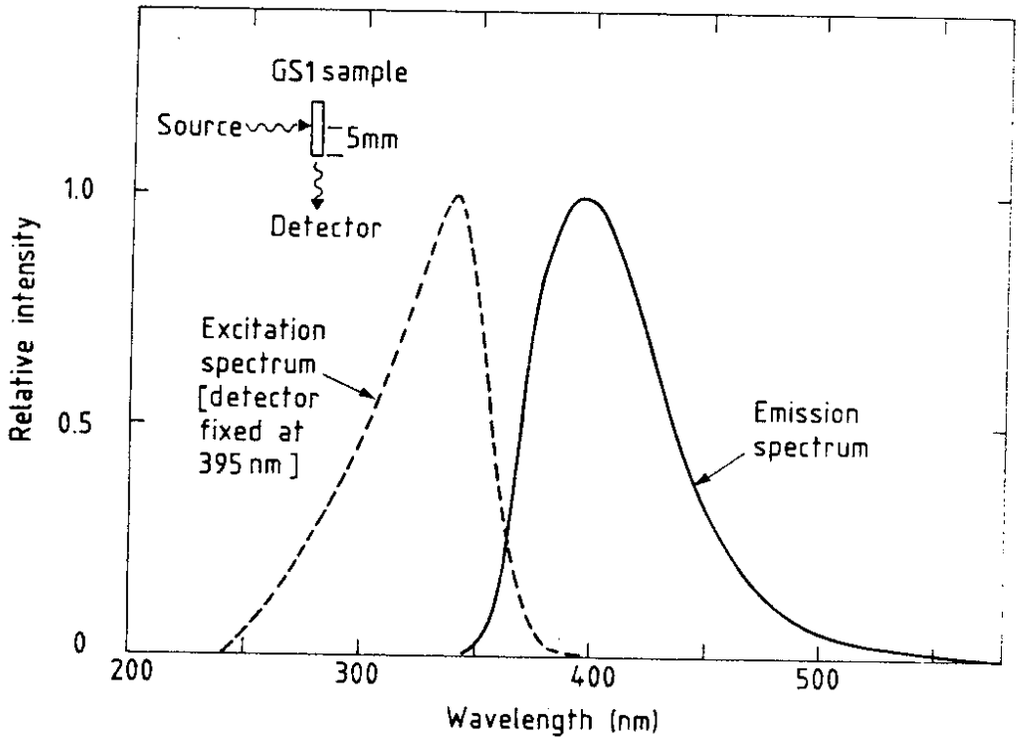

Fig. 11. Excitation and emission spectra of GS1 scintillating glass (Ref. 10). The excitation curve shows the relative emission intensity (with the detector fixed at 395 nm) when GS1 is excited by a UV source at the indicated wavelength and with a fixed intensity.

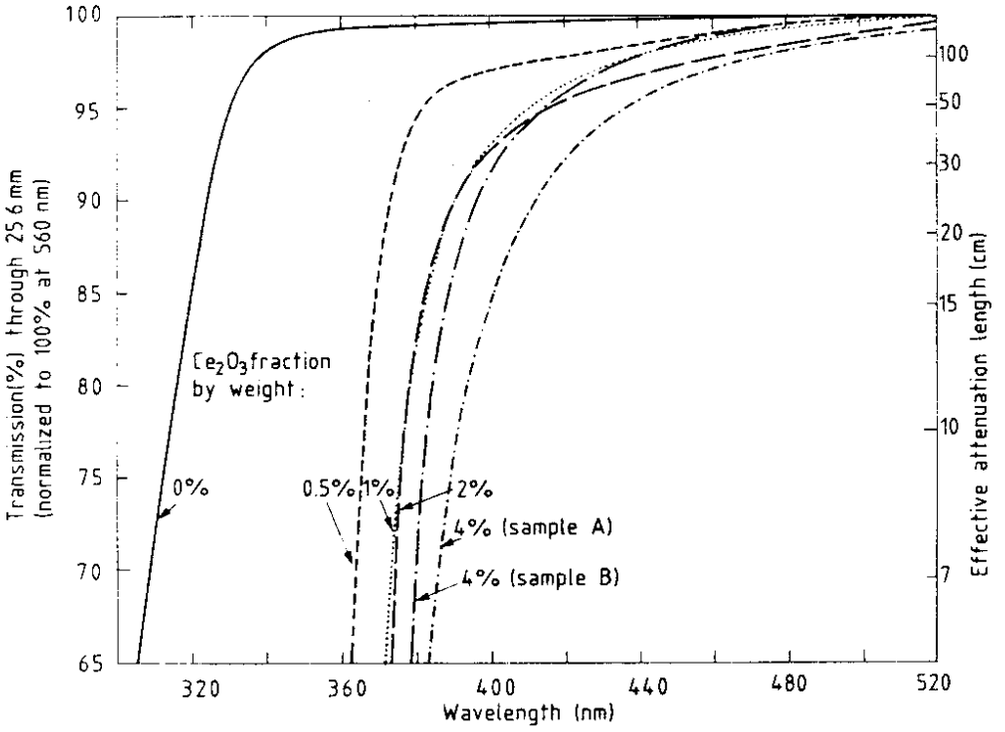

Fig. 12. Transmission vs. wavelength for samples of GS1 scintillating glass involving different fractions of Ce_2O_3 (Ref. 10). Two different samples (A and B) of nominal GS1 (4% Ce_2O_3) are displayed. The curves are normalized to 100% transmission at 560 nm. The measured transmissions at 560 nm range between 80–88%, corresponding largely to reflective losses at the entrance and exit faces and at scattering centres, such as small bubbles, inside the glass.

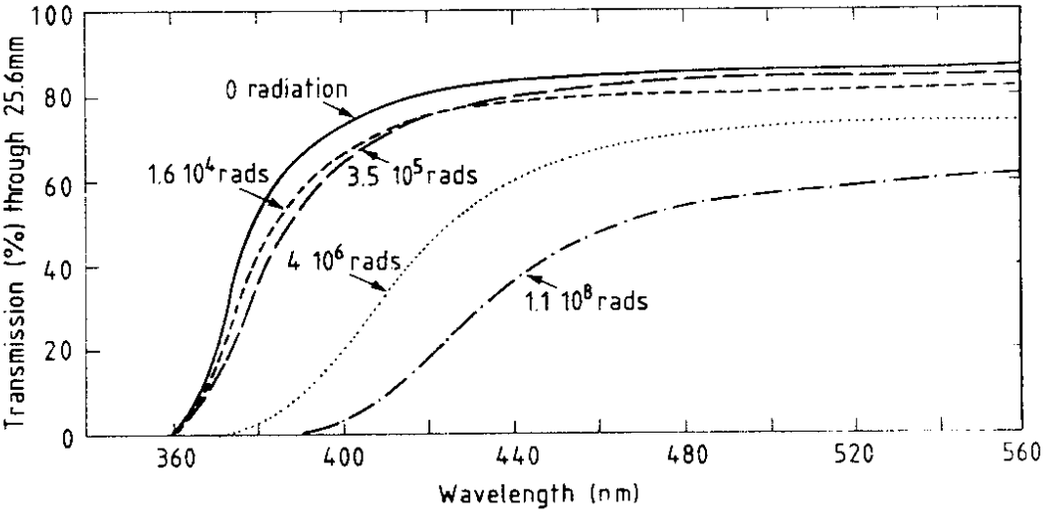

Fig. 13. Transmission vs. wavelength for samples of GS1 scintillating glass after exposure to secondary radiation from external targets at CERN (Ref. 10). The curves are not corrected for reflective losses.

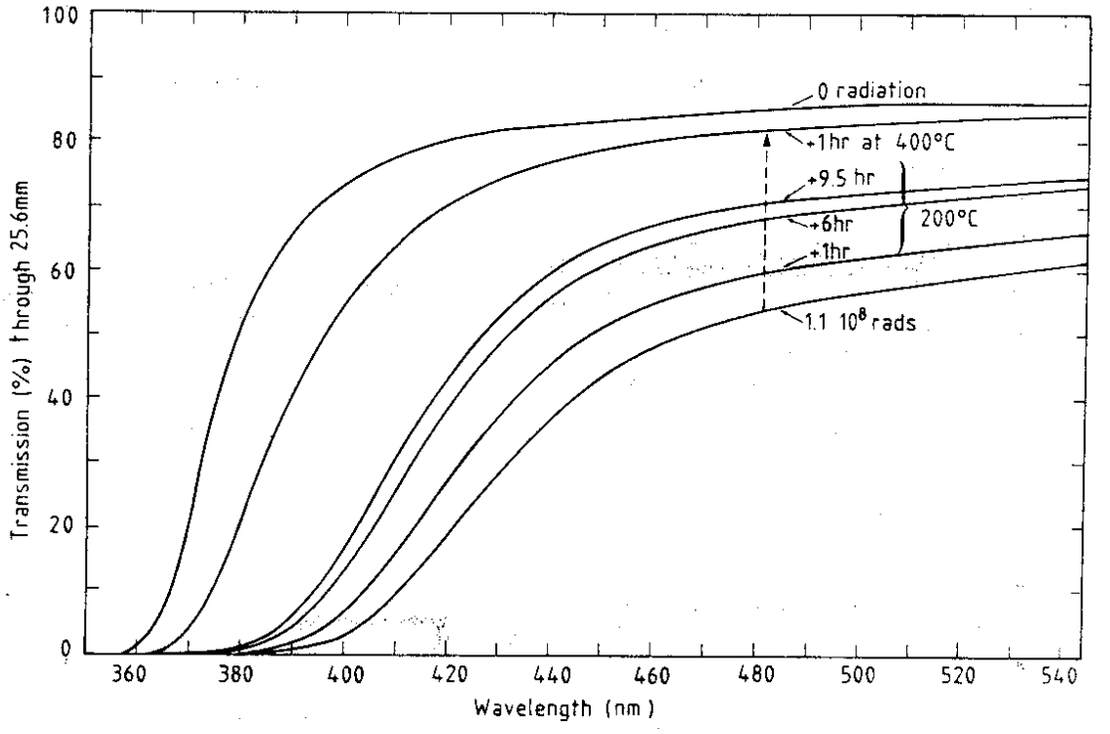

Fig. 14. Temperature annealing of a sample of GS1 scintillating glass after exposure to 1.1 x 10^8 rads (Ref. 10). The indicated annealing times are cumulative (e.g. the total annealing time at 200°C is 16.5 hours). The curves are not corrected for reflective losses.

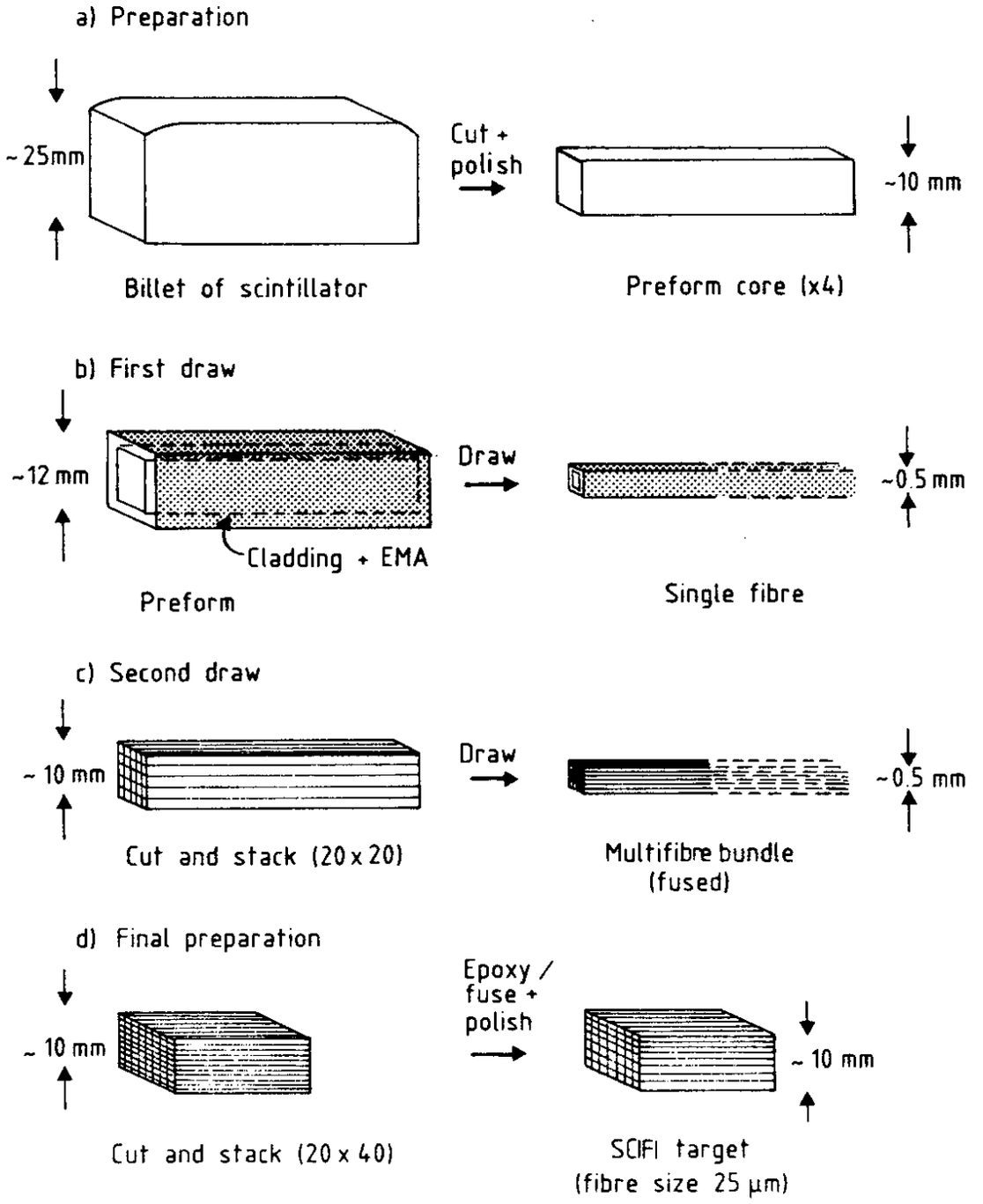

Fig. 15. Steps involved in the manufacture of coherent SCIFI bundles from bulk scintillator. The dimensions refer to the glass SCIFI targets of Ref. 10 and Figs. 17 and 18.

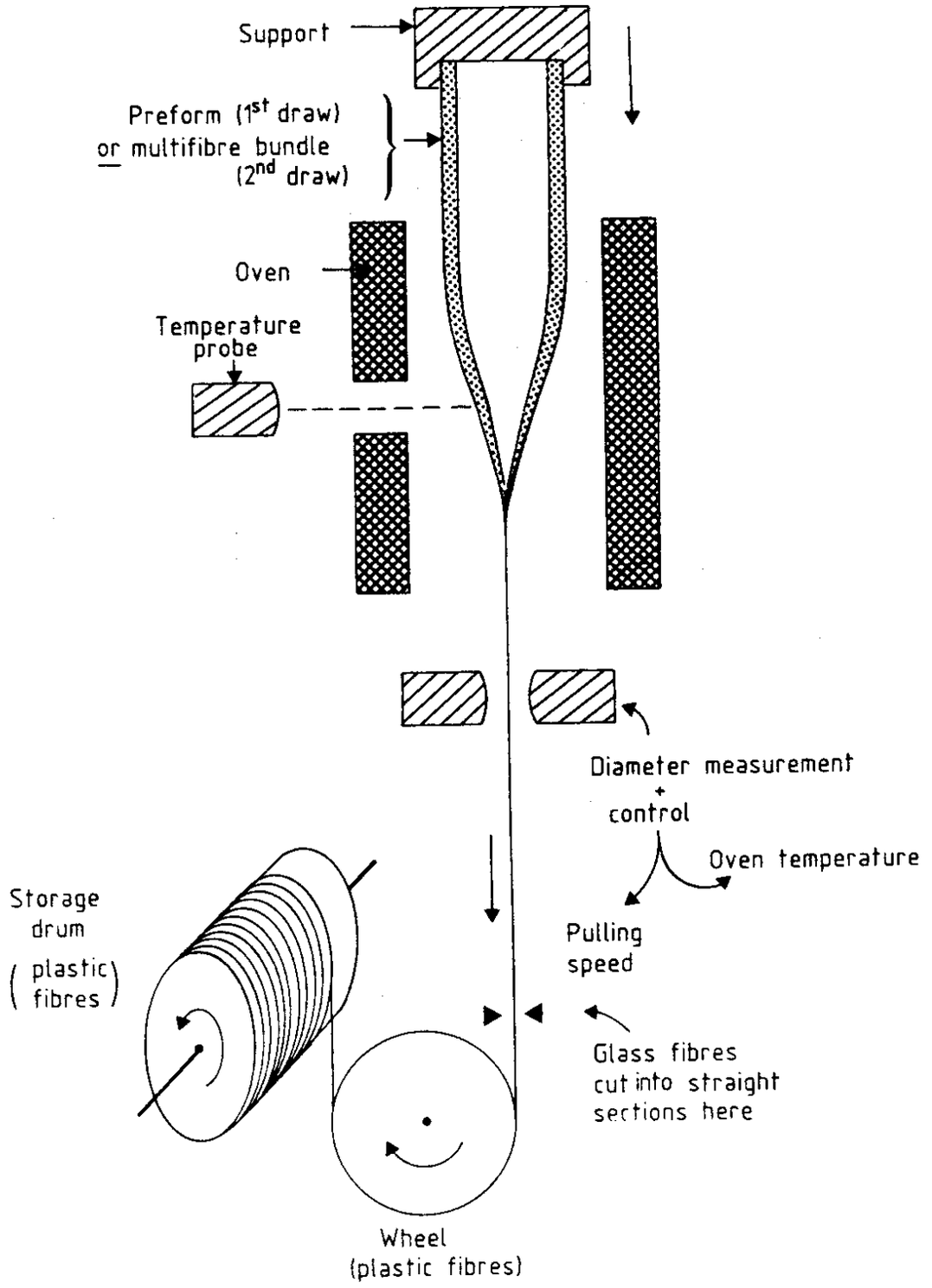

Fig. 16. Schematic representation of a fibre pulling station.

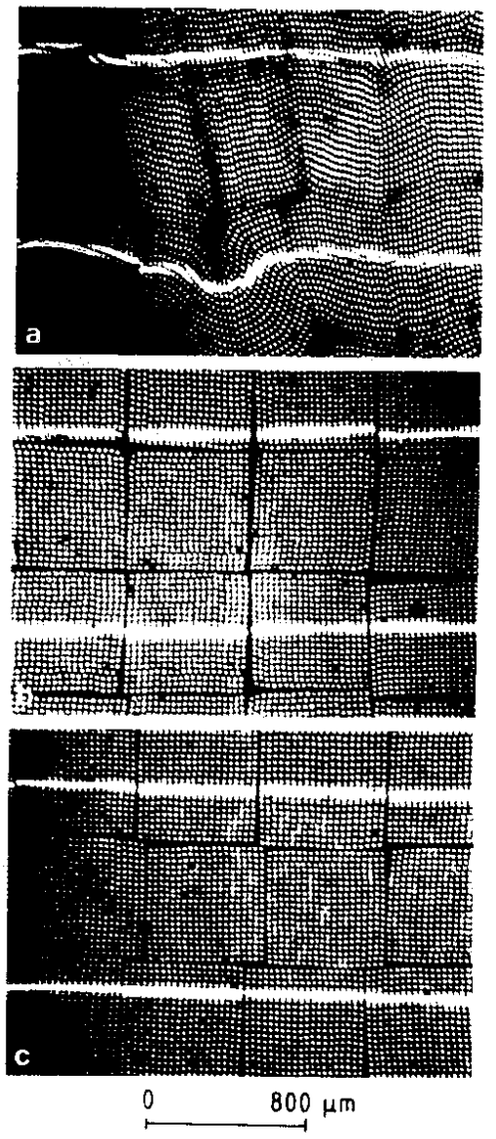

Fig. 17. Microphotographs of glass SCIFI targets (Ref. 10): a) target 1 (no EMA, fusion bonded multifibres), b) target 2 (EMA, epoxy bonded), and c) target 3 (no EMA, epoxy bonded). Photographs b) and c) show clearly the multifibre bundles, of transverse dimension 0.6 mm, which are composed of matrices of 20 x 20 individual fibres. The bright lines are the images of a pair of illuminated parallel straight slits of width 30 µm and separation 1 mm. The slits are placed in contact with the entrance face of each SCIFI target and viewed through 25 mm fibre length at the exit face.

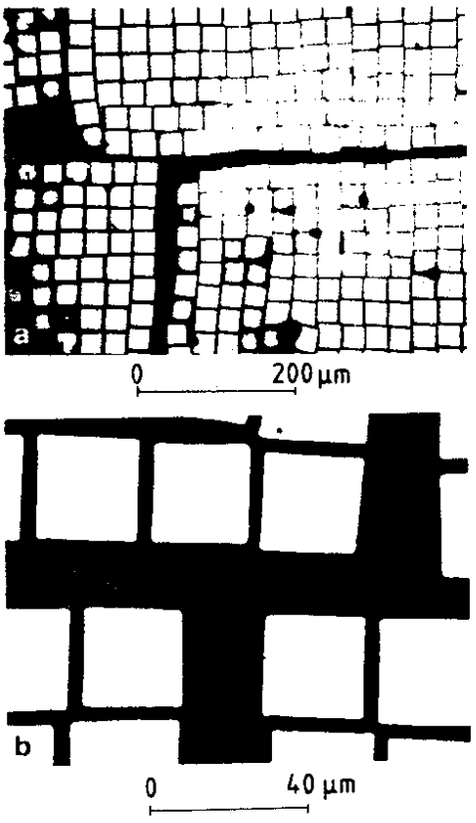

Fig. 18. High magnification views of individual glass fibres from target 2 (Ref. 10). The transverse dimension of a core (bright square) is 26 µm and the centre-to-centre spacing between fibres is typically 31 µm.

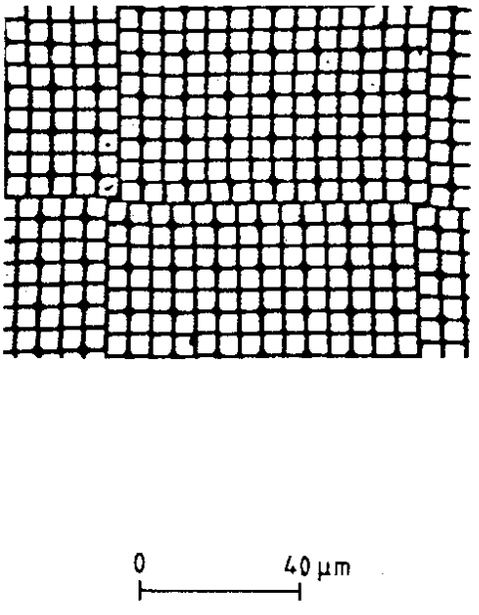

Fig. 19. Microphotograph of a fibre optic plate used in image intensifiers. The centre-to-centre fibre spacing is 5.5 µm.

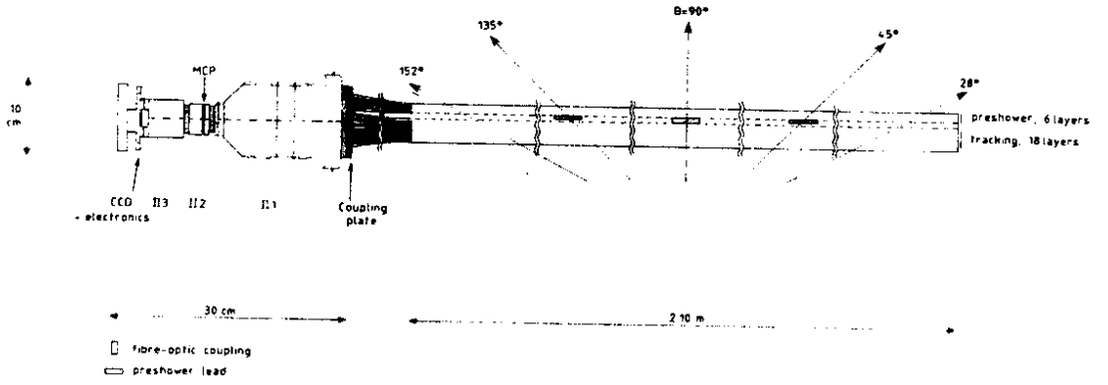

Fig. 20. Geometry and readout system of the UA2 plastic SCIFI detector, SFD (Ref. 6).

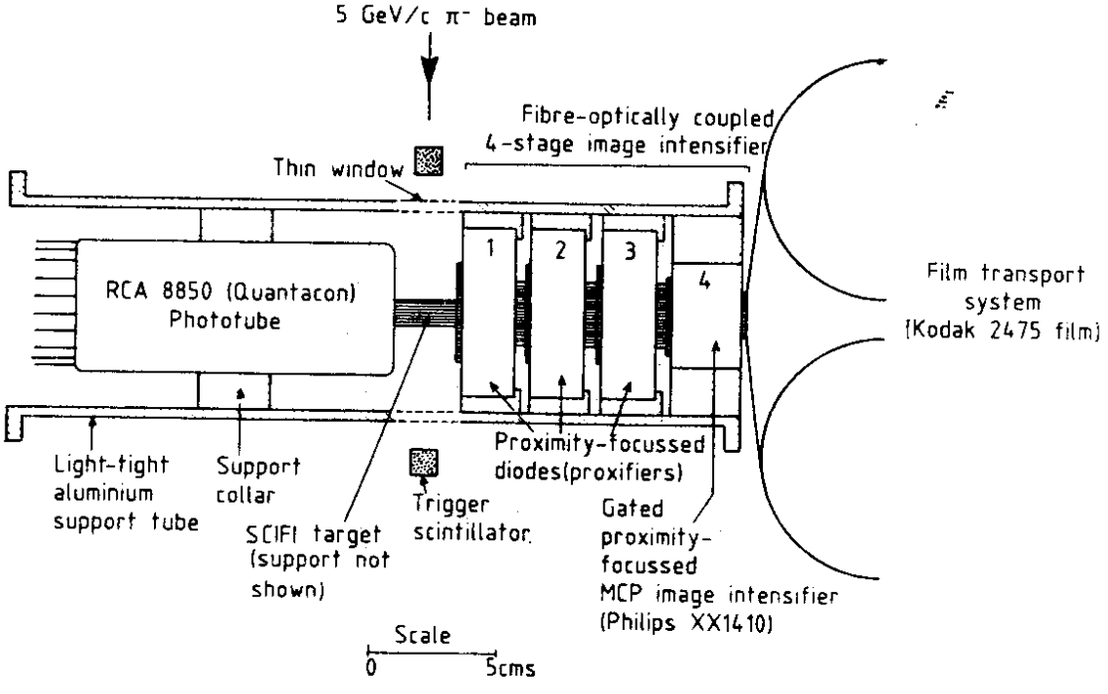

Fig. 21. Geometry and readout system of a glass SCIFI target (Ref. 10). The original film recording medium (as shown) is replaced by a CCD in later tests.

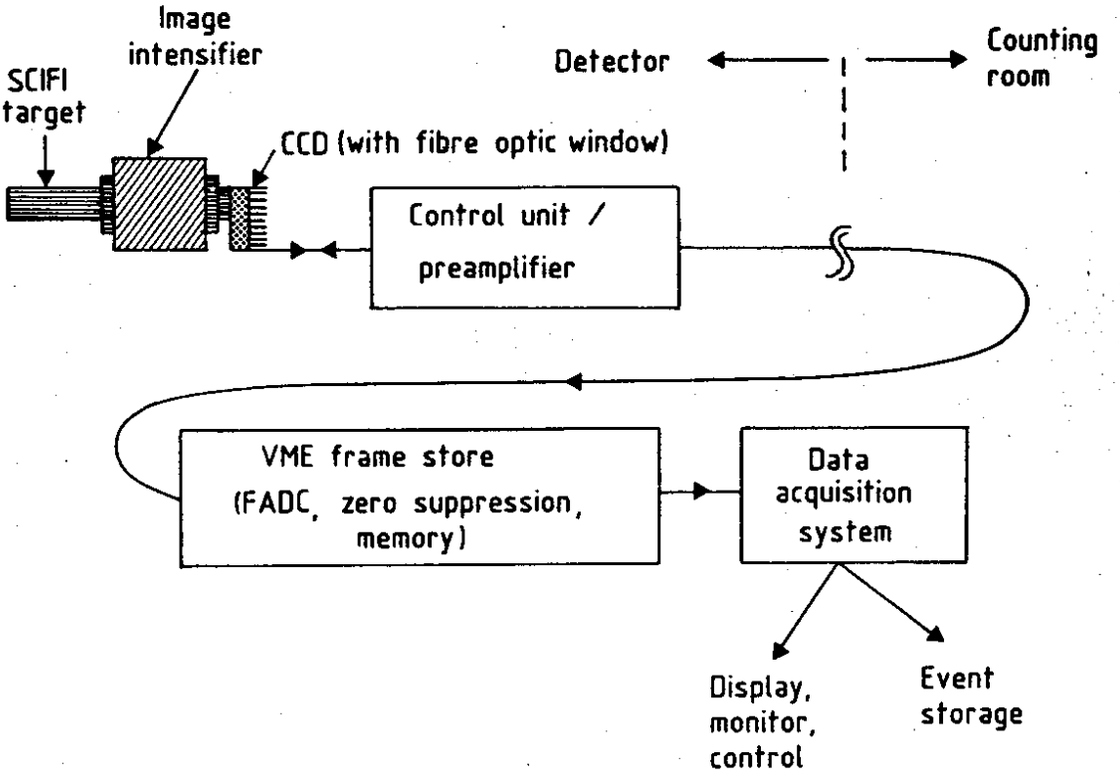

Fig. 22. CCD readout system.

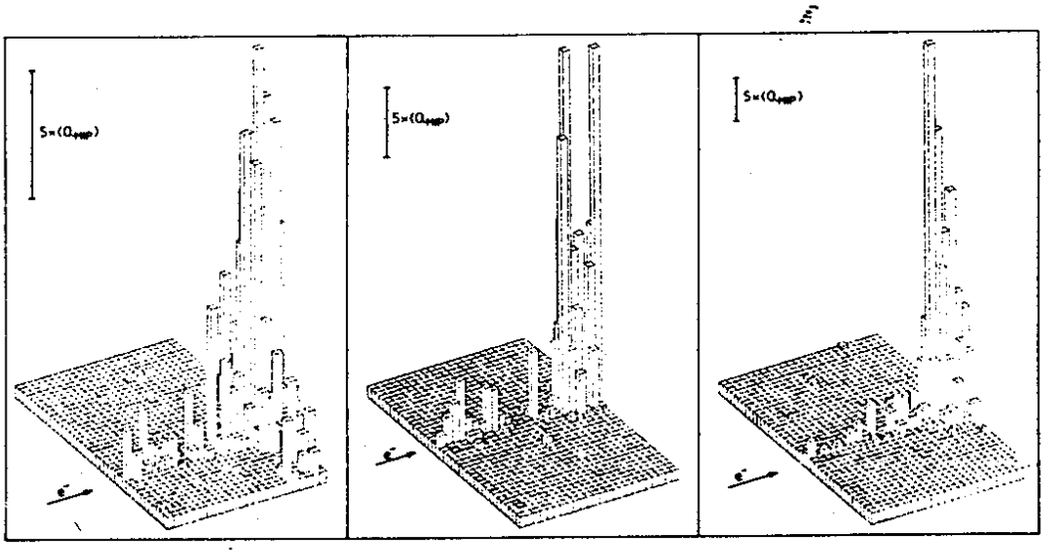

Fig. 23. Typical single events of 40 GeV/c electrons in the UA2 SFD prototype (Ref. 6). Each pixel represents 1 × 1 mm², equivalent to a single fibre. A 1.5 X_0 Pb converter (not represented) separates the first 18 ('tracking') and last 6 ('preconverter') fibre layers.

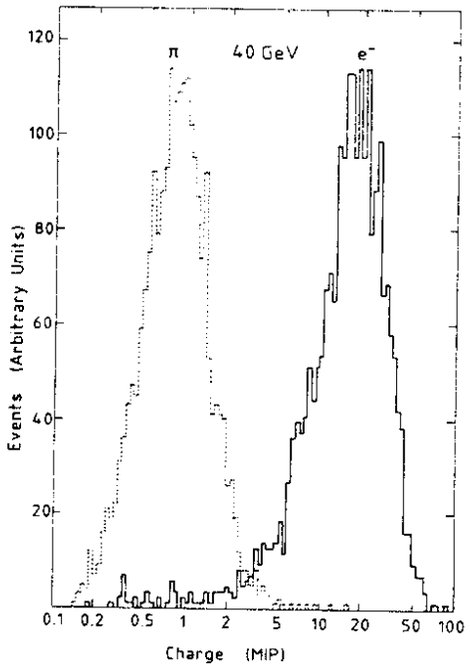

Fig. 24. The total pulse height in the 6 preconverter fibre layers of the SFD for 40 GeV π and 40 GeV e (Ref. 6). The electron data have a small π contamination of ~ 1%.

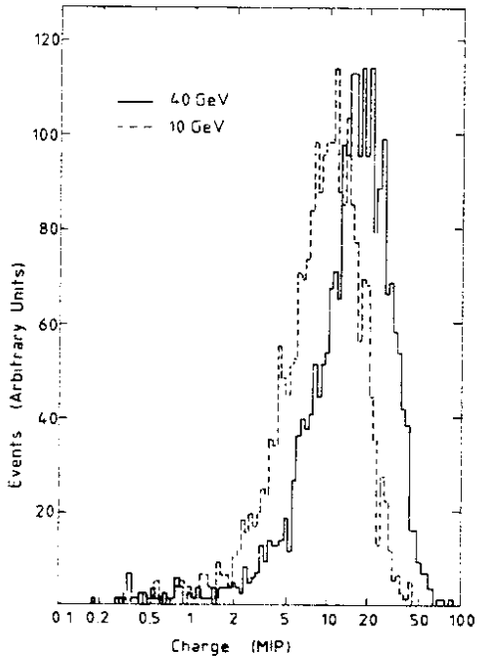

Fig. 25. The same as Fig. 24 but showing 10 and 40 GeV e (Ref. 6).

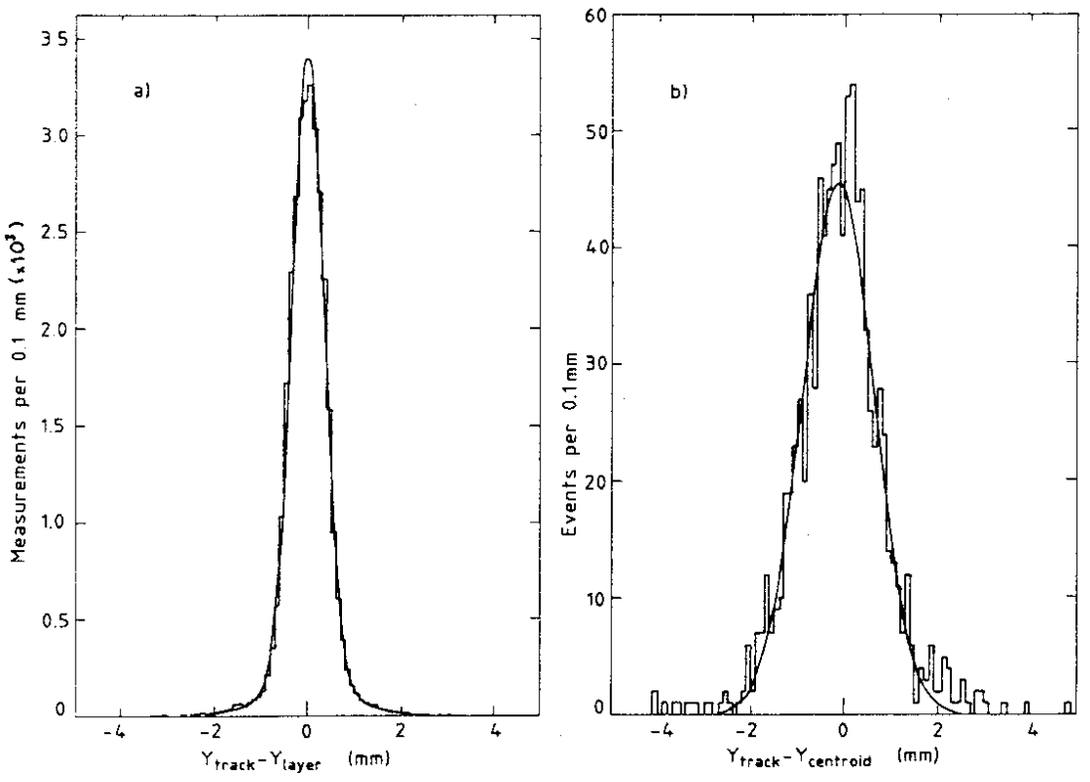

Fig. 26. a) The track residuals in the first 18 tracking layers of the UA2 SFD prototype (Ref. 6). The distance between each spot centroid and the fitted track is plotted. The data are fitted with a central Gaussian, of σ = 0.35 mm (94%) and two satellite Gaussians of σ = 0.58 mm (2 x 3%).
b) The shower location precision for 40 GeV e. The horizontal axis is the difference between the impact point in the Pb converter, as determined by the first 18 layers, and the centroid of the shower pulse height distribution seen after the Pb converter, in the final 6 layers. The fitted curve is a Gaussian of σ = 0.76 mm.

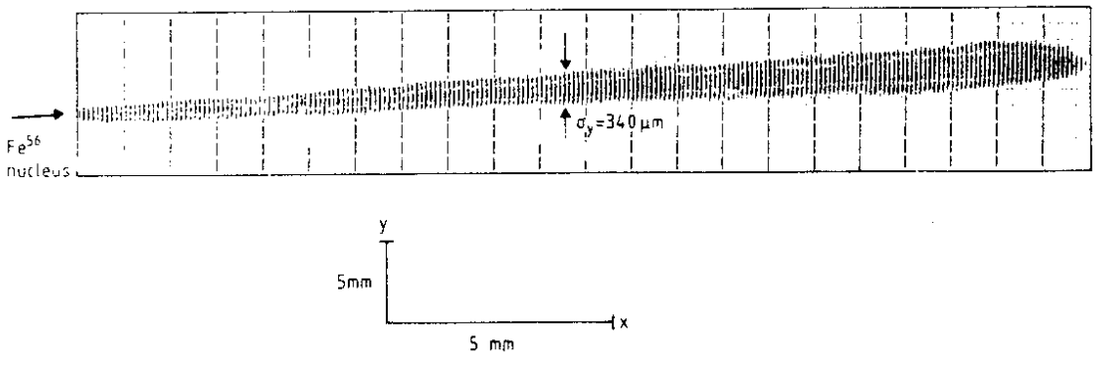

Fig. 27. A stopping ^{56}Fe nucleus in the plastic SCIFI detector of Ref. 7. The non-EMA fibres are square with a centre-to-centre spacing of 100 μm. The observed broadening of the track is largely due to UV cross-talk (see Fig. 6b).

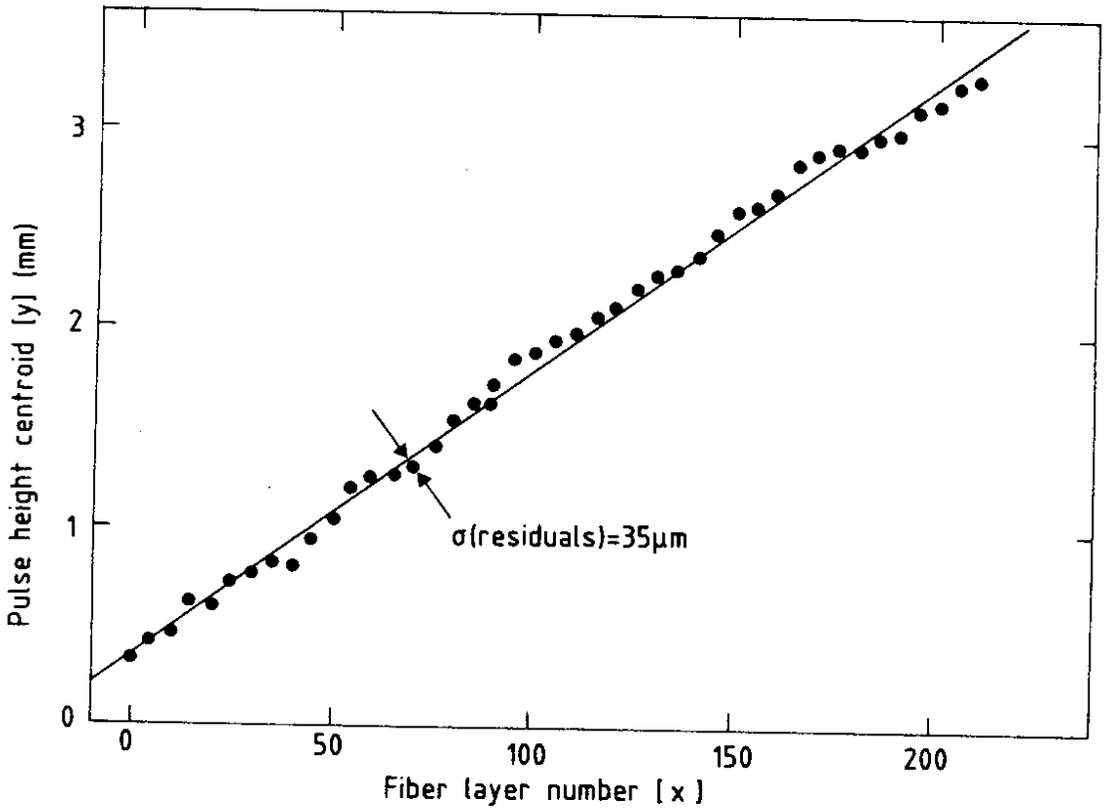

Fig. 28. Track residuals for a single ^{56}Fe event (Ref. 7). The transverse pulse height centroid (y) is plotted vs. fibre layer number (x). Each fibre layer represents 0.1 mm. The residual error is σ = 35 μm.

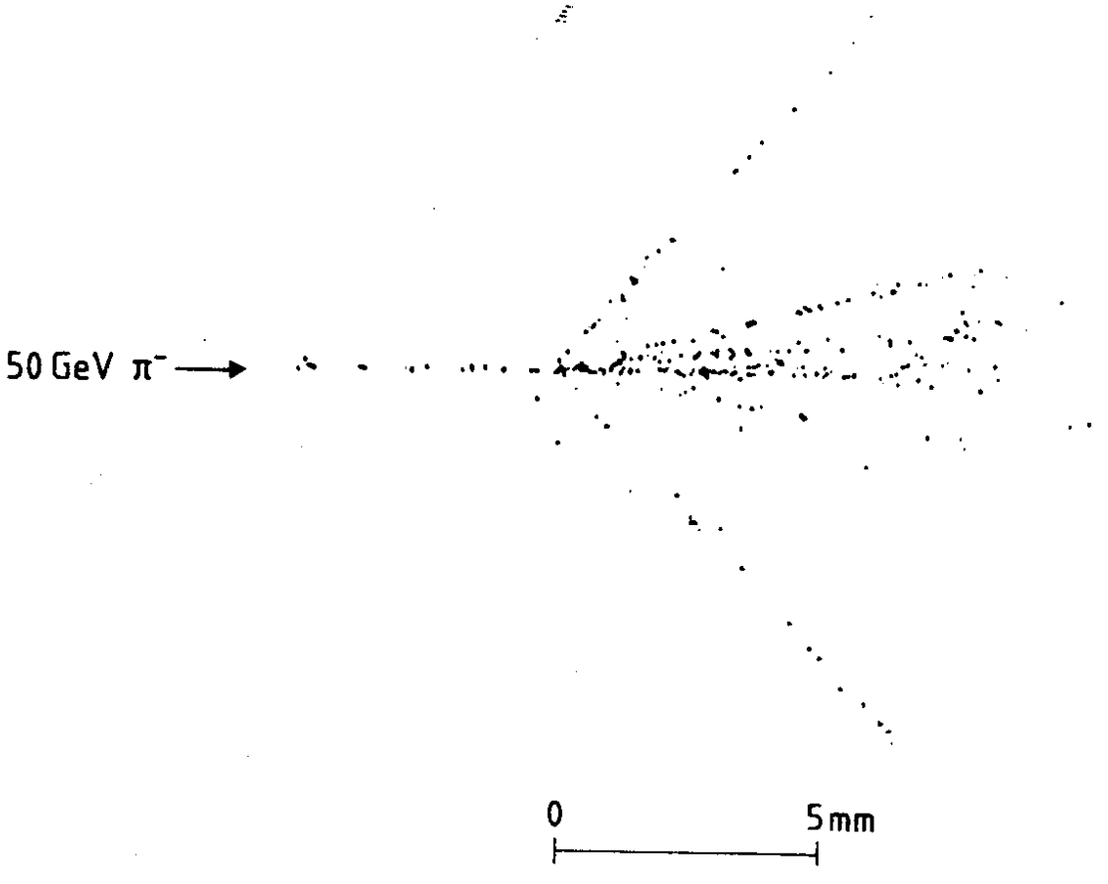

Fig. 29. Photograph of a 50 GeV π^- interaction in a glass SCIFI target (Ref. 5).

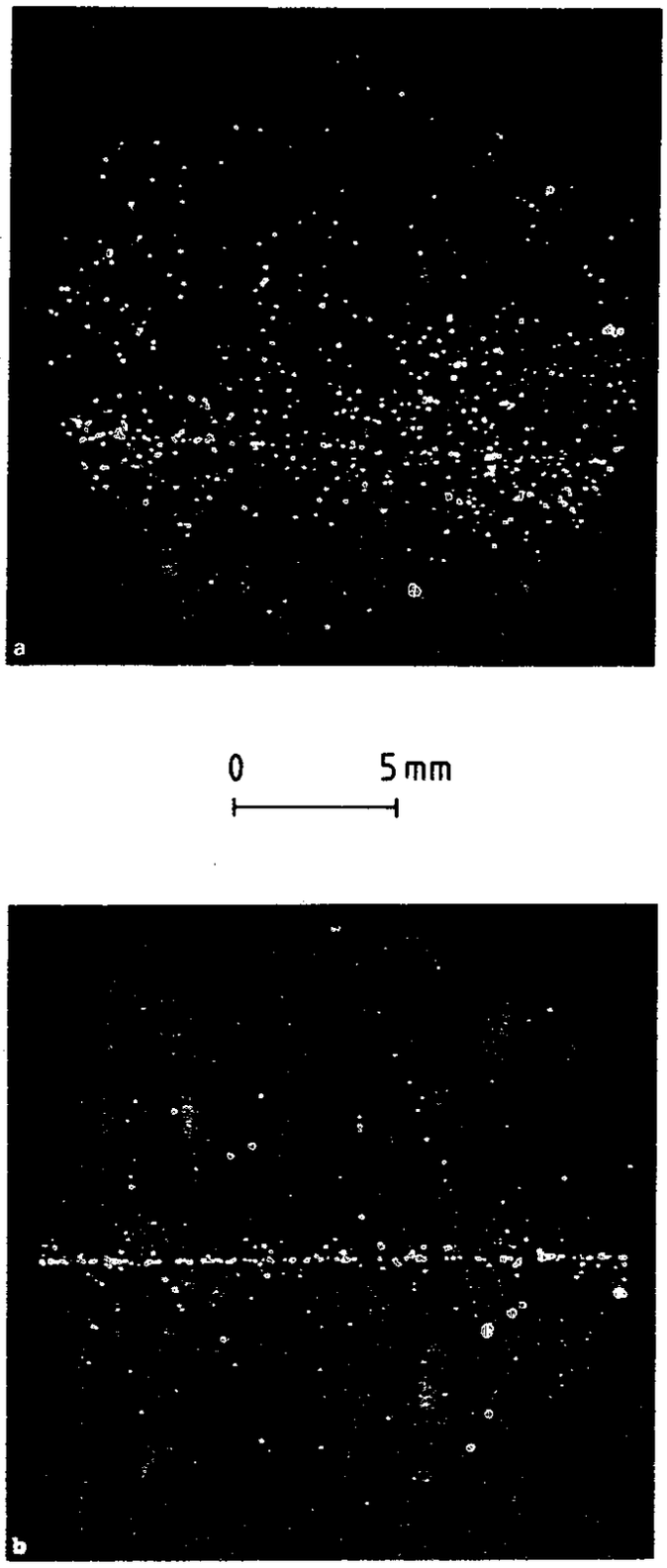

Fig. 30. Minimum ionizing tracks recorded on film using the glass SCIFI targets shown in Figs. 17 and 18 (Ref. 10): a) target 1 (no EMA) and b) target 2 (with EMA).

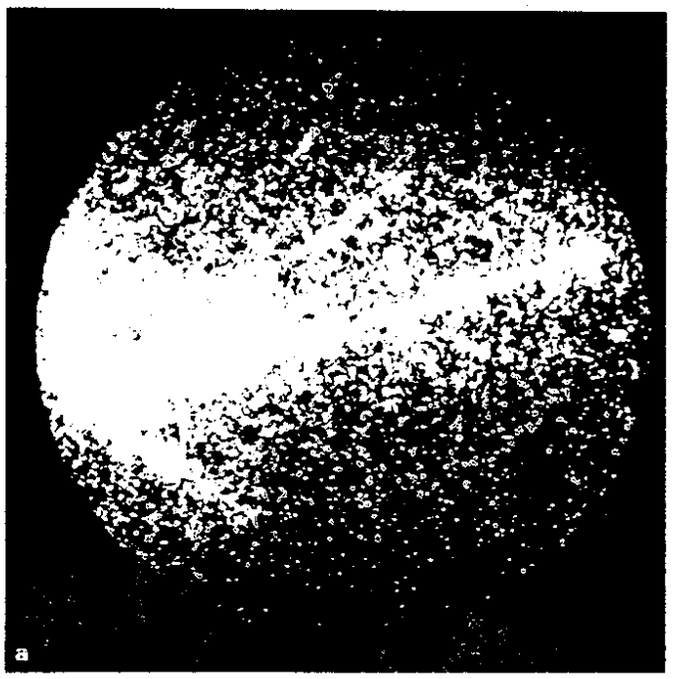

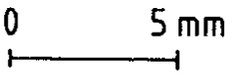

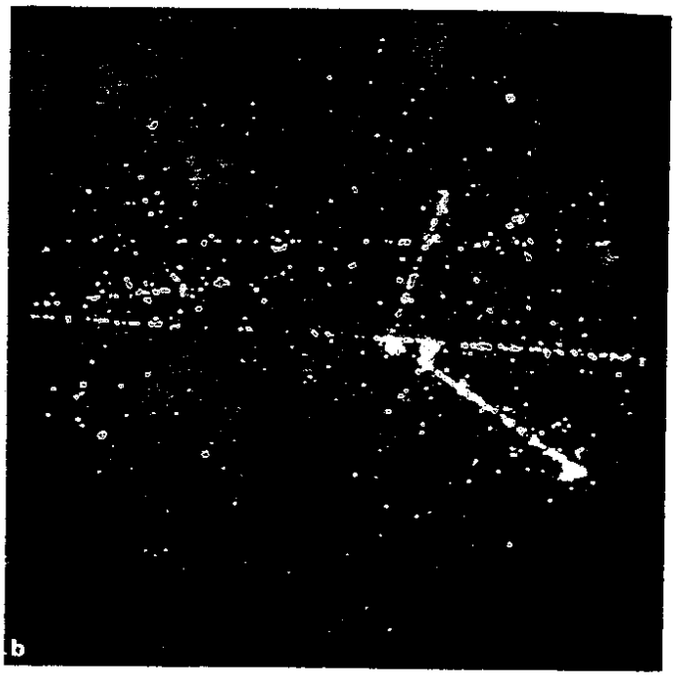

Fig. 31. Interactions of 5 GeV/c π^- recorded on film using the glass SCIFI targets shown in Figs. 17 and 18 (Ref. 10): a) target 1 (no EMA) and b) target 2 (with EMA).

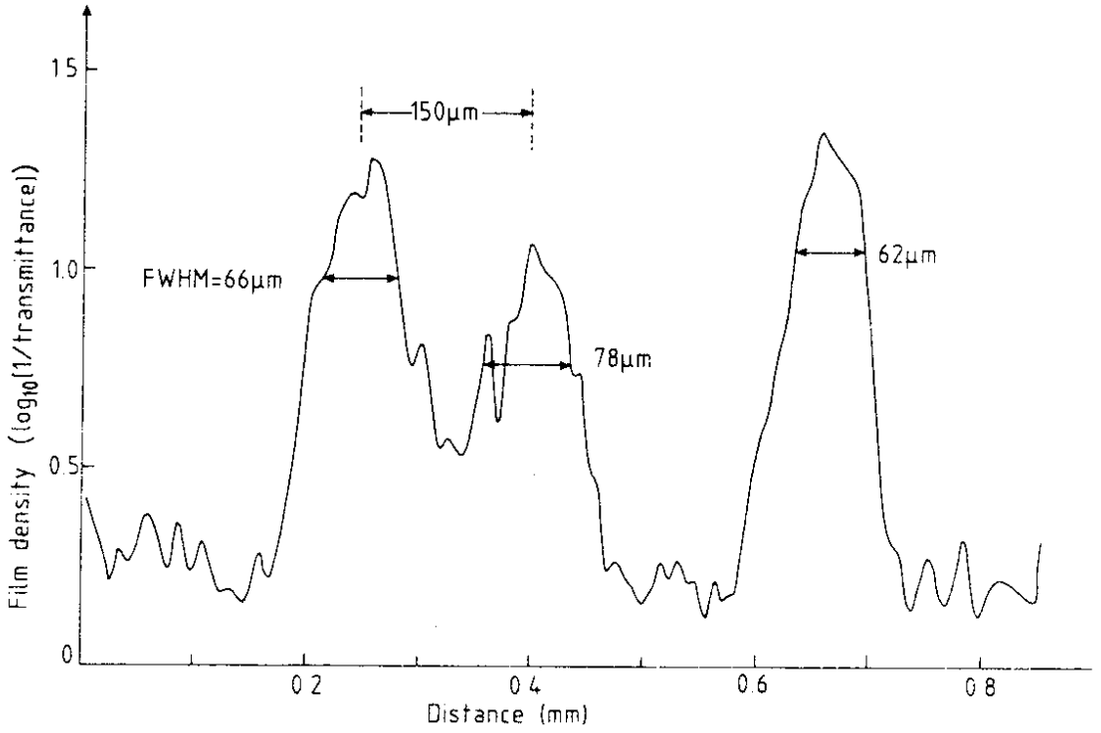

Fig. 32. Densitometer measurement through the centre of three spots along a track recorded on film in glass SCIFI (Ref. 10). The slit width of the densitometer (along the track direction) is 10 μm.

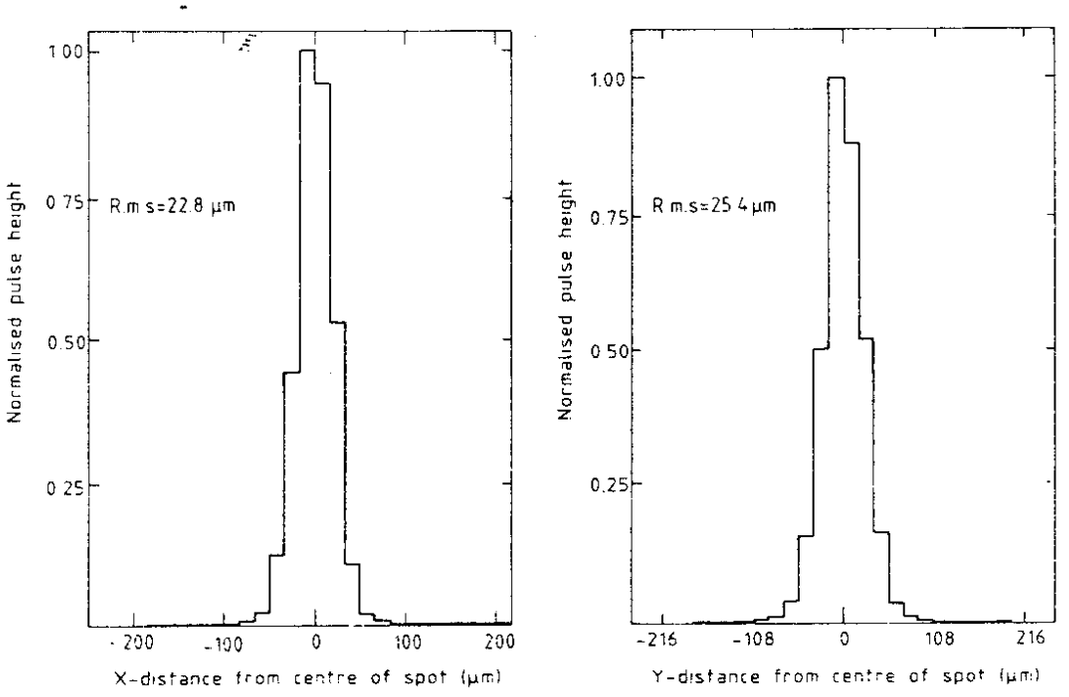

Fig. 33. Spot profiles obtained in glass SCIFI (Ref. 10). Figures 33-38 are results obtained in a 5 GeV π^- beam using the glass SCIFI target 2 (Figs. 17 and 18) with CCD readout.

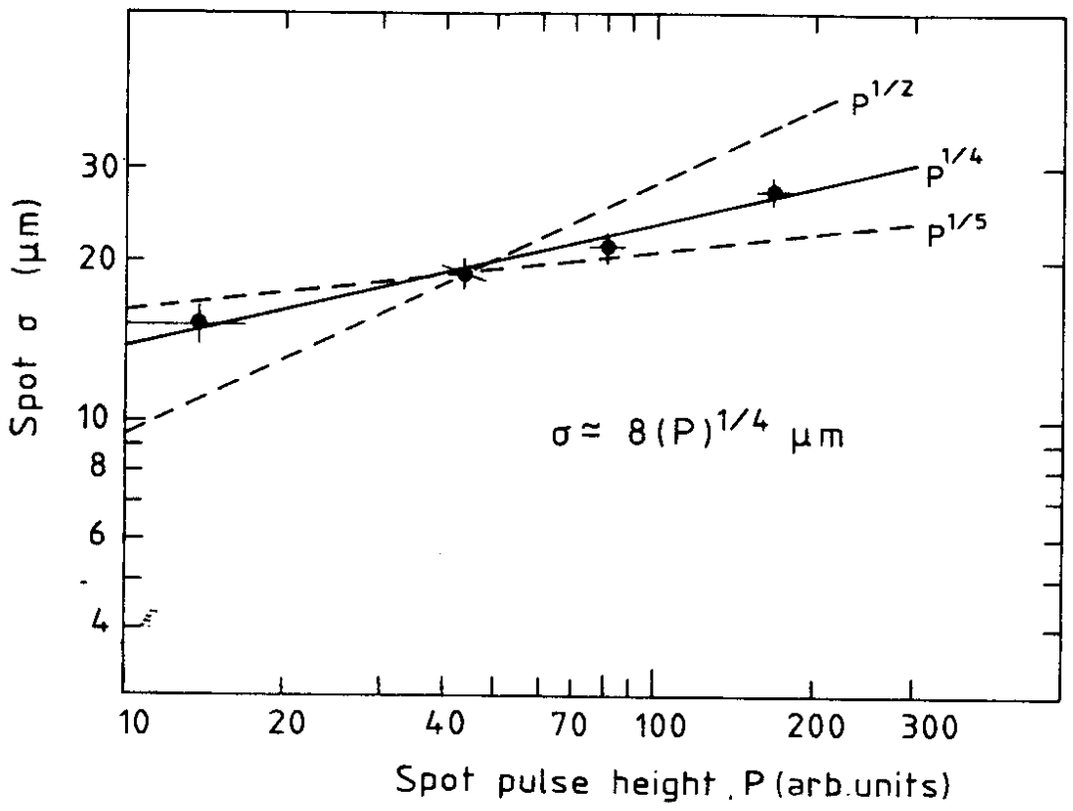

Fig. 34. Spot size vs. pulse height in glass SCIFI (Ref. 10).

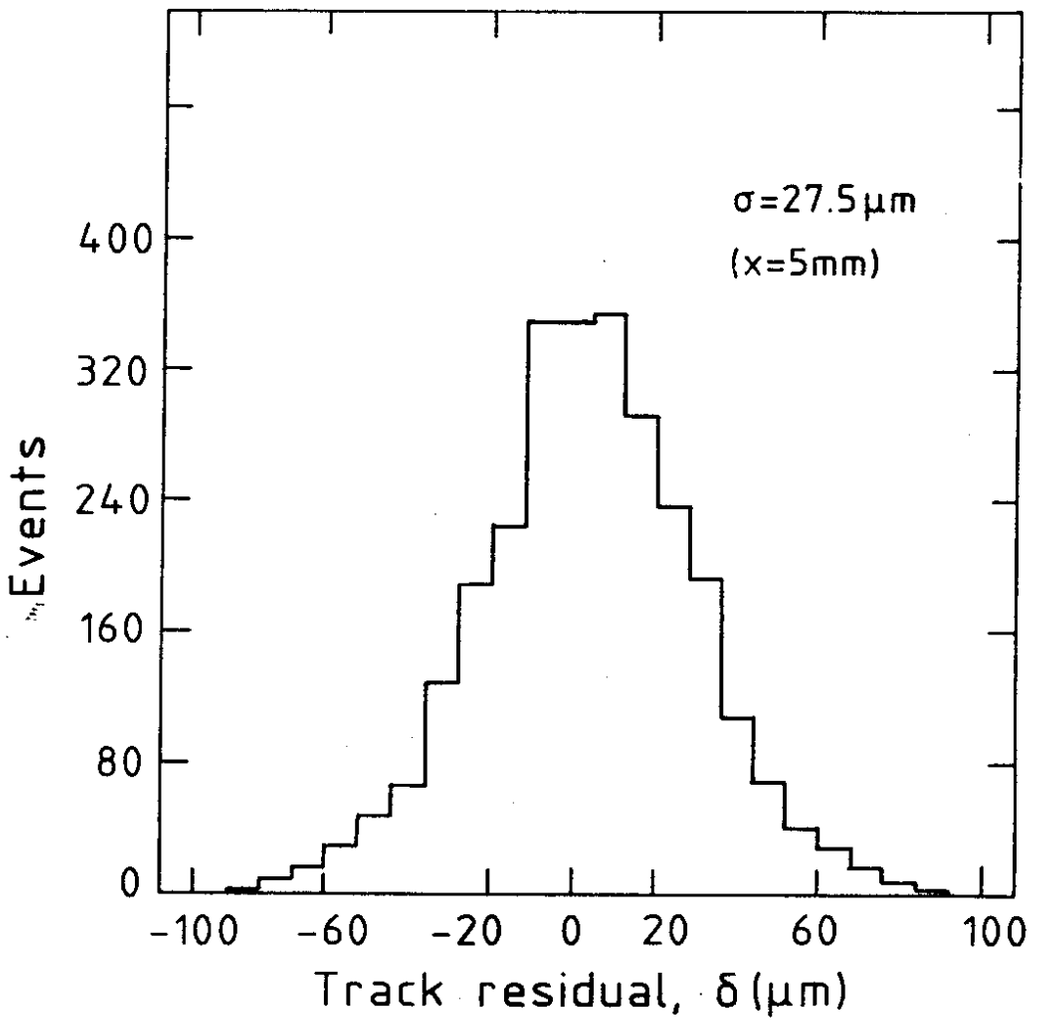

Fig. 35. Track residual distribution in glass SCIFI (Ref. 10).

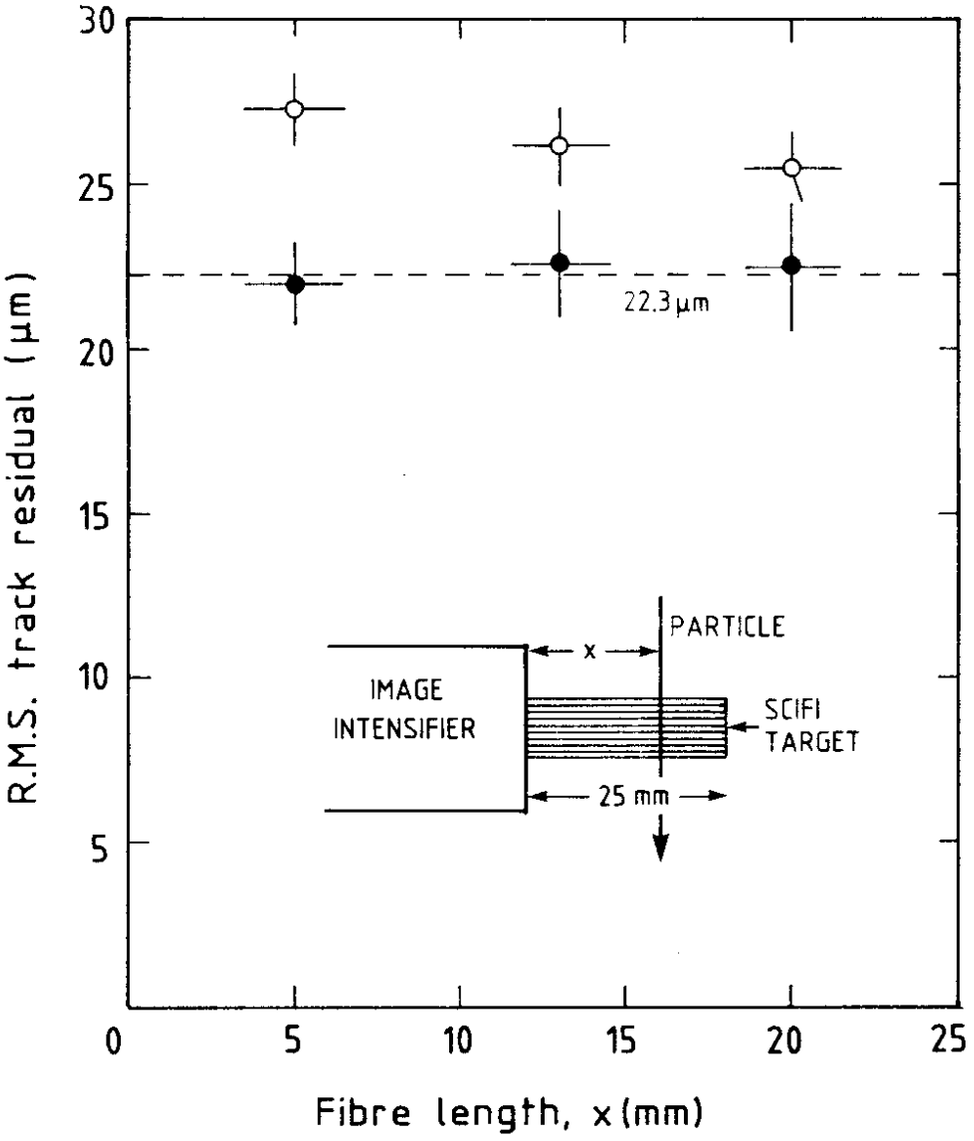

Fig. 36. R.m.s. track residuals vs. depth (x) into the glass SCIFI target (Ref. 10). The black dots show the original data (open dots) after correcting for background tracks.

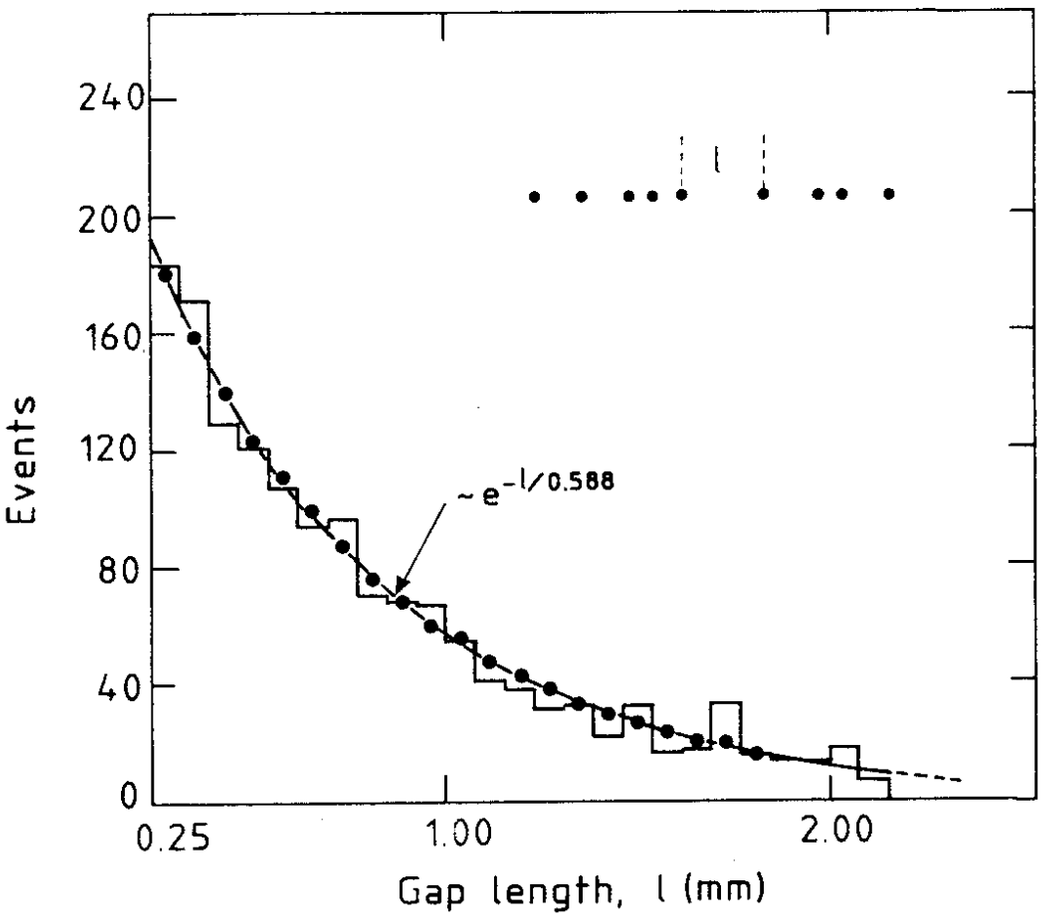

Fig. 37. The gap length distribution which is used to extract the spot frequency in glass SCIFI (Ref. 10).

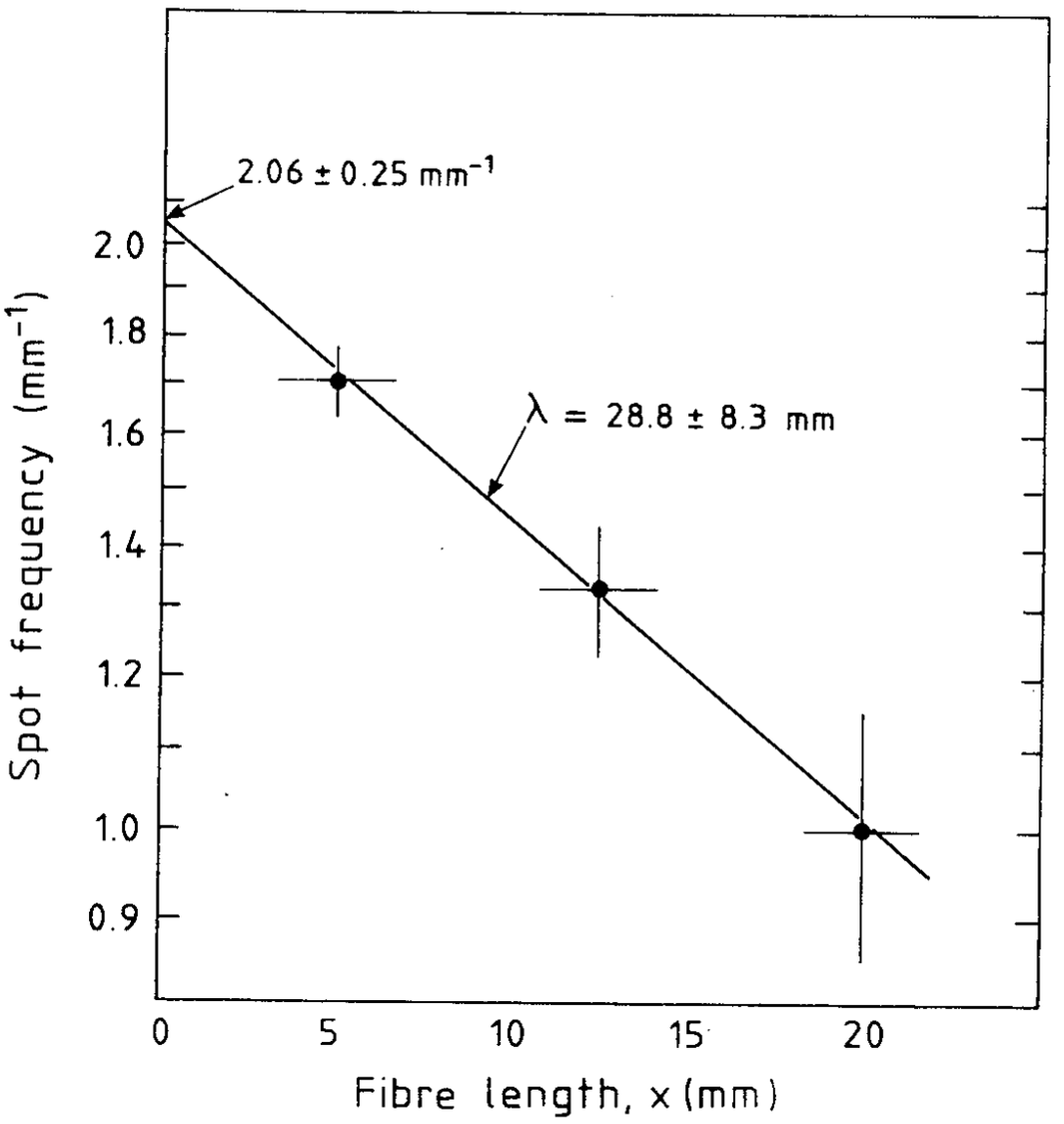

Fig. 38. The spot frequency vs. fibre length in glass SCIFI (Ref. 10).

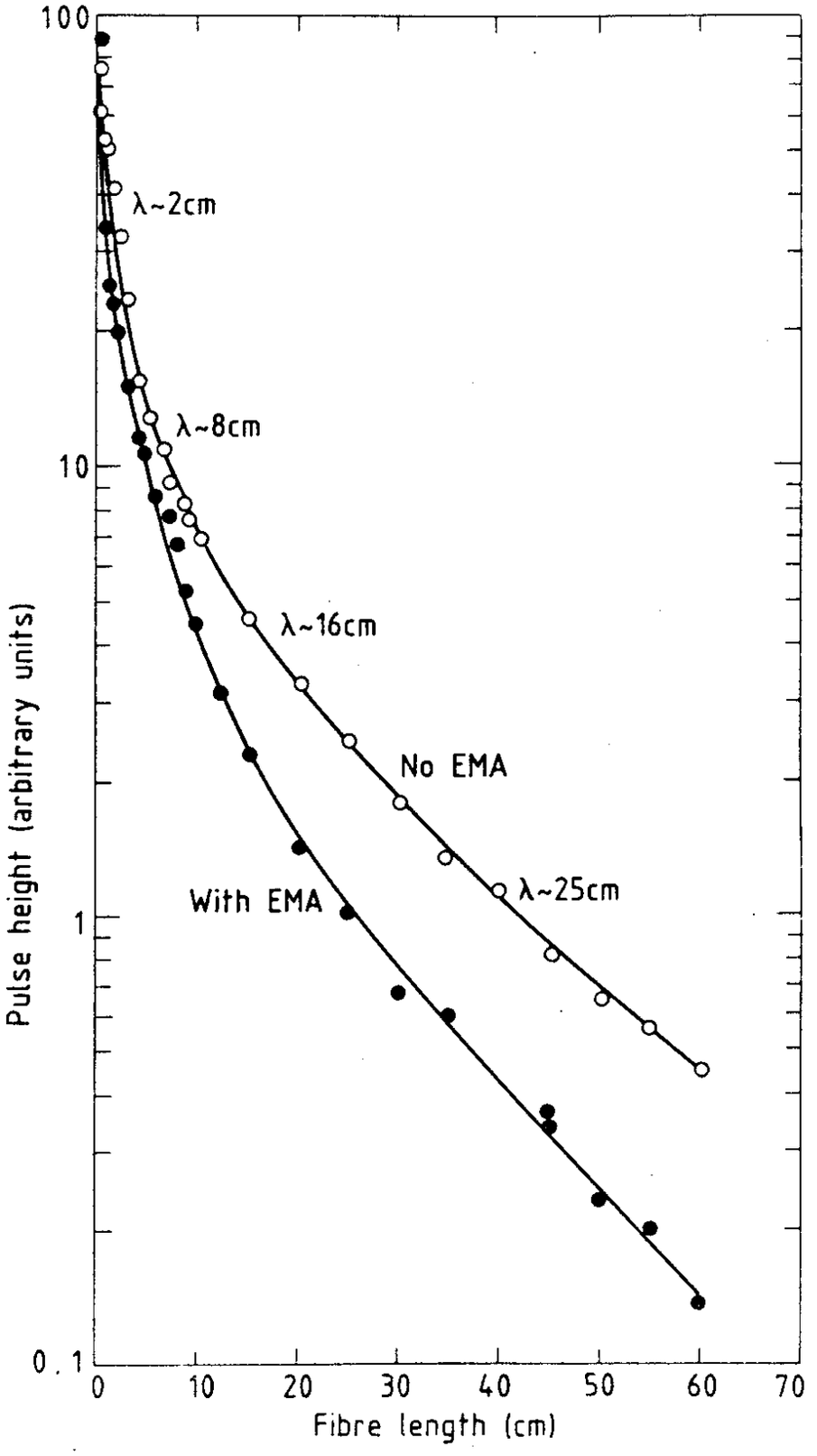

Fig. 39. Measurement of the attenuation of scintillation light in single multifibre bundles manufactured during production of the glass SCIFI targets 1 ('No EMA') and 2 ('With EMA'), shown in Figs. 17 and 18 (Ref. 10). The fibres are excited by a UV source.

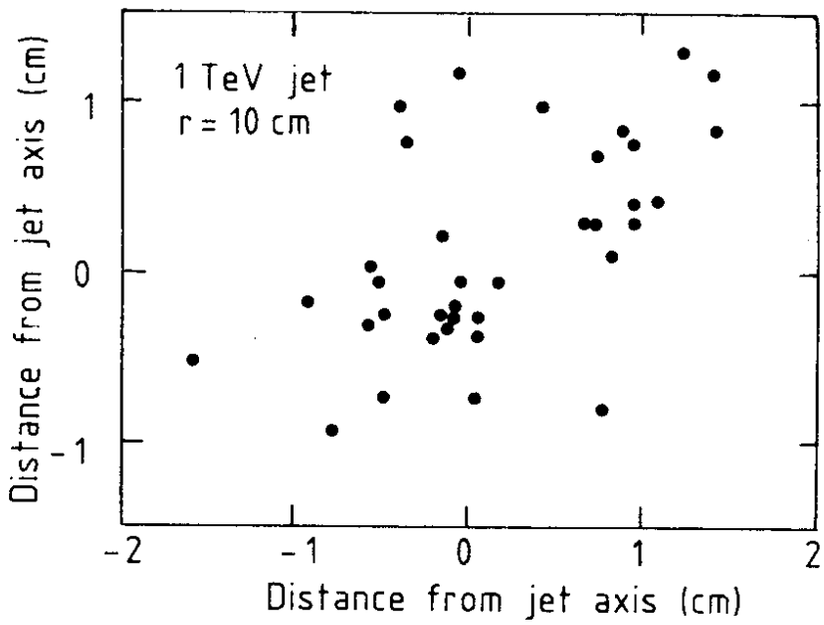

Fig. 40. Transverse distribution of charged particles in the core of a 1 TeV jet, at a distance of 10 cm from the interaction point (Ref. 51).

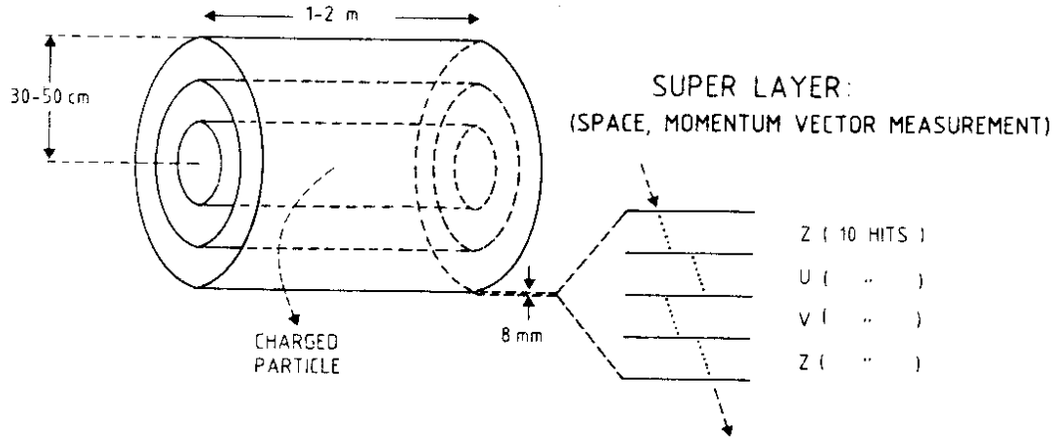

Fig. 41. Geometry of a SCIFI micro-tracker for a supercollider detector.

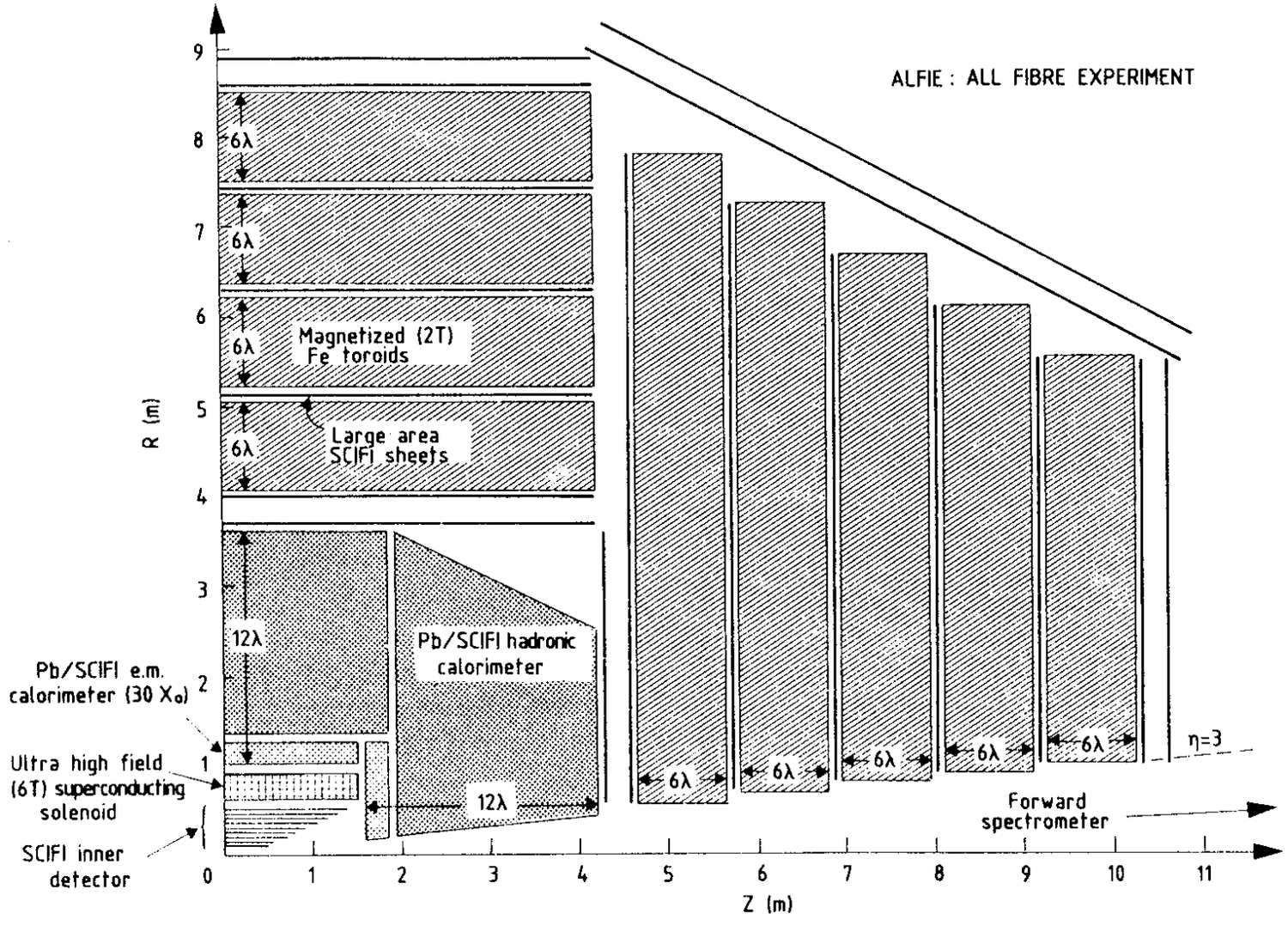

Fig. 42. ALFIE: All Fibre Experiment for a supercollider. The dimensions are chosen for operation at $\sqrt{s}$ = 20–40 TeV.

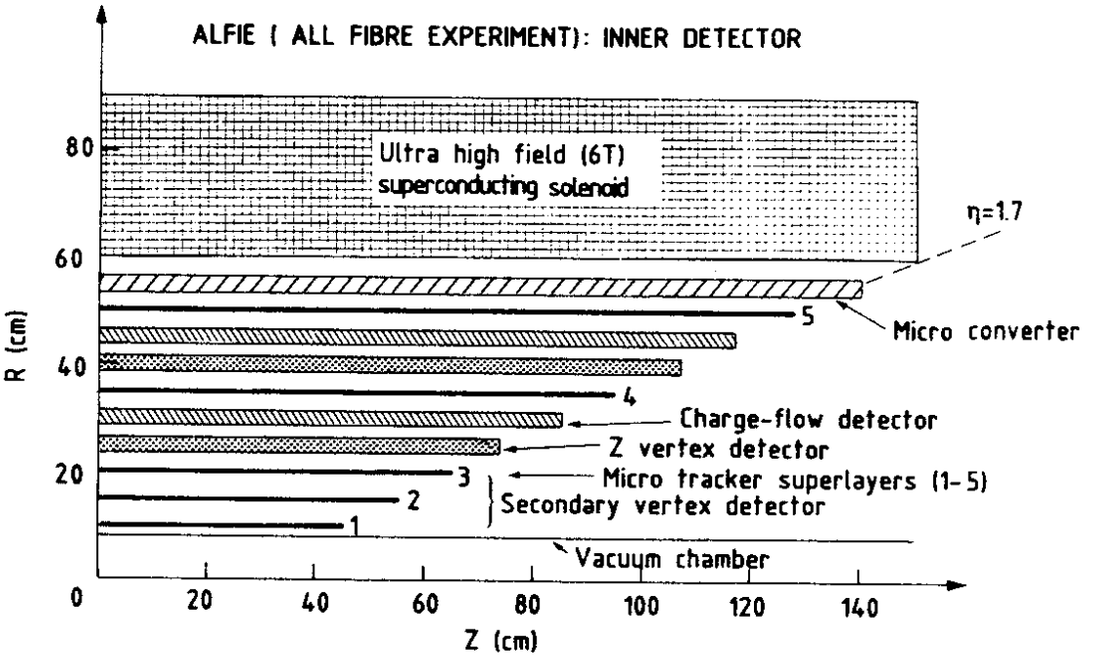

Fig. 43. The inner detector of ALFIE. Further representations of each element are shown in Figs. 41, 44-46.

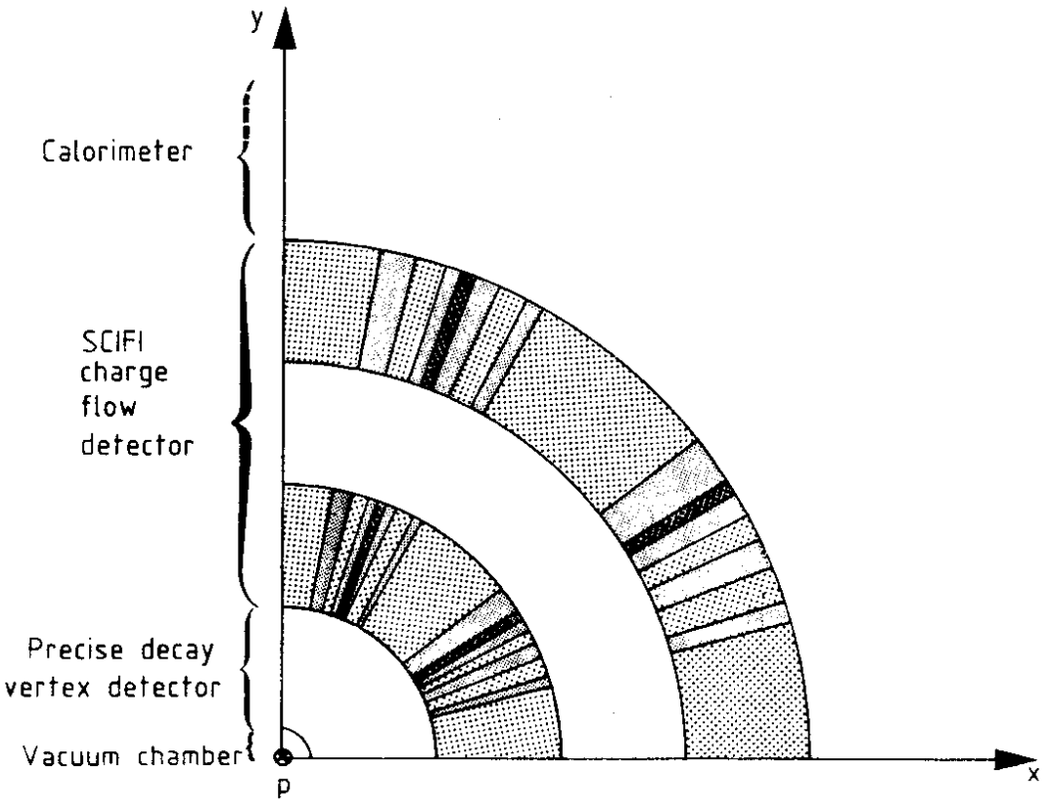

Fig. 44. The SCIFI charge flow detector.

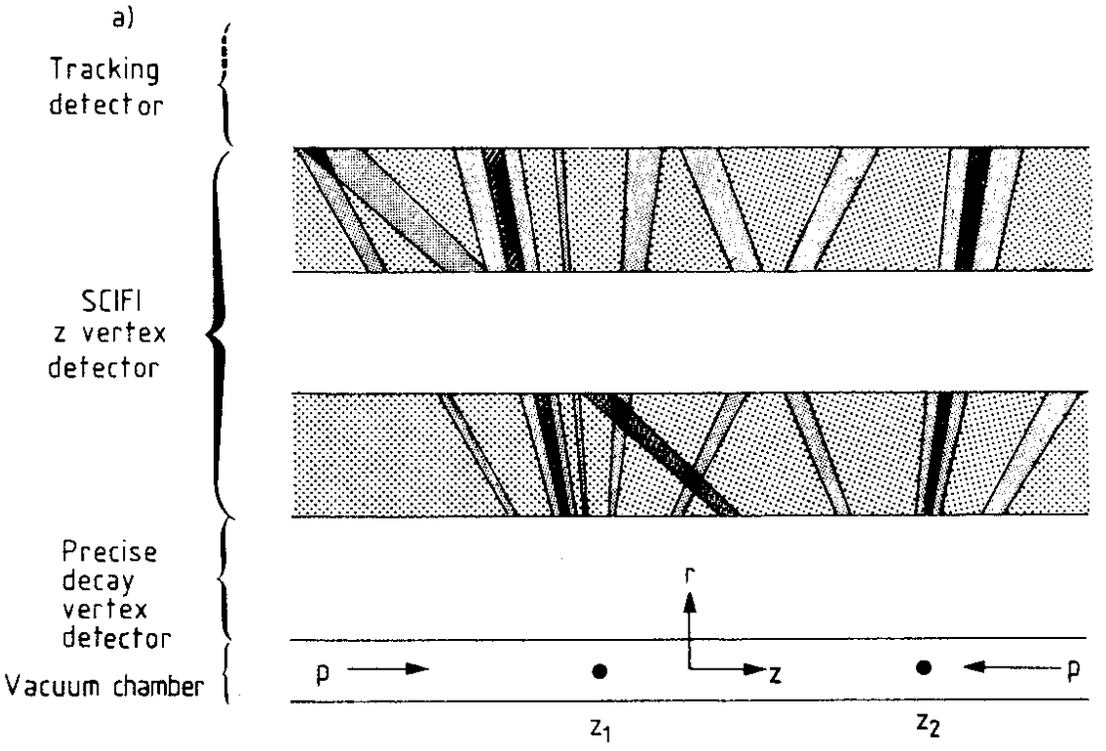

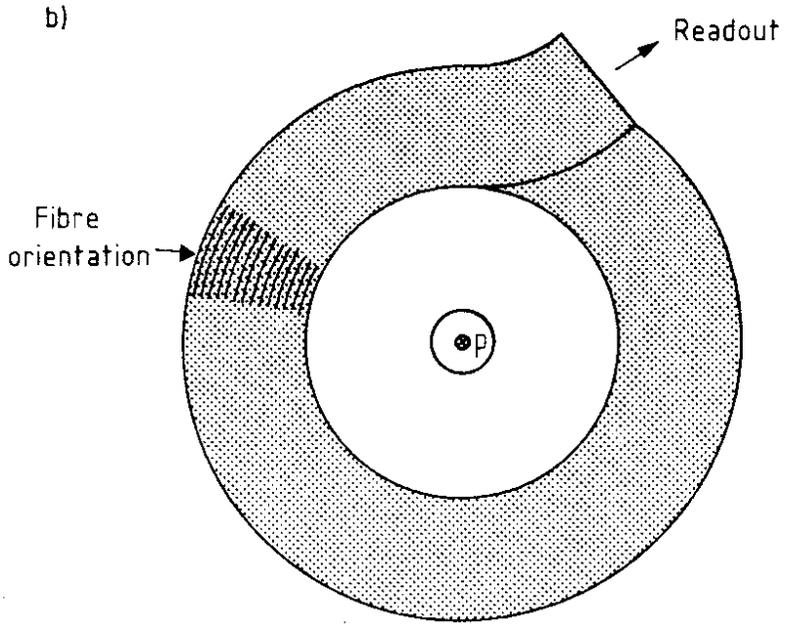

Fig. 45. The SCIFI z vertex detector. The fibres are oriented perpendicular to the beam axis.

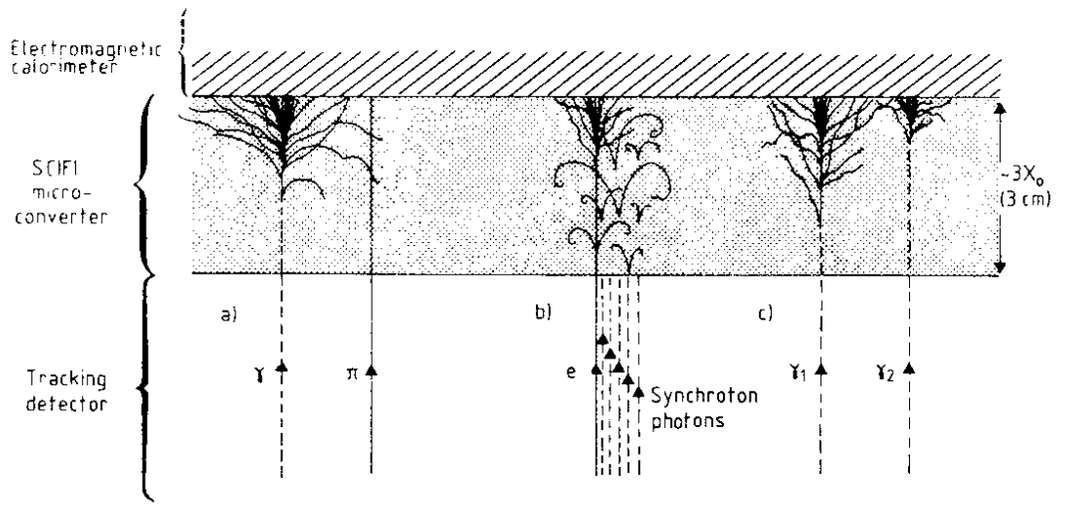

Fig. 46. The SCIFI micro-converter. The functions are a) to identify false electron signatures from $\pi\gamma$ overlap, b) to provide positive electron identification by means of showering and synchrotron photon identification and c) to identify false signatures of a hard single photon due to high energy π^0/η production.

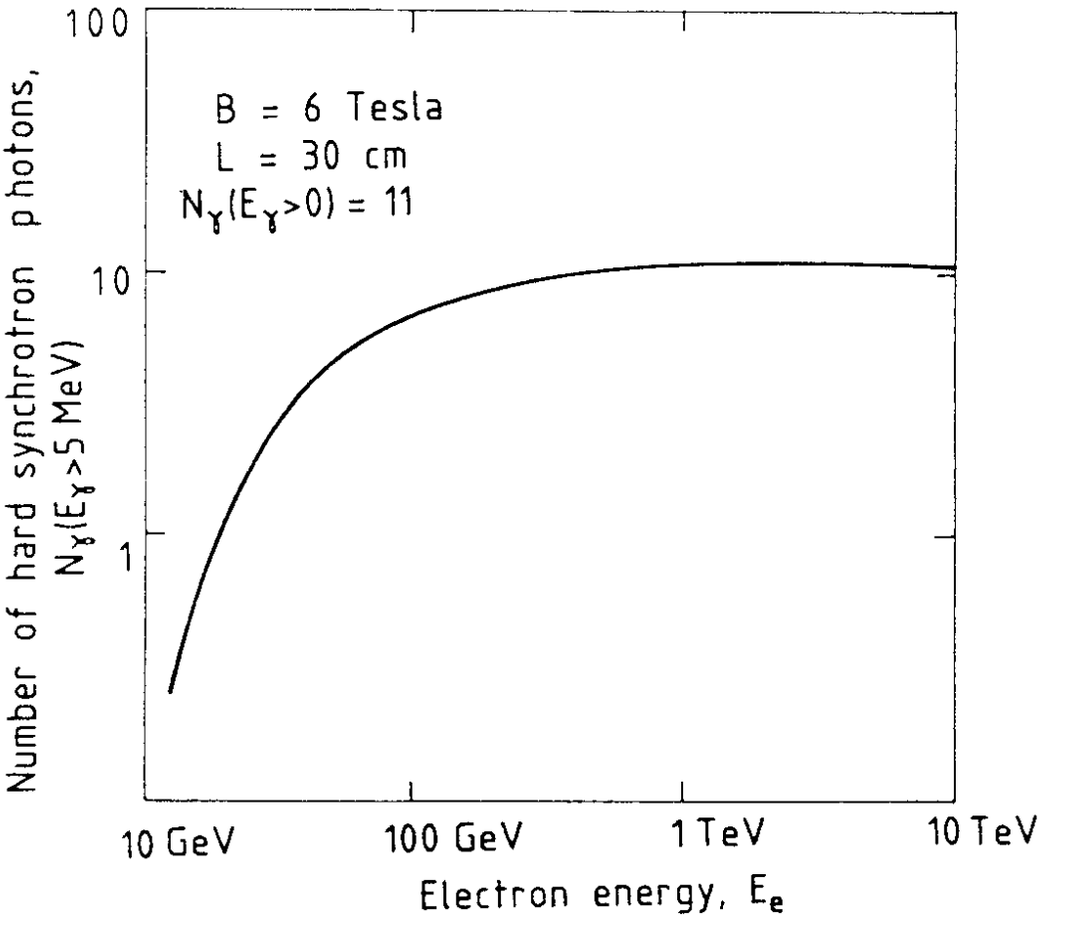

Fig. 47. The hard synchrotron photon flux, N_γ (E_γ > 5 MeV), radiated by electrons of energy E_e in a compact inner tracker similar to Fig. 43.

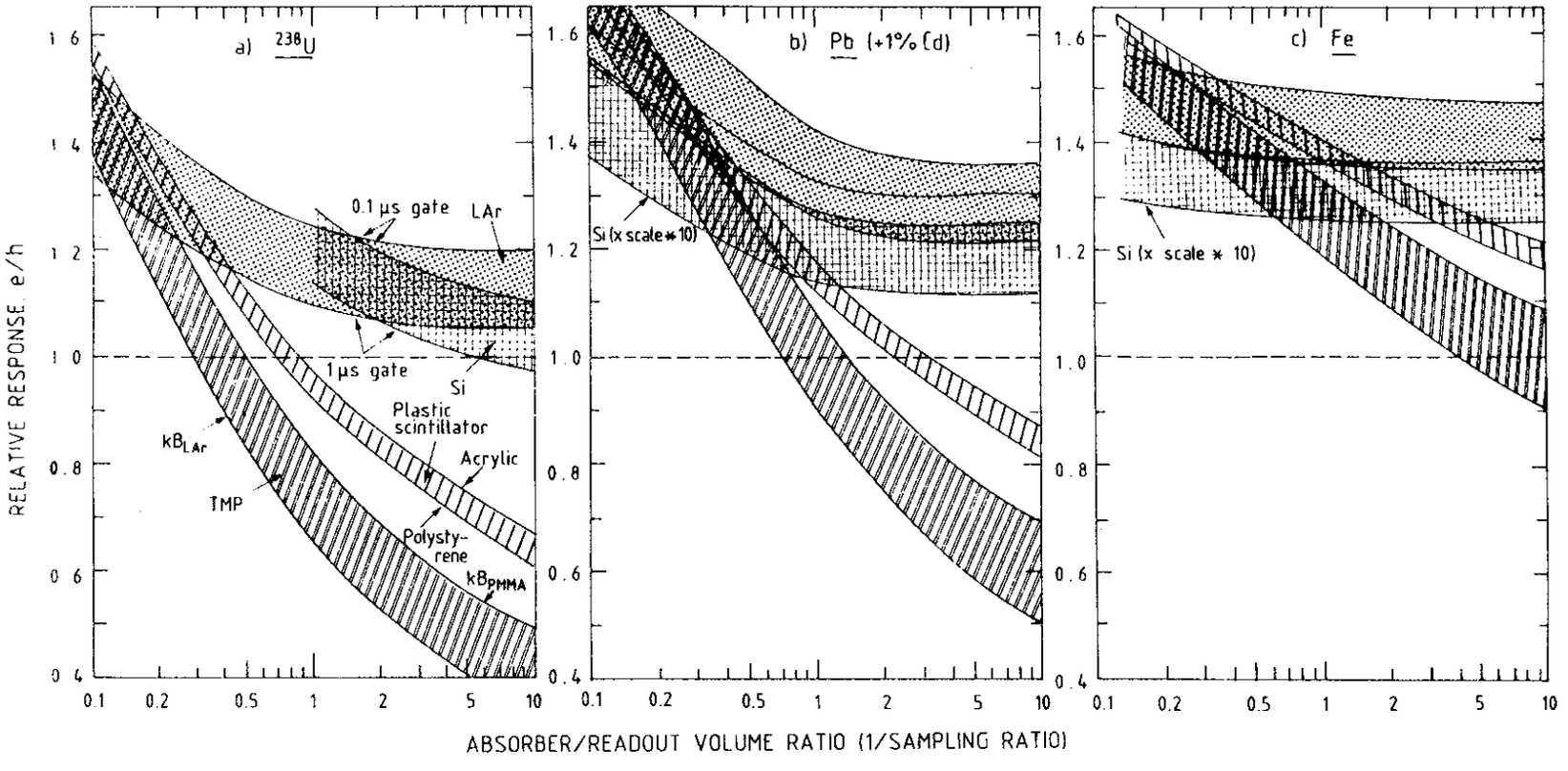

Fig. 48. The relative electron/hadron response vs. absorber/readout volume ratio for hadron calorimeters (Ref. 53). The absorber materials are a) uranium 238, b) lead (+1% cadmium, for improved capture of thermal neutrons) and c) iron. The range of possible responses of each readout material is indicated by a band. For TMP (tetramethyl pentane) the value of the Birks (recombination) constant, kB, is not yet known and so the values for LAr (liquid argon) and acrylic (PMMA) scintillator are used. Plastic scintillator responses for polystyrene and acrylic are indicated. The responses of Si and LAr are shown with the standard gate of 0.1 µs and a very long gate of 1 µs which captures essentially all of the thermal neutrons.

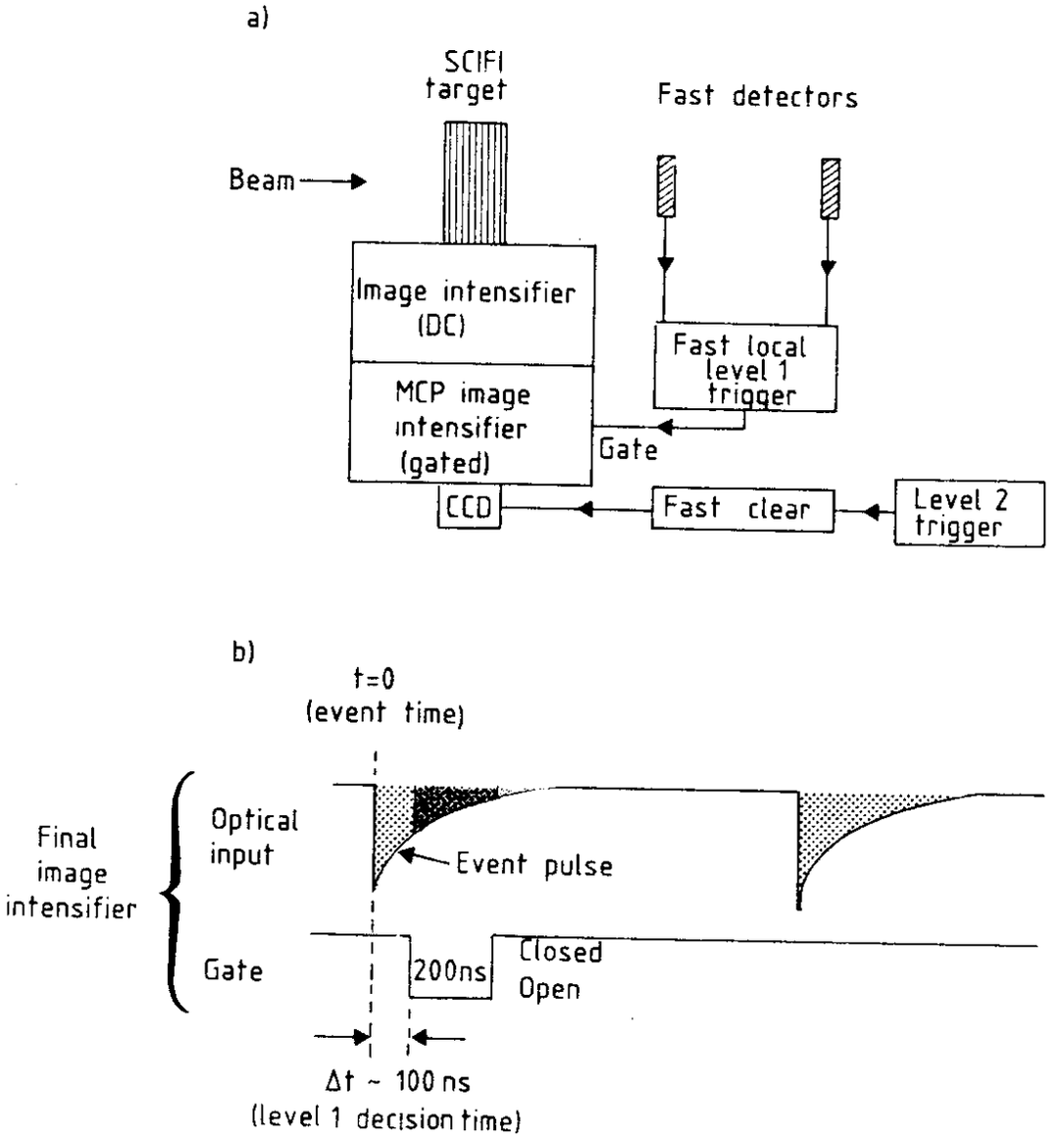

Fig. 49. a) Schematic and b) timing diagrams for the operation of SCIFI readout at beam rates up to ~ 10^6 Hz.

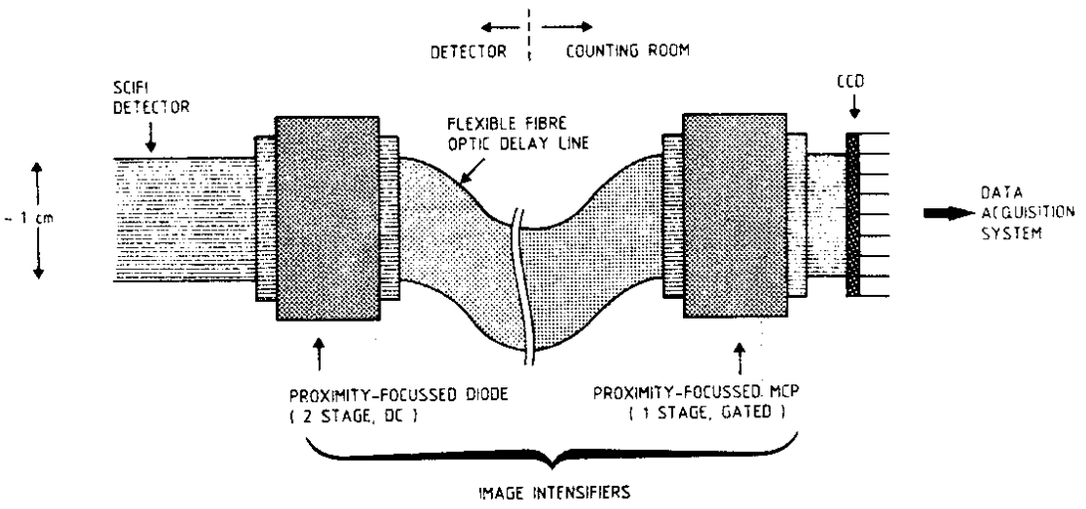

Fig. 50. SCIFI readout assembly for supercollider operation. The coherent fibre optic cable provides sufficient time delay for formation of a level 1 trigger which is then used to gate open the final MCP image intensifier.

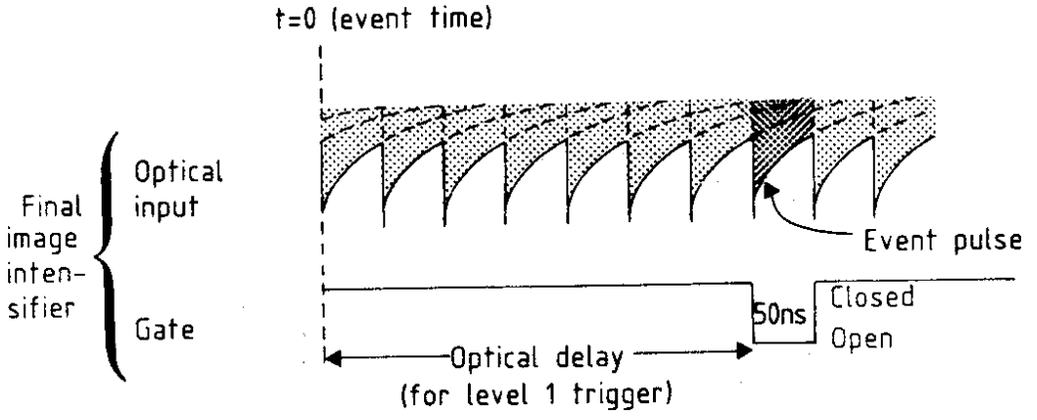

Fig. 51. Timing diagram for the final MCP image intensifier of Fig. 50, at an input event rate of 0.2 10^8 Hz.

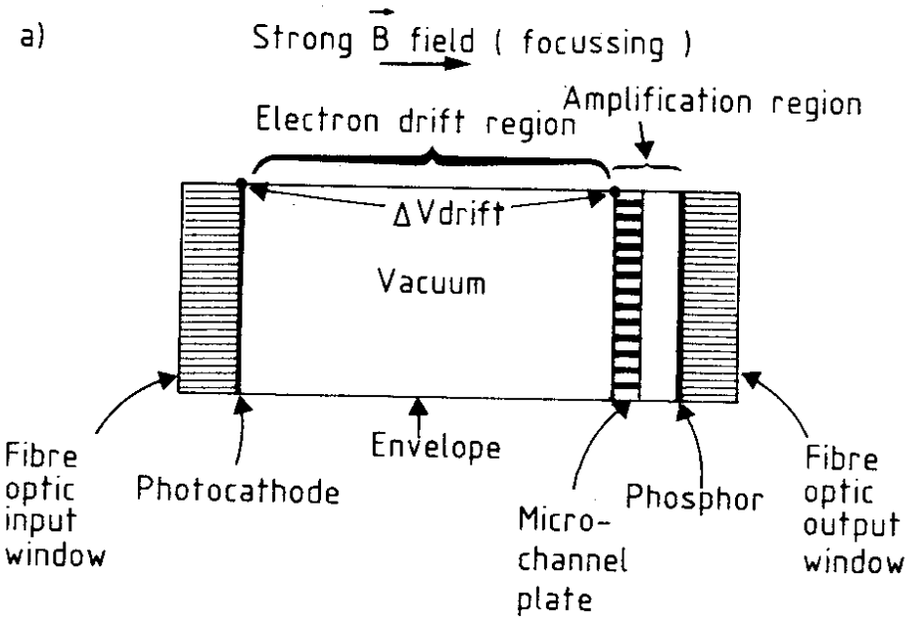

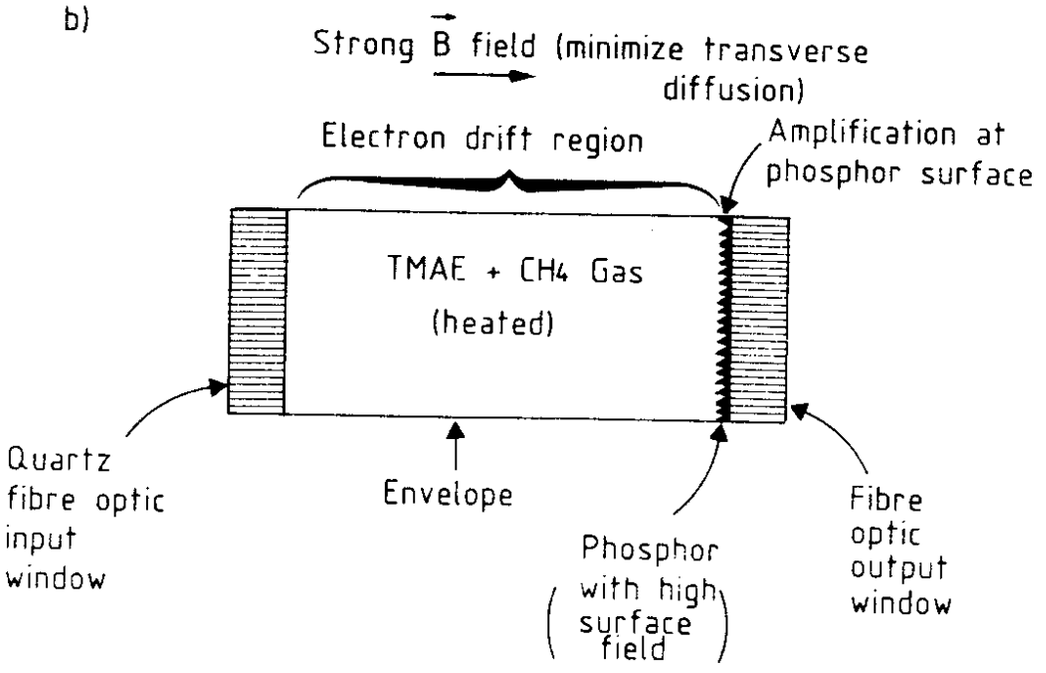

Fig. 52. Conceptual schemes for a coherent optical delay line involving a) vacuum and b) gas-filled devices.